Optimization of multiphysical material properties using surrogate models

vom Fachbereich Maschinenbau und Verfahrenstechnik
der Rheinland-Pfälzischen Technischen Universität Kaiserslautern-Landau
zur Verleihung des akademischen Grades
Doktor-Ingenieur (Dr.-Ing.)
genehmigte Dissertation

von
M.Sc. Julian Marr
aus Altenkunstadt

Berichterstattende:	Prof. Dr.-Ing. Ralf Müller
	PD Dr. rer. nat. Heiko Andrä
	Prof. Dr.-Ing. Kristin de Payrebrune
Vorsitzender:	Prof. Dr.-Ing. Eberhard Kerscher
Dekan:	Prof. Dr. rer. nat. Roland Ulber

Tag der Einreichung:	15.11.2023
Tag der mündlichen Prüfung:	25.06.2024

Kaiserslautern, 2024

D 386

Vorwort

Die vorliegende Arbeit entstand während meiner Tätigkeit als Doktorand bei der ZF Friedrichshafen AG in der Abteilung Multiphysics and Simulation in Kooperation mit dem Lehrstuhl für Technische Mechanik der RPTU Kaiserslautern-Landau, dem Institut für Mechanik der TU Darmstadt und der Abteilung Material- und Strömungssimulation des Fraunhofer Instituts für Techno- und Wirtschaftsmathematik.

Mein besonderer Dank gilt Prof. Dr.-Ing. Ralf Müller und PD Dr. Heiko Andrä für die in jeder Hinsicht hervorragende Betreuung und Unterstützung während der Anfertigung meiner wissenschaftlichen Arbeit. Weiterhin bedanke ich mich bei Prof. Dr.-Ing. Kristin de Payrebrune für die Erstellung des Drittgutachtens. Herrn Prof. Dr.-Ing. Eberhard Kerscher danke ich vielmals für die Übernahme des Prüfungsvorsitzes.

Ich danke allen direkten Kollegen in der ZF Friedrichshafen AG, die mich bei meiner Promotion fachlich unterstützt haben. Insbesondere danke ich an dieser Stelle Dr. Doris Reinel-Bitzer und Lukas Zartmann für die stets angenehme und kollegiale Atmosphäre sowie den fachlichen und anwendungsbezogenen Diskussionen. Mein Dank gilt auch Herrn Dr.-Ing. Constantin Bauer für die Unterstützung bei experimentellen Themen.

Zu guter Letzt möchte ich mich bei meinen Eltern für ihre bedingungslose Unterstützung nicht nur während meiner Promotion bedanken.

Kurzfassung

Die Auswahl geeigneter Materialien stellt im Rahmen der zunehmenden Elektrifizierung von Fahrzeugen eine anspruchsvolle Aufgabe dar. Dies liegt vor allem darin begründet, dass nicht nur mechanische, sondern multiphysikalische Anforderungen an die Materialeigenschaften simultan berücksichtigt werden müssen. Ein Beispiel hierfür ist die Forderung nach einem elektrisch isolierenden, aber gut wärmeleitenden Material mit geringer Wärmeausdehnung. Kunststoffbasierte Verbundwerkstoffe bieten die Möglichkeit die physikalischen Materialeigenschaften durch Verwendung entsprechender Füllstoffe gezielt zu beeinflussen. Die makroskopischen Materialeigenschaften ergeben sich hierbei gemäß dem Ursache-Wirkungs-Prinzip: Herstellungsprozess → Struktur → Eigenschaften in Abhängigkeit der komplexen Mikrostruktur des Kunststoffverbunds. Das Design von Materialien erfordert eine Betrachtung dieser Prozesskette in umgekehrter Reihenfolge und kann als inverse Problemstellung aufgefasst werden. Entsprechend vielfältig und herausfordernd gestaltet sich der Entwurf solcher Funktionswerkstoffe. In der vorliegenden Arbeit soll die Frage beantwortet werden, wie die Mikrostruktur von Verbundwerkstoffen beschaffen sein muss, um ein gewünschtes effektives thermomechanisches Materialverhalten aufzuweisen. Eine rein experimentelle Entwicklung solcher Materialien stellt im Allgemeinen einen zeitaufwändigen und kostspieligen Prozess dar, da viele Prototypen hergestellt und getestet werden müssen. Computergestützte Multiskalenmethoden ermöglichen durch direkte Modellierung der Heterogenität auf Mikrostrukturebene eine rein virtuelle Charakterisierung von Verbundwerkstoffen. Diese Verfahren bieten somit das Potenzial teure Experimente zu ersetzen und die Produktentwicklungszeit zu verkürzen. In dieser Arbeit wird eine simulationsbasierte Optimierungsmethodik zum Design von Funktionswerkstoffen präsentiert. Hierzu wird ein metamodellbasierter Ansatz vorgeschlagen, der auf einer Approximation der Struktur-Eigenschafts-Beziehungen in Abhängigkeit physikalischer Parameter der Mikrostruktur basiert. Dies ermöglicht eine effiziente Lösung multiphysikalischer Materialoptimierungsprobleme in hochdimensionalen Parameterräumen. Die Methodik wird anschließend zur Optimierung thermomechanischer Eigenschaften partikelgefüllter und kurzfaserverstärkter Kunststoffe angewendet.

In Kapitel 2 werden einige grundlegende Aspekte der Kontinuumsmechanik zur Modellierung thermoelastischer Materialien und der Wärmeleitung beschrieben. Die eingeführten Notationen und Beziehungen werden in den folgenden Kapiteln zur Berechnung effektiver Materialeigenschaften durch numerische Simulation auf Mikrostrukturebene verwendet.

In Kapitel 3 wird die metamodellbasierte Optimierungsmethodik zum Design von Funktionswerkstoffen vorgestellt. Dazu wird für das Materialdesign ein Strukturoptimierungsproblem formuliert. Durch Beschreibung der makroskopischen Materialeigenschaften in Form tensorieller Größen wird eine Berücksichtigung richtungsabhängiger (anisotroper) Anforderungen an die Materialien ermöglicht. Als Designvariablen werden physikalische Parameter der Mikrostruktur gewählt, da diese beim Herstellungsprozess direkt beeinflusst werden können. Diese setzen sich aus Parametern der geometrischen Mikrostruktur (z. B. dem Füllgrad) und den Materialeigenschaften (z. B. dem Elastizitätsmodul) der einzelnen Konstituenten zusammen. Verschiedene Aspekte wie der große Rechenaufwand und der Einfluss stochastischer Effekte bedingt durch die heterogene Mikrostruktur motivieren die Entwicklung der metamodellbasierten Optimierungsmethodik. Diese basiert auf einer Approximation der Struktur-Eigenschafts-Beziehung innerhalb des gesamten Parameterraums. Ein wesentlicher Vorteile solcher Metamodelle besteht im effizienten Einsatz globaler Optimierungsverfahren im Vergleich zur direkten Anwendung des mikromechanischen Simulationsmodells, insbesondere für hochdimensionale Probleme. Zur Erstellung der Metamodelle werden in einem ersten Schritt auf Grundlage von Verfahren der statistischen Versuchsplanung bestimmte Parameterkombinationen (experimentelle Designs) festgelegt. Für jedes dieser Designs wird ein repräsentatives Volumenelement generiert, das die jeweilige Konfiguration der Mikrostruktur wiedergibt. Die entsprechenden effektiven Materialeigenschaften werden durch numerische Homogenisierungsmethoden unter Vorgabe periodischer Randbedingungen berechnet. Als Resultat dieser Schritte steht eine Materialdatenbank zur Verfügung, welche die Struktur-Eigenschafts-Beziehung für eine diskrete Menge parametrisierter Mikrostrukturen beschreibt. Der nächste Schritt besteht darin, die effektiven Eigenschaften auf Grundlage dieser Materialdaten innerhalb des gesamten Parameterraums zu approximieren. Hierzu werden Polynome (Response Surface Modelle) und Kriging-Interpolationen vorgestellt. Die Verwendung von (globalen) Methoden der Sensitivitätsanalyse zur Quantifizierung der relativen Bedeutung der einzelnen Designvariablen wird diskutiert. Des Weiteren wird ein simples Konzept zur Bewertung der Robustheit der Designs bzw. für die robuste Optimierung vorgestellt.

Kapitel 4 bietet einen kompakten Überblick zu partikelgefüllten und kurzfaserverstärkten Kunststoffen. Neben der Beschreibung für technische Anwendungen relevanter Matrix- und Füllstoffmaterialien und deren Einfluss auf die makroskopischen Eigenschaften wird kurz auf die Herstellung und die Anwendungsgebiete dieser Materialien eingegangen.

In Kapitel 5 wird das metamodellbasierte Optimierungsverfahren anhand konkreter Materialbeispiele demonstriert. Hierzu wird in Kapitel 5.1 ein dreiphasiger partikelgefüllter Werkstoff mit großem Kontrast in den Wärmeleitfähigkeiten der einzelnen Konstituenten betrachtet, bei dem eine bestimmte thermische Leitfähigkeit eingestellt werden soll. Als Designvariablen werden der Füllgrad und die Phasenanteile, sowie geometrische

Parameter der Füllstoffpartikel betrachtet. Es stellt sich heraus, dass mit einer relativ geringen Anzahl experimenteller Designs eine gute Approximation der makroskopischen Wärmeleitfähigkeit erstellt werden kann. Der Füllgrad und die Phasenanteile erweisen sich neben dem Aspektverhältnis der plättchenförmigen Partikel als wesentliche Einflussgrößen. Als Optimierungsverfahren wird die Differentielle Evolutionsstrategie angewandt, um verschiedene optimale Mikrostrukturen zu ermitteln. Eine Validierung der Optimierungsergebnisse durch Auswertung des mikromechanischen Modells zeigt nur geringfügige Abweichungen. Anschließend werden als alternative Optimierungsmethoden ein gradientenbasiertes Optimierungsverfahren und ein sequentielles metamodellbasiertes Verfahren angewendet und mit dem präsentierten Ansatz verglichen. Eine Validierung der Homogenisierungsmethode anhand experimenteller Messungen zeigt eine gute Übereinstimmung. In Kapitel 5.2 wird die Methodik zur Optimierung der viskoelastischen Eigenschaften kurzfaserverstärkter Polymere eingesetzt. Neben dem Füllgrad werden die Faserorientierungsverteilung sowie die linear-elastischen Materialeigenschaften des Fasermaterials als Designvariablen betrachtet. Im Rahmen des Konzepts des Advani-Tucker-Faserorientierungstensors zweiter Stufe kann die Faserorientierungsverteilung durch lediglich zwei Parameter beschrieben werden, die innerhalb des Faserorientierungsdreiecks liegen. Zur Modellierung des viskoelastischen Verhaltens der Polymermatrix wird ein verallgemeinertes Maxwell-Modell verwendet und die Materialparameter werden anhand experimentell ermittelter Kriechkurven bestimmt. Auf Grundlage von Kriechsimulationen wird eine viskoelastische Materialdatenbank generiert. Diese wird zu Erstellung von Kriging-Interpolationen der orthotropen Komponenten des Kriechnachgiebigkeitstensors verwendet. Zur Lösung des Materialoptimierungsproblems wird die Differentielle Evolutionsstrategie unter Berücksichtigung des durch das Faserorientierungsdreieck beschränkten Designraums verwendet. Eine Validierung der Optimierungsergebnisse anhand des mikromechanischen Modells zeigt auch hier nur geringfügige Abweichungen. In Kapitel 5.3 wird die vorgeschlagene Methode schließlich zur Lösung multiphysikalischer Probleme eingesetzt. Um thermische und mechanische Anforderungen an den dreiphasigen Werkstoff simultan zu berücksichtigen wird ein Mehrzieloptimierungsproblem formuliert. Eine relativ große Anzahl von insgesamt zehn Designvariablen wird betrachtet, die neben dem Füllgrad und den Phasenanteilen die thermomechanischen Eigenschaften der Füllstoffe umfassen. Basierend auf der für thermische und mechanische Eigenschaften gesondert generierten Materialdatenbanken werden Kriging-Modelle zur Approximation der effektiven thermomechanischen Eigenschaften erstellt. Für die Optimierung wird ein genetischer Algorithmus auf den Metamodellen angewendet. Die Anwendung der Methode wird anhand zweier Beispiele demonstriert. Die Ergebnisse zeigen, dass durch Änderung der Phasenanteile die Wärmeausdehnung auf Kosten der thermischen Leitfähigkeit optimiert werden kann. Die Einhaltung eines maximalen makroskopischen E-Moduls in Form einer Nebenbedingung kann im Vergleich zum unrestringierten Problem durch Reduktion des E-Moduls der plättchenförmigen Partikel erreicht werden.

Die wesentlichen Erkenntnisse dieser Arbeit lassen sich wie folgt zusammenfassen: Die bei Einsatz globaler Optimierungsverfahren große Anzahl benötigter Funktionsauswertungen ist mit einem hohen numerischen Aufwand bedingt durch die Generierung repräsentativer Volumenelemente und der Simulation verschiedener Lastfälle verbunden. Aus diesem Grund wird in der vorliegenden Arbeit eine metamodellbasierte Optimierungsmethodik vorgeschlagen, die zum Teil überhaupt erst eine wirtschaftliche Lösung thermomechanischer Strukturoptimierungsprobleme ermöglicht. Weitere Vorteile dieser Methode liegen im effizienten Auffinden unterschiedlicher Designalternativen, der Berücksichtigung variierender Zieleigenschaften ohne die Notwendigkeit erneuter numerischer Simulationen, sowie der Bewertung der Robustheit verschiedener Designs und der Sensitivität individueller Parameter. Vorhandene Modelle können zudem um weitere physikalische Eigenschaften erweitert werden und bei multiphysikalischen Optimierungen eingesetzt werden. Im Gegensatz zu existierenden Arbeiten wird in dieser Arbeit eine ganzheitliche Prozesskette zur Optimierung physikalischer Parameter der Mikrostruktur partikelgefüllter und kurzfaserverstärkter Polymere präsentiert. Eine Validierung der mit dieser Methodik erhaltenen Optimierungsergebnisse durch Vergleich mit einer Auswertung des numerischen Modells zeigt bei den vorgestellten Beispielen nur geringfügige Abweichungen. Der Ansatz erweist sich als recht allgemeingültig und kann auch für andere Arten von Verbundwerkstoffen eingesetzt werden. In Kombination mit fortschrittlichen Fertigungstechniken und der Auswahl geeigneter Füllstoffe bietet die vorgeschlagene Methode das Potential den Produktentwicklungsprozess zu beschleunigen und die Anzahl zeitaufwändiger Experimente zu reduzieren.

Abstract

The selection of suitable materials represents a demanding task in the context of the increasing electrification of vehicles. This is mainly due to the fact that not only mechanical but also multiphysical requirements for the material properties have to be taken into account simultaneously. An example of this is the requirement for an electrically insulating yet good heat-conducting material with low thermal expansion. Polymer-based composites offer the possibility of specifically influencing the physical material properties by the use of suitable fillers. The macroscopic material properties result from the cause-effect principle: manufacturing process → structure → properties depending on the complex microstructure of the polymer matrix composite. The design of materials requires the consideration of this process chain in the reverse order and can be regarded as an inverse problem. Consequently, the design of such functional materials is diverse and sophisticated. The present work aims to answer the question of how the microstructure of composite materials must be tailored in order to exhibit the desired effective thermomechanical material behavior. A purely experimental development of such materials is generally a time-consuming and cost-intensive process, as many prototypes have to be produced and tested. Computer-aided multiscale methods enable a virtual characterisation of composites by a direct modelling of the heterogeneity at the microstructure level. These methods offer the potential to replace expensive experiments and to shorten the product development time. In the work at hand, a simulation-based optimization methodology for the design of functional materials is presented. For that purpose, a metamodel-based approach is proposed, which relies on the approximation of the structure-property relationship (SPR) in dependence of physical parameters of the microstructure. This enables an efficient solution of multiphysical material optimization problems in high-dimensional parameter spaces. The developed methodology is subsequently applied to the optimization of thermomechanical properties of particle reinforced and short fiber reinforced polymers.

Chapter 2 covers some basic aspects of continuum mechanics for the modeling of thermoelastic materials and heat conduction. The introduced notations and relations are applied in the following sections to compute effective material properties of composites by numerical simulation at the microscopic level.

In Chapter 3, the metamodel-based optimization methodology for the design of functional composites is presented. For this purpose, a structural optimization problem is

formulated for the material design. A description of the macroscopic material properties in terms of tensor quantities enables a consideration of direction-dependent (anisotropic) requirements imposed on materials. As design variables, physical parameters of the microstructure are selected, since these can be directly affected during the manufacturing process. These comprise parameters of the geometrical microstructure (e.g., the filler volume fraction) and the material properties (e.g., the Young's modulus) of the individual constituents. Several aspects such as the large computational effort and the influence of stochastic effects caused by the heterogeneous microstructure, motivate the development of the surrogate-based optimization methodology. This is based on an approximation of the SPR within the entire design space. A major advantage of such metamodels is the efficient use of global optimization methods compared to the direct application of the micromechanical simulation model, especially for high-dimensional problems. To create the metamodels, in a first step certain parameter combinations (experimental designs) are specified on the basis of an experimental design scheme. For each of these designs, a representative volume element is generated that represents the particular configuration of the microstructure. The corresponding effective material properties are computed by numerical homogenization under specification of periodic boundary conditions. As a result of these steps, a material database is provided that describes the SPR for a discrete set of parameterized microstructures. In the next step, the effective properties are approximated within the entire parameter space on the basis of this material data. Polynomial response surface models and Kriging interpolations are introduced for that purpose. The use of (global) sensitivity analysis methods to quantify the relative importance of the different design variables is discussed. Moreover, a simple concept for the evaluation of the robustness of the designs and for robust optimization is presented.

Chapter 4 provides a compact overview of particle reinforced and short fiber reinforced polymers. In addition to a description of the matrix and filler materials relevant for technical applications and their influence on the macroscopic properties, the manufacturing and application areas of these materials are briefly discussed.

In Chapter 5, the metamodel-based optimization method is demonstrated by means of specific material examples. For that purpose, in Section 5.1 a three-phase particle reinforced material with large contrast in the thermal conductivities of the individual constituents is considered, where a certain thermal conductivity is to be adjusted. The filler volume fraction and phase fractions as well as geometrical parameters of the filler particles are considered as design variables. It turns out that with a relatively small number of samples a reasonably good approximation of the macroscopic thermal conductivity can be obtained. The filler volume fraction and the phase fractions prove to be significant influencing variables, in addition to the aspect ratio of the platelet-shaped particles. As optimization method, differential evolution is employed to determine different optimal microstructures. A validation of the optimization results by an evaluation of the

micromechanical model shows only slight deviations. Subsequently, a gradient-based optimization method and a sequential metamodel-based method are utilized as alternative optimization methods and are compared with the presented approach. A validation of the homogenization method by experimental measurements shows a satisfactory agreement. In Section 5.2, the methodology is applied to optimize the viscoelastic properties of short fiber reinforced polymers. In addition to the fiber volume fraction, the fiber orientation distribution and the linear elastic material properties of the fiber material are considered as design variables. Within the concept of the second-order Advani-Tucker fiber orientation tensor, the fiber orientation distribution can be described by only two parameters lying within the fiber orientation triangle. A generalized Maxwell model is used to model the viscoelastic behavior of the polymer matrix and the corresponding material parameters are determined based on experimentally determined creep curves. A viscoelastic material database is established from the results of creep simulations. This is used to create Kriging interpolations of the orthotropic components of the creep compliance tensor. Differential evolution is employed to solve the material optimization problem considering the constrained design space imposed by the fiber orientation triangle. A validation of the optimization results using the micromechanical model shows only minor deviations here as well. Finally, the proposed method is applied to solve multiphysical optimization problems in Section 5.3. To consider thermal and mechanical requirements of the three-phase material simultaneously, a multi-objective optimization problem is formulated. A relatively large number of ten design variables are considered, which include the thermomechanical properties of the fillers in addition to the filler volume fraction and the phase fractions. Based on the material databases generated separately for thermal and mechanical properties, Kriging models are created to approximate the effective thermomechanical properties. An genetic algorithm is applied to the metamodels for optimization. The application of the method is demonstrated by two examples. The results show that by changing the phase fractions, the thermal expansion can be optimized at the expense of the thermal conductivity. Compared to the unrestricted problem, compliance with a maximum macroscopic Young's modulus in the form of a constraint can be achieved by reducing the Young's modulus of the platelet-shaped particles.

The main findings of this work can be summarized as follows: The large number of function evaluations required when using global optimization methods is associated with a large numerical effort caused by the generation of representative volume elements and the simulation of different load cases. For this purpose, a surrogate-based optimization methodology is proposed in that work, which partly enables an economical solution of thermomechanical structural optimization problems at all. Further advantages of this method are the efficient identification of different design alternatives, the consideration of varying target properties without the necessity of renewed numerical simulations, as well as the evaluation of the robustness of different designs and the sensitivity of

individual parameters. Existing models can also be extended to include other physical properties and can be used for multiphysical optimization. In contrast to existing works, this thesis presents a holistic process chain for the optimization of physical parameters of the microstructure of particle reinforced and short fiber reinforced polymers. A validation of the optimization results obtained with this methodology by comparison with an evaluation of the numerical model shows only minor deviations for the presented examples. The approach proves to be quite general and can also be applied to other types of composite materials. In combination with advanced manufacturing techniques and the selection of suitable fillers, the proposed method offers the potential to accelerate the product development process and to reduce the number of time-consuming experiments.

Table of Contents

Chapter 1

Introduction

1.1 Motivation

In connection with the increasing electrification of vehicles, novel, challenging, and partly contradictory requirements are placed on the physical properties of materials. In this context, it is generally not sufficient to limit the consideration to individual, e.g., mechanical properties. In fact, multiphysical material requirements must be taken into account simultaneously. An example of this is the demand for an electrically insulating yet well thermally conductive material with low thermal expansion.

Polymer matrix composites offer the potential to modify and optimize the physical material properties by the use of suitable fillers. The application of polymers as matrix material is primarily motivated by their low density, easy processability, and low costs. The inherently low thermal conductivity of polymers (typically in the range of 0.1 - 0.5 W/mK) can be significantly increased by adding thermally conductive filler particles. Such particle reinforced polymers (PRPs) are therefore primarily used in the field of power electronics, where adequate heat dissipation is necessary to ensure proper functionality. Short fiber reinforced polymers (SFRPs) exhibit outstanding mechanical properties in terms of high stiffness and strength in relation to their weight. This makes them a predestined material for lightweight construction applications, which is increasingly replacing other materials such as metals.

The **macroscopic material properties** result from the partially complex microstructure of the polymer composite. The most important factors comprise the physical material properties of the individual constituents as well as geometrical parameters of the microstructure such as the filler volume fraction and the dispersion of the fillers (e.g., the orientation of fibers) within the polymer matrix. The computation of the overall properties of a particular microstructural configuration is often referred as the forward problem or the structural analysis problem. For technical applications, it is often possible to concretely quantify the desired physical material properties required for the performance of a product. These properties are often the result of a multiphysical optimization at the component (macroscopic) level. This means that the conventional direction in

which information flows in materials science: processing → structure → property → performance [131], [130] should ideally occur in the opposite direction. To this end, the essential aim of this work consists in the developement of an optimization methodology for the design of functional composites. This should be illustrated by the following example: Consider a component consisting of a PRP as depicted in Fig. 1.1. Let $\boldsymbol{\Psi}_{\text{eff}}$ denote a generic macroscopic property depending on parameters of the heterogeneous microstructure such as the filler volume fraction V_f and the material properties of the filler $\boldsymbol{\Psi}_1$ and the polymer $\boldsymbol{\Psi}_2$, i.e., $\boldsymbol{\Psi}_{\text{eff}} = \boldsymbol{\Psi}_{\text{eff}}(\boldsymbol{\Psi}_1, V_f, \boldsymbol{\Psi}_2, ...)$. Please note that there are also other influencing variables (indicated by the dots), which will be explained in the further course of the work. The task in the inverse problem is to adjust these parameters so that the microstructure exhibits the desired macroscopic material property $\boldsymbol{\Psi}^*_{\text{eff}}$. The need to exchange information across different length scales in material design is extensively described within the integrated computational materials engineering (ICME) [133] paradigm. In the work at hand, in addition to the simultaneous consideration of multiphysical material properties, a specific anisotropic material behavior should also be taken into account. It has to be kept in mind that the optimization of a certain material property can lead to a deterioration of another material property. In the following, a brief overview of the state of the art for the determination of the overall properties of composites and for material optimization is provided.

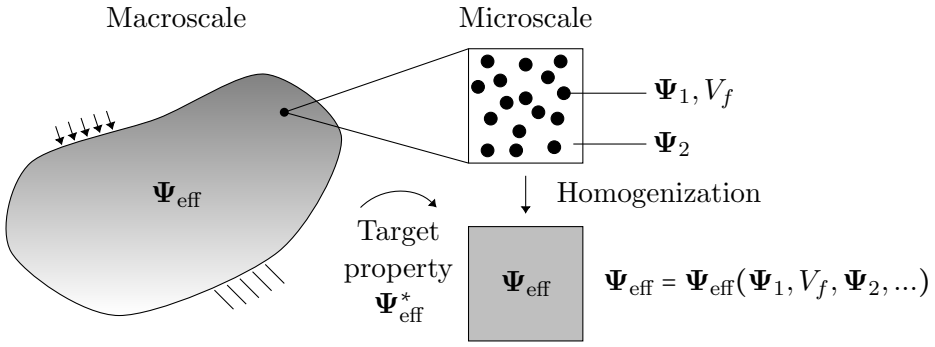

Figure 1.1: Linkage of macro- and microscale: Dependence of a macroscopic material property on physical parameters of the heterogeneous microstructure

1.2 State of the art

Experimental test procedures are usually employed in practice to determine the overall properties of composites. However, this only allows the consideration of a certain material at a time. Furthermore, it may be impractical to manufacture specific microstructural configurations due to process-related reasons. Pure experimental development of such functional materials is therefore usually quite costly and time-consuming

and represents a tedious trial-and-error process.

Analytical homogenization methods have been established for the determination of macroscopic properties of heterogeneous materials. A common class of approximation methods is given by the so-called mean field approaches. These are based on the inclusion theory of Eshelby [43] and basically assume elliptical inclusions embedded within a matrix material. Another class of homogenization approaches provides theoretical upper and lower bounds of the effective properties of composites. For example, the simple rule of mixture is obtained by averaging the individual properties of the constituents weighted by their volume faction. They do not take into account the morphology of the microstructure and often provide a very rough estimate, especially for large contrasts in the material properties of the constituents. More complex microstructures and the interaction of physical effects at large filler volume fractions cannot be captured accurately enough with this methods for the materials considered in this work.

To overcome these drawbacks, **multiscale computational homogenization methods** [51] were developed. These are based on the geometrical and physical modeling of the microstructure of the composite on the microscale. A direct resolution of the heterogeneity on the macroscopic (component) level would be computationally far too expensive. Because of that, computational homogenization methods employ so-called representative volume elements (RVEs) which capture the local microstructural setting and are attached to each macroscopic point. Suitable simulation software [14] offer the possibility to compute the macroscopic properties in terms of appropriate averaging (homogenization) relations. This is based on the formulation of boundary value problems (BVPs) on the RVE level and its solution by numerical methods such as the finite element method (FEM). Besides the use of FEM, fast Fourier transform (FFT)-based techniques [121], [122] operating on a regular voxel grid represents a more efficient numerical method. This simulation-based approach enables the consideration of different microstructural configurations in short time and offers the potential to shorten the product development time. Hence, such computational homogenization methods are utilized in the work at hand.

Topology optimization (TO) methods have been applied for the design of heterogeneous materials [178]. In [76], a numerical method for addressing different physical demands on effective properties of composites is presented. TO methods were employed, for example, to identify structures for maximum thermal and electrical conductivity [180] and extreme thermal expansion [165]. From a practical point of view, a drawback of TO is that the resulting structures are difficult to realize by traditional processing techniques. This is mainly caused by the complex morphology of the resulting structures and the dependence on conventional fillers. For this reason, topology optimization is not further considered in the current work.

Microstructure-sensitive design (MSD) [3] has been established as a very generic paradigm for the design of microstructures. MSD is based on spectral representations of statistical distribution functions yielding the microstructure hull (i.e., the complete set of relevant microstructural designs). Starting from this representation, homogenization relations are formulated which delineate a so-called property closure [49]. This property closure enables the inverse design by the identification of microstructures with target properties. Because MSD is based on spectral representations, it is especially suitable for the design of anisotropic, polycrystalline materials and is therefore not further investigated in the work at hand.

In recent years, **machine learning (ML)** techniques [143] have been gaining much popularity for the design and analysis of materials at different length and time scales. Commonly, surrogate models [168], a special case of supervised learning models, are established to model the unknown structure-property relationship (SPR). These models rely on the use of training data and require the selection of descriptors (input parameters) for the representation of the material system (e.g., the material composition or the morphology of microstructures), which are linked to corresponding material properties (output parameters). Such surrogate models are used to replace physical models such as experiments or numerical simulations and offer the advantage of an efficient prediction and parametric optimization by the use of optimization algorithms. Nowadays, surrogate models are often trained with data from computer simulations. This is partly due to recent advances in computing power, data acquisition and storage, ML algorithms as well as material models. Propelled at least by the Material Genome Initiative [109], a plethora of research articles concerning the application of ML in materials science has been published over the last two decades. Most of them rely on the use of density functional theory or molecular dynamics methods (considering phenomena occuring at a lower length scale as regarded in this work) to generate training data for the ML model to predict corresponding material properties. High-throughput computations [35] have been applied to generate large amounts of data. This led to the emergence of open source databases such as the open quantum material database [151] or Materialsmine - a database for nanocomposites (Nanomine [25], mostly created by experimental data) and mechanical metamaterials (Metamine). An overview of such interdisciplinary "material informatic" approaches can be found in one of the numerous articles, e.g., [103], [184] or [5].

The following review focuses on current research on ML techniques for the optimization of effective material properties of microstructured materials. In [193] and [194], a physical descriptor-based methodology for the design of heterogeneous materials is proposed. State-of-the-art (ML) methods such as design of experiments (DoE), surrogate modeling, sensitivity analysis, and multi-objective optimization are used to identify optimal microstructures. Based on training data obtained from latin hypercube sam-

pling (LHS), a Kriging surrogate model is constructed to accelerate the optimization procedure using a genetic algorithm. Bessa et al. [18] developed a data-driven computational framework for the analysis of material systems and structures. Its essential steps integrate DoE (sampling), computational analysis (numerical homogenization) of each sample leading to a material database, and the creation of an ML model on the basis of this database. Three different types of descriptors, geometrical microstructure descriptors, material property descriptors, as well as boundary condition descriptors are investigated. Neural networks and Kriging models are utilized as ML models trained on data generated by space-filling sampling schemes such as the Sobol' sequence and LHS. These models serve as multiscale models and depict the (nonlinear) macroscopic constitutive material behavior. The possibility of using these models for optimization is mentioned, but not further elaborated. Further recent attempts for the design of microstructured materials make use of deep neural networks [9], generative adversarial networks [198], and convolutional neural networks [2]. Beside the application to mechanical properties, in [59] an ML model is generated to optimize the thermal conductivity of a particle reinforced composite. Recently, Chen et al. [32] proposed a data-centric approach for the design of microstructural material systems. This contains elements of design representation, design evaluation, and design synthesis. Computational methods for each of these elements are presented. A latent variable Gaussian process model [202] introduced by some of the authors to handle both qualitative and quantitative variables for design representation is used as surrogate model. For design synthesis, a Bayesian optimization approach is used, which employs an adaptive sampling technique to identify the global optimum in an efficient way. In [79], this approach is used for mixed-variable multicriteria optimization of nanocomposites. A recent overview of ML methods utilized for the analysis and design of polymer composite materials is given in [164]. Apart from the aforementioned works, research dealing with such parametric material optimization problems for composites is still limited. Gu and Chen [30] indicated that ML models have been used mainly for predicting the properties of composites rather than for the design of new materials. General purpose frameworks for solving such multiphysical material optimization problems for polymer matrix composites are currently still lacking.

1.3 Scope and outline

The main goal of this work is the development of an optimization methodology for the design of functional materials according to multiphysical requirements. The focus will be placed on the thermomechanical material properties of particle reinforced and short fiber reinforced polymers. In addition to the application of the methodology for the optimization of thermal and mechanical properties, the simultaneous consideration of thermomechanical properties by multi-objective optimization methods is considered. Robustness evaluation and robust optimization aspects are also taken into account. It

should be emphasized that the developed surrogate models can also serve as multiscale material models as input for component simulations. However, the focus of this work is on the adjustment of specific, generally anisotropic thermomechanical material properties. The approach proves to be quite general and can also be applied to other composite materials and other physical (e.g., electromagnetic) material properties. The optimization results can be incorporated into the manufacturing process by tailoring the microstructure using appropriate processing techniques.

This thesis is organized as follows: Chapter 2 covers some basic principles of continuum mechanics, including the constitutive modeling of linear thermoelastic materials and the description of heat conduction problems. The notation used in the context of computational homogenization is introduced.

Chapter 3 provides the surrogate-based multiscale optimization method for the design of functional composites and represents the methodological background of this work. The material design problem is formulated in terms of a parametric optimization problem in the standard setting of nonlinear structural optimization problems. Based on the characteristics of this problem, the concept of the surrogate-based optimization methodology is developed. In the further sections, the individual elements of the framework are described in greater detail. This includes a brief overview of homogenization and optimization methods. The essential steps include DoE, the generation of RVEs, surrogate modeling, and global optimization. Moreover, sensitivity analysis methods and a robust design method are presented.

Chapter 4 deals with the polymer matrix composites investigated in this thesis. Some basic aspects of particle reinforced and short fiber reinforced polymers are addressed. This includes technically relevant matrix and filler materials and their influence on the overall properties.

In Chapter 5, the optimization framework is demonstrated by means of specific material examples. A three-phase PRP is investigated with view of its thermomechanical properties. In the first example, the method is applied to identify different microstructures of that material with a specific effective thermal conductivity [107]. The demand of different physical material requirements in a multiphysics setting is addressed by adopting the surrogate-based method and the use of multi-objective optimization techniques. Furthermore, the framework is employed for the optimization of the overall viscoelastic behavior of SFRPs [106].

Finally, Chapter 6 summarizes the main results. An outlook to future work is given.

Chapter 2

Foundations of continuum mechanics and heat conduction

2.1 Continuum mechanics

This section focuses on the modeling of linear thermoelastic materials and the description of heat conduction problems. For this purpose, some basic concepts of continuum mechanics in the form of kinematic relations, balance equations, and constitutive models are briefly reviewed and the notation used in the remainder of this work is introduced. The inferred relations apply both at the macroscopic level and at the microscale, introduced later in the context of homogenization. For a more comprehensive description of continuum mechanics approaches, the reader is referred to, e.g., [61] or [69].

2.1.1 Kinematics

The motion and deformation of a body under the action of forces is given in terms of kinematic relations. This is illustrated in Fig. 2.1. The position of a material point in the reference (undeformed) configuration Ω_0 at time $t = t_0$ is denoted by the position vector $\boldsymbol{X} \in \mathbb{R}^3$. The position of a material point $\boldsymbol{x} \in \mathbb{R}^3$ in the current (deformed) configuration Ω_t at time $t > t_0$ is described by a nonlinear deformation map

$$\boldsymbol{x} = \boldsymbol{\varphi}(\boldsymbol{X}, t) \tag{2.1}$$

with respect to the reference configuration. Based on this mapping, the displacement vector $\boldsymbol{u}$ is defined as the difference of the position vectors of current and reference configuration

$$\boldsymbol{u} = \boldsymbol{x}(\boldsymbol{X}, t) - \boldsymbol{X}. \tag{2.2}$$

For the description of deformation processes, the deformation gradient

$$\boldsymbol{F} = \frac{\partial \boldsymbol{x}}{\partial \boldsymbol{X}} \tag{2.3}$$

and the displacement gradient

$$\boldsymbol{H} = \frac{\partial \boldsymbol{u}}{\partial \boldsymbol{X}} = \boldsymbol{F} - \boldsymbol{I} \tag{2.4}$$

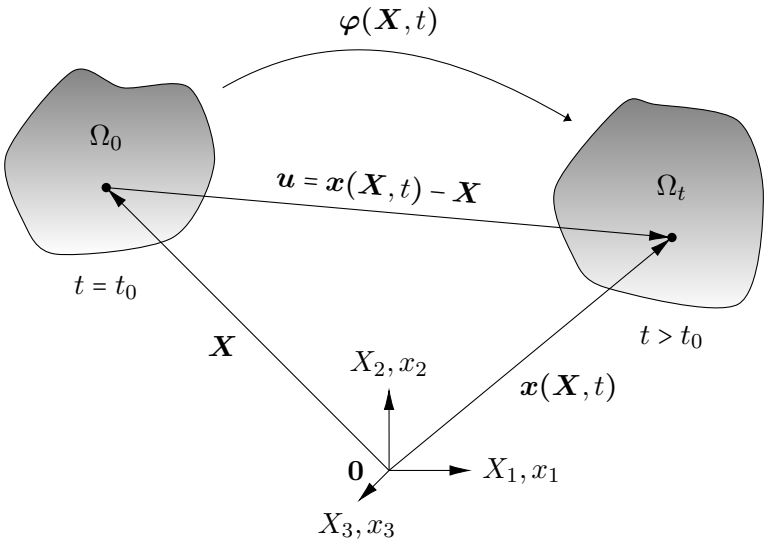

Figure 2.1: Kinematics of rigid bodies

are introduced, where $\boldsymbol{I}$ denotes the second order identity tensor. By means of the deformation gradient, a transformation between infinitesimal material lines, surfaces, and volume elements [7] from the current to the reference configuration can be described as

$$\begin{aligned} \mathrm{d}\boldsymbol{x} &= \boldsymbol{F}\,\mathrm{d}\boldsymbol{X}, \\ \boldsymbol{n}\,\mathrm{d}a &= J\boldsymbol{F}^{-T}\boldsymbol{N}\,\mathrm{d}A, \\ \mathrm{d}v &= J\,\mathrm{d}V \end{aligned} \tag{2.5}$$

with the determinant of the deformation gradient $J = \det(\boldsymbol{F}) > 0$ and the outward normal $\boldsymbol{n}$ of the surface area $\mathrm{d}a$. Another measure of the deformation state is given by the Green-Lagrange strain tensor

$$\boldsymbol{E} = \frac{1}{2}(\boldsymbol{F}^T\boldsymbol{F} - \boldsymbol{I}) = \frac{1}{2}(\boldsymbol{H} + \boldsymbol{H}^T + \boldsymbol{H}^T\boldsymbol{H}). \tag{2.6}$$

The definition of $\boldsymbol{E}$ is motivated to describe the difference between the squares of infinitesimal material line elements from the reference to the current configuration. Due to its definition, rigid body motions are not considered and $\boldsymbol{E}$ vanishes for this case. If the displacement gradient is small ($\|\boldsymbol{H}\| \ll 1$), $\boldsymbol{H}^T\boldsymbol{H}$ in (2.6) becomes negligible and the theory of small deformations is obtained. This results in the linearized strain tensor $\boldsymbol{\epsilon}$, which is given by the symmetric part of the displacement gradient, i.e.,

$$\boldsymbol{\epsilon} = \frac{1}{2}\left(\boldsymbol{H} + \boldsymbol{H}^T\right) = \frac{1}{2}\left(\nabla\boldsymbol{u} + \nabla^T\boldsymbol{u}\right). \tag{2.7}$$

In the context of this work, the validity of the theory of small deformations is assumed. In this case, both configurations coincide, so no distinction has to be made and all observation relate to the same configuration Ω in the following. Due to the symmetry of $\boldsymbol{\epsilon}$, a common notation, which is also used later in this work, is the Voigt notation. In Voigt notation, $\boldsymbol{\epsilon}$ can be expressed as a vector $\boldsymbol{\epsilon}_V \in \mathbb{R}^6$ by

$$\boldsymbol{\epsilon}_V = (\epsilon_{11},\ \epsilon_{22},\ \epsilon_{33},\ 2\epsilon_{23},\ 2\epsilon_{13},\ 2\epsilon_{12})^T. \tag{2.8}$$

2.1.2 Balance equations

To describe the deformations inside a body under the action of external forces, the static balance equation is employed. For their derivation, a deformable body (with density ρ) associated with the domain Ω and the boundary $\partial\Omega$ as shown in Fig. 2.2 is considered.

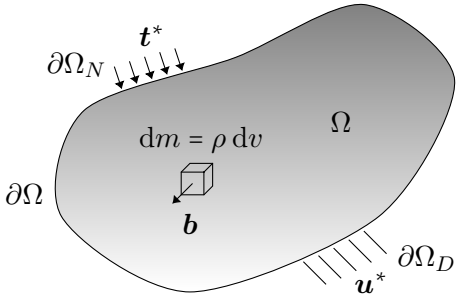

Figure 2.2: Solid body under the action of volume and surface forces

The regarded mechanical forces are volume forces $\boldsymbol{f} = \rho\boldsymbol{b}$ (per unit volume $\mathrm{d}v$) acting inside the body and surface tractions $\boldsymbol{t}$ acting on $\partial\Omega$. If static problems are considered (neglecting inertia forces), the balance of linear momentum yields

$$\underbrace{-\int_{\partial\Omega} \boldsymbol{t}\,\mathrm{d}a}_{\text{surface tractions}} = \underbrace{\int_{\Omega} \boldsymbol{f}\,\mathrm{d}v}_{\text{body forces}}, \tag{2.9}$$

i.e., the equilibrium of volume and surface forces. Substituting the traction vector $\boldsymbol{t}$ by Cauchy's stress theorem $\boldsymbol{t} = \boldsymbol{\sigma}\cdot\boldsymbol{n}$ with the Cauchy stress tensor $\boldsymbol{\sigma}$ and the outward normal $\boldsymbol{n}$ of the surface area $\mathrm{d}a$, this leads to

$$-\int_{\partial\Omega} \boldsymbol{\sigma}\cdot\boldsymbol{n}\,\mathrm{d}a = \int_{\Omega} \boldsymbol{f}\,\mathrm{d}v. \tag{2.10}$$

Applying Gauss' divergence theorem, the surface integral in (2.10) can be transformed into a volume integral, so (2.9) can be written as

$$-\int_{\Omega} (\operatorname{div}\boldsymbol{\sigma})\,\mathrm{d}v = \int_{\Omega} \boldsymbol{f}\,\mathrm{d}v. \tag{2.11}$$

Since (2.11) is valid for arbitrary volumes Ω, the local form of the static balance equation is given as

$$-\operatorname{div}\boldsymbol{\sigma} = \boldsymbol{f}. \tag{2.12}$$

Moreover, the symmetry of the Cauchy stress tensor $\boldsymbol{\sigma} = \boldsymbol{\sigma}^T$ results from the balance of angular momentum

$$\int_{\partial\Omega} \boldsymbol{x} \times \boldsymbol{t}\, \mathrm{d}a + \int_{\Omega} \boldsymbol{x} \times \boldsymbol{f}\, \mathrm{d}v = \boldsymbol{0}, \tag{2.13}$$

so $\boldsymbol{\sigma}$ can be expressed in Voigt notation $\boldsymbol{\sigma}_V = (\sigma_{11},\ \sigma_{22},\ \sigma_{33},\ \sigma_{23},\ \sigma_{13},\ \sigma_{12})^T \in \mathbb{R}^6$ too.

2.1.3 Linear thermoelasticity

The connection between stresses and strains describes the mechanical material behavior and is expressed in form of constitutive equations. In linear elasticity, the stresses and strains are related via Hooke's law

$$\boldsymbol{\sigma}_V = \boldsymbol{C}_V \cdot \boldsymbol{\epsilon}_V \tag{2.14}$$

by a symmetric stiffness tensor $\boldsymbol{C}_V \in \mathbb{R}^{6\times 6}$ (in Voigt notation). The inverse relation is given as $\boldsymbol{\epsilon}_V = \boldsymbol{S}_V \cdot \boldsymbol{\sigma}_V$ with the compliance tensor $\boldsymbol{S}_V = \boldsymbol{C}_V^{-1}$. For isotropic materials, $\boldsymbol{\sigma}$ can be expressed as

$$\boldsymbol{\sigma} = \lambda \operatorname{tr}(\boldsymbol{\epsilon})\boldsymbol{I} + 2\mu\boldsymbol{\epsilon} \tag{2.15}$$

and $\boldsymbol{C}$ is defined by two parameters, the so-called Lamé constants λ and μ. The Lamé constants can also be expressed in terms of the Young's modulus E and the Poisson's ratio ν,

$$\lambda = \frac{E\nu}{(1+\nu)(1-2\nu)} \quad \text{and} \quad \mu = \frac{E}{2(1+\nu)} \tag{2.16}$$

commonly used in engineering applications.

A thermoelastic material is subjected to strains under a variation of temperature. The total strain $\boldsymbol{\epsilon}$ can be expressed as the sum of an elastic $\boldsymbol{\epsilon}_{\mathrm{el}}$ and an thermal part $\boldsymbol{\epsilon}_{\mathrm{therm}}$ as

$$\boldsymbol{\epsilon} = \boldsymbol{\epsilon}_{\mathrm{el}} + \boldsymbol{\epsilon}_{\mathrm{therm}} \tag{2.17}$$

and $\boldsymbol{\epsilon}_{\mathrm{therm}}$ is given by

$$\boldsymbol{\epsilon}_{\mathrm{therm}} = \boldsymbol{\alpha} \cdot \Delta T \tag{2.18}$$

with the (linearized) thermal expansion tensor $\boldsymbol{\alpha}$ and a small temperature change $\Delta T = T - T_0$ with the current temperature T and a reference temperature T_0. Thus, the constitutive material law (in Voigt notation) is given in terms of the Duhamel-Neumann law

$$\boldsymbol{\sigma}_V = \boldsymbol{C}_V \cdot \boldsymbol{\epsilon}_{V,\mathrm{el}} = \boldsymbol{C}_V \cdot (\boldsymbol{\epsilon}_V - \boldsymbol{\alpha}_V \cdot \Delta T). \tag{2.19}$$

2.2 Heat conduction

This section deals with the modeling of heat conduction in solid bodies. In the following, it is assumed that the volume change remains small due to the thermal expansion, i.e., the process is considered to be isochoric. The heat conduction equation can be derived from the energy balance equation (first law of thermodynamics). Considering a closed system on which no external mechanical forces act, this states the change in internal energy is equal to the heat transfer rate. In integral form, this can be expressed as

$$\underbrace{\frac{\mathrm{d}}{\mathrm{d}t}\int_\Omega \rho u \,\mathrm{d}v}_{\text{change of internal energy}} = \underbrace{\int_\Omega \rho r \,\mathrm{d}v}_{\text{heat source/sink}} - \underbrace{\int_{\partial\Omega} \boldsymbol{q}\cdot\boldsymbol{n}\,\mathrm{d}a}_{\text{heat flow over boundary}} \tag{2.20}$$

with the specific internal energy u. The heat transfer rate is given by the heat added or removed by heat sources or sinks r and the heat flux through $\partial\Omega$ expressed by the heat flux vector $\boldsymbol{q}(\boldsymbol{x}) \in \mathbb{R}^3$. Utilizing the same arguments as in the previous subsection, the local form of (2.20) is given as

$$\rho\frac{\mathrm{d}u}{\mathrm{d}t} = -\operatorname{div}\boldsymbol{q} + \rho r. \tag{2.21}$$

A constitutive law of heat conduction is given in the form of Fourier's law

$$\boldsymbol{q} = -\boldsymbol{k}\cdot\nabla T. \tag{2.22}$$

In 2.22, $\boldsymbol{k}$ denotes the symmetric second-order thermal conductivity tensor. For isotropic materials, $\boldsymbol{k}$ reduces to a scalar value, i.e., $\boldsymbol{k} = k\boldsymbol{I}$, which states that the heat flux $\boldsymbol{q}$ in Ω is proportional to the negative temperature gradient $-\nabla T$. Moreover, the change of internal energy is given as $\mathrm{d}u = c_v\,\mathrm{d}T$ with the specific heat capacity $c_v = c_v(T)$ as material parameter. Substituting these two material laws into (2.21), the following expression for the heat conduction equation in homogeneous and isotropic materials is obtained:

$$\rho c_v\frac{\mathrm{d}T}{\mathrm{d}t} = \operatorname{div}\left(k\cdot\nabla T\right) + \rho r. \tag{2.23}$$

Please note that k depends on the temperature for some materials. If steady-state heat conduction is considered and in the absence of heat sources/sinks r, the heat conduction equation (2.23) reduces to Laplace's equation:

$$\Delta T = 0. \tag{2.24}$$

To summarize, Table 2.1 compares the field quantities and governing equations used to describe elastostatic and steady-state heat conduction problems. Also provided are the boundary conditions (BCs) that must be specified to solve the differential equations 2.12 and 2.24.

Table 2.1: Comparison of field quantities and governing equations including BCs for elastostatic and steady-state heat conduction problems

Elastostatics	**Steady-state heat conduction**
Field quantities	
Displacement vector $\boldsymbol{u}$	Temperature T
Strain tensor $\boldsymbol{\epsilon}$	Temperature gradient ∇T
Stress tensor $\boldsymbol{\sigma}$	Heat flux vector $\boldsymbol{q}$
Governing equations	
$\boldsymbol{\epsilon} = \frac{1}{2}\left(\nabla \boldsymbol{u} + \nabla^T \boldsymbol{u}\right)$	∇T
$\boldsymbol{\sigma} = \boldsymbol{C} : \boldsymbol{\epsilon}$	$\boldsymbol{q} = -\boldsymbol{k} \cdot \nabla T$
$\operatorname{div} \boldsymbol{\sigma} + \boldsymbol{f} = \boldsymbol{0}$	$\operatorname{div} \boldsymbol{q} = \boldsymbol{0}$
Boundary conditions	
$\boldsymbol{\sigma} \cdot \boldsymbol{n} = \boldsymbol{t}^{bc}$	$\boldsymbol{q} \cdot \boldsymbol{n} = \boldsymbol{q}^{bc}$
$\boldsymbol{u} = \boldsymbol{u}^{bc}$	$T = T^{bc}$
Energy	
$W_{el} = \frac{1}{2}\boldsymbol{\epsilon} : \boldsymbol{C} : \boldsymbol{\epsilon}$	$\Delta Q = m \cdot c_v \cdot \Delta T$

There can be distinguished between two basic types of BCs: Dirichlet BCs are given by specification of displacements $\boldsymbol{u}^{bc} = \boldsymbol{u}$ or temperatures $T^{bc} = T$ acting on the Dirichlet boundary $\partial\Omega_D$, while Neumann BCs comprise predefined tractions $\boldsymbol{t}^{bc} = \boldsymbol{\sigma} \cdot \boldsymbol{n}$ or heat fluxes $\boldsymbol{q}^{bc} = \boldsymbol{q} \cdot \boldsymbol{n}$ acting on the Neumann boundary $\partial\Omega_N$. These must be defined on the entire boundary $\partial\Omega = \partial\Omega_D \cup \partial\Omega_N$. A combination of both BCs on disjoint subsets ($\partial\Omega_D \cap \partial\Omega_N = \varnothing$) represent mixed BCs, see Fig. 2.2 for a schematic illustration in elastostatics.

Chapter 3

Surrogate-based multiscale optimization method

This chapter concerns with the proposed surrogate-based multiscale optimization method for the design of composite materials. A formulation of the material optimization problem in terms of physical descriptors of microstructured materials is introduced. Based on a characterization of this optimization problem, the surrogate-based optimization framework and its individual steps are explained in more detail in the following sections.

3.1 Formulation of the material optimization problem

In the following, the selection of design variables for the representation of a microstructural design is outlined (Section 3.1.1). In order to obtain materials with target properties, these design variables are used for the formulation of a parametric optimization problem, which is introduced and characterized in Section 3.1.2.

3.1.1 Parameterization of microstructured materials

In order to describe the processing-structure-property relationship [28] of a composite material, microstructure characterization and reconstruction (MCR) techniques have been developed. Following [21], MCR techniques can be categorized into five categories: (1) statistical functions, (2) physical descriptors, (3) spectral density functions, (4) ML-based, and (5) texture synthesis and multiple-point statistic-based methods. According to the aim of this thesis, suitable design variables have to be chosen for the formulation of a structural optimization problem. Descriptors from the categories (1), (4), and texture synthesis are generally not applicable for material design, as they do not yield design variables that are necessary for the formulation of a structural optimization problem [21]. Spectral density function descriptors are used for example for crystals to describe the microstructure hull in the context of microstructure-sensitive design [3]. The most convenient yet capable category for material design is the physical descriptor-based method [193], [194], [59]. In this thesis, physical descriptors are considered, because these can be adjusted by locally influencing the microstructure during the manufacturing process. For

the describtion of a microstructured material by physical descriptors, three stages can be considered [193], allowing an increasingly detailed description of the microstructure: Composition of the constituents, spatial distribution (dispersion), and geometry of the filler particles. For the description of the SPR, the design variables are classified into two categories in the context of this work: Design variables of the geometrical microstructure and physical material property descriptors. The geometrical microstructure descriptors represent the geometrical setting (the morphology) of the microstructure. Examples of design variables of the geometrical microstructure are the filler volume fraction, the dispersion of the fillers within the matrix, and the shape and size of the filler particles. The material property descriptors typically comprise material parameters that are used to specify the constitutive material behavior of the individual constituents. Considering linear (isotropic) materials, these can be, e.g., the thermal conductivity k, the Young's modulus E and the Poisson's ratio ν, or the coefficient of thermal expansion α. The parameterization of a microstructured material is demonstrated by the following example: A random heterogeneous material composed of spherical filler particles suspended in a polymer matrix is investigated. For the representation of the geometrical microstructure, the filler volume fraction V_f and the mean diameter d_{sp} of the spherical particles are selected as design variables. As material property descriptors, the thermal conductivity k_m of the matrix material and the filler k_p are investigated. Fig. 3.1 shows a realization of this microstructure in form of a RVE represented by the design variables vector $\boldsymbol{d} = (V_f,\, d_{sp},\, k_m,\, k_p)$. Each design variable requires the specification of physically meaningful upper and lower bounds. The dispersion of the filler particles in the matrix was specified here as uniform. Further examples of parameterized structures are given in Chapter 5.

3.1.2 Formulation and characterization of the material optimization problem

In order to find an optimal microstructural design with target macroscopic properties, the following parametric minimization problem for the design variables $\boldsymbol{d}$ is introduced:

$$\begin{aligned} J(\boldsymbol{d}) &= \left(\frac{\left\| \boldsymbol{\Psi}_{\text{eff}}(\boldsymbol{d}) - \boldsymbol{\Psi}^*_{\text{eff}} \right\|_2}{\left\| \boldsymbol{\Psi}^*_{\text{eff}} \right\|_2} \right)^2 \rightarrow \min, \quad \boldsymbol{d} \in \mathbb{R}^n \\ \text{s. t.} \qquad & d_{i,low} \leq d_i \leq d_{i,up}. \end{aligned} \tag{3.1}$$

In (3.1), $J = J(\boldsymbol{d})$ denotes an objective function to be minimized involving the effective property of interest $\boldsymbol{\Psi}_{\text{eff}} = \boldsymbol{\Psi}_{\text{eff}}(\boldsymbol{d})$ as a tensor quantity as a function of the design variables $\boldsymbol{d}$ and $\boldsymbol{\Psi}^*_{\text{eff}}$ represents the target effective material property. As effective properties, the thermal conductivity $\boldsymbol{k}_{\text{eff}}$, the linear elastic stiffness $\boldsymbol{C}_{\text{eff}}$, and the thermal expansion $\boldsymbol{\alpha}_{\text{eff}}$ will be investigated in that work. Formulation (3.1) allows a consideration of the full anisotropic material behavior, which is essential in the work at hand to design materials

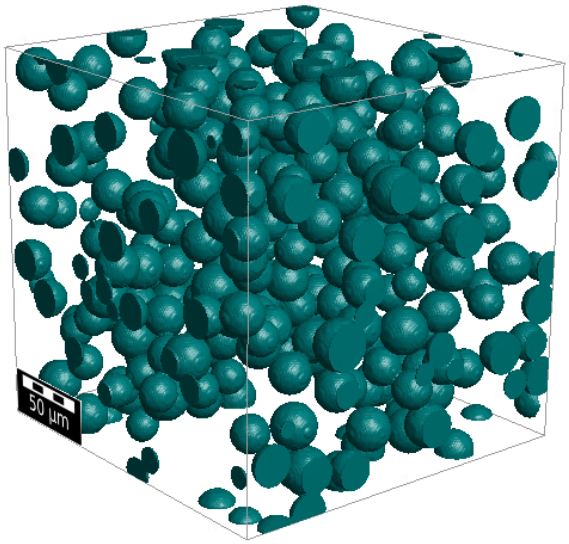

Figure 3.1: RVE of a parameterized PRP represented by the design variables vector $\boldsymbol{d}$ = (15 %, 20 µm, 0.23 W/mK, 30 W/mK)

with direction-dependent macroscopic properties. It should already be pointed out at this point that a consideration of different physical material properties is enabled by introducing several objective functions and the use of constraints. The formulation of such material optimization problems in the standard form of nonlinear structural optimization problems will be presented later in this thesis. In order to select a proper optimization method, the generic material optimization problem (3.1) is analyzed in further detail. The objective function exhibits the following characteristics:

- The evaluation is in general computationally expensive, since an RVE has to be generated for each design specification and several load cases have to be computed.
- Non-convexity is encountered due to the variety of design variables and the influence of stochastic effects.
- No gradient information in closed form is available for the micromechanical (numerical) model.
- Stochastic character due to the randomness of the heterogeneous microstructure.
- Deviations from the specifications in the structure (RVE) generation (even if these deviations are quite small in the considered examples).
- Different optimal, or "near" optimal designs with different robustness may be identified.

Beside the fact, that a single run with a gradient-descent algorithm may locate in a local optimum resulting from the complex behavior of the structural response, the use of gradient-based optimization methods poses further difficulties. The stochastic nature of the RVEs leads to mutual fluctuations in the observed physical fields (e.g., strains and stresses in the mechanical case and temperatures and heat fluxes in the thermal case), which, in turn, leads to noise in the objective function. The use of gradient-based methods carries the risk of being trapped in such a local optimum. Based on these considerations, a global optimization method that attempts to find the global optimum and can handle the problems of noisy behavior, non-convexity, and missing gradient information is chosen. Common global methods such as evolutionary algorithms require far more iterations than gradient-based methods. The application of such global methods on the micromechanical model leads to a tremendous numerical effort, since each function evaluation is associated with the generation of an RVE and the solution of several BVPs. Hence, evolutionary methods cannot be applied directly on microstructural optimization problems due to the enormous computational effort associated with some applications. In order to cope with this computational burden, a surrogate-based optimization method is suggested in the following section.

3.2 Development of a solution strategy

Based on the characterization of the optimization problem in the previous section, a surrogate-based optimization approach [141] is proposed. A flowchart of the optimization framework is shown in Fig. 3.2. The framework comprises the following methodologies:

- Design of Experiments
- Generation of RVEs
- Computational homogenization
- Surrogate modeling
- Sensitivity analysis (optional)
- Global optimization
- Robustness evaluation (optional)

The essential idea is based on the construction of a global approximation of the effective properties of interest $\boldsymbol{\Psi}_{\text{eff}}$ (respectively its components $\Psi_{ij,\text{eff}}$) as a function of the design variables $\boldsymbol{d}$ within the entire material design space. This surrogate model serves as a quick to evaluate representation of the SPR and substitutes the expensive to evaluate computational homogenzation model. As starting point, the parametric optimization

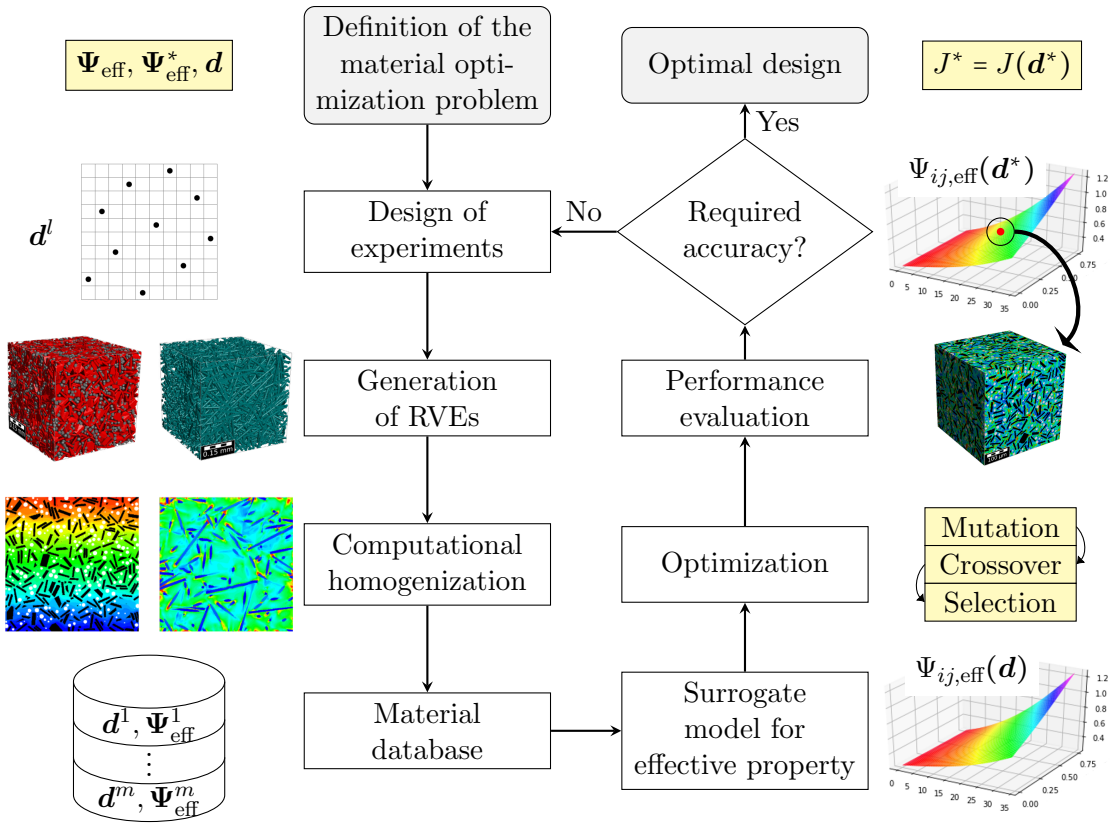

Figure 3.2: Flowchart of the surrogate-based multiscale material design framework

problem (3.1) has to be defined. This includes the specification of the design objectives and constraints as well as the design variables with the feasible set. In the first step, a DoE scheme is used for the exploration of the material design space. For each of the experimental designs $\boldsymbol{d}^{l}$ $(l = 1, ..., m)$, a corresponding RVE is generated. Based on this microstructural design representation, computational homogenization is performed to evaluate the effective property $\boldsymbol{\Psi}^{l}_{\text{eff}}$. For the complete determination of the effective properties in the form of a tensor quantity, in general a total of three load cases must be simulated for the calculation of the thermal conductivity and six load cases for the calculation of the mechanical properties. So-called periodic BCs are used in these investigations. As a result of these previous steps, a material database $(\boldsymbol{d}^{l}, \boldsymbol{\Psi}^{l}_{\text{eff}})$ is provided that depicts the effective material behavior for a discrete set of m microstructural configurations. In order to obtain a model for arbitrary design variables, the third step employs surrogate modeling techniques to construct an approximation of the effective property of interest within the entire material design space $\Psi_{ij,\text{eff}} = \Psi_{ij,\text{eff}}(\boldsymbol{d})$. To identify

a microstrucural design with desired properties, a global optimization technique is employed on the surrogate representation of the parametric material optimization problem. Compared to the application of the simulation model, the evaluation of the objective function can be performed very fast in this way, i.e., the computational burden becomes manageable. Therefore, sensitivity analysis and robustness evaluation methods can be applied to gain further information from the design objectives. This enables a deeper understanding of the property under consideration as a function of the design variables and can support the designer in the selection of materials. Another main advantage of the approach is that once the metamodel is created, it is possible to specify different target values as well as to identify various microstructures for a target property without renewed numerical simulations (except for validation). Since the optimization results are obtained from the surrogate representation of (3.1), a validation simulation has to be conducted by evaluating the optimum with the micromechanical model. The methodical background of the individual steps are explained in more detail in the following sections.

3.3 Design of experiments (DoE)

3.3.1 Introduction

The construction of a surrogate model rely on training data, consisting of a set of input samples (model input data) and the values of interest evaluated at these sampling points (model output data or responses). The selection of the locations of these sampling points in the design space is based on so-called **design of experiments (DoE)** schemes. In general, the objective is to gain as much information as possible with as few as possible sampling points (i.e., computational effort). While the theory of DoE originally emerged in the context of planning physical experiments, appropriate design techniques used in connection with computer simulations have been developed.

An **experimental design** can be described by a set of m experiments, each defined by n input (design) variables d_i $(i = 1, ..., n)$, called factors. In the context of this work, the factors comprise design variables of the geometrical microstrucure and physical material properties as introduced in Section 3.1.1. For each experiment (sampling point) $\boldsymbol{d}^l$ $(l = 1, ..., m)$ to be evaluated by the computer code, the factors are set to specified values, called levels. As denoted in the DoE literature, an experimental design can be expressed as an $(m \times n)$ matrix $\boldsymbol{D}$, where the rows of $\boldsymbol{D}$ represent the sampling points and the columns refer to the corresponding factor settings.

Beside the use for the construction of surrogates, DoE is also used for other purposes such as characterization, sensitivity analysis, screening, or uncertainty quantification. In the following, a brief overview of different DoE schemes with a focus on surrogate modeling is provided.

3.3.2 Classical design methods

DoE schemes were originally developed to conduct physical experiments. Pioneering work was carried out in the 1960s by Ronald Fisher [46] in the field of agriculture. Physical experiments contain stochastic effects encounting random variations. For that purpose, schemes incorporating statistical elements such as randomization, blocking, and replication have been developed to cancel out such random errors. For example, to consider random variations, the samples are selected on the boundary of the design space and replicates are taken. To have an comprehensive overview of such schemes, a short introduction to some of the most popular schemes is presented in the following.

Factorial and fractional factorial designs

Factorial designs [12] are the most basic experimental schemes and are characterized by the fact that the n factors are varied on a specified number of l levels at a regular grid. In a full factorial design, all factor-level combinations are considered, so the design consists of a total number of l^n sampling points. Besides the creation of a global approximation, these design are often used for screening experiments to detect the influence of different design variables and to test if negligible variables occur. Often, 2^n and 3^n with 2 and 3 levels respectively are used. While for 3 levels, a regression model including main effects, interactions, and quadratic effects can be constructed, for 2 levels only main effects and interactions can be taken into account. Their main drawback is the exponentially increasing number of sampling points with the number of factors, making them prohibitively for high-dimensional design spaces. For example, a full factorial design with 5 factors evaluated on 3 levels leads to a number of $3^5 = 243$ experiments to be evaluated. To circumvent this problem, fractional factorial designs were developed. As the name suggests, such designs consists only of a fraction (a subset) of the full factorial design. These designs consist of l^{n-p} experiments, where p denotes the reduction of levels compared to full factorial designs. However, depending on the number of levels (the selection of p), this has the effect that some main effects and interactions may be aliased. This means that an independent estimation from each other is not possible because the corresponding term is missing in the regression model. Both full and fractional factorial designs are illustrated in Fig. 3.3 with 3 (left) and 3-1 (middle) factors on 2 levels.

Central composite designs

For the construction of a linear approximation, $(n+1)$ sampling points and for a quadratic approximation $(n+1)(n+2)/2$ are required. To fit a quadratic approximation, a 3^n or 3^{n-p} design could be used, but often this implies too many sampling points. A commonly used design for fitting second-order polynomials with a limited number of sampling points are the so-called central composite designs (CCD). This is illustrated in

Fig. 3.3 (right). CCD designs requires a number of $2^n + 2n + 1$ sampling points. The 2^n samples are the same as in the full factorial design with two levels. Furthermore, one center point (marked in blue) and $2n$ star points (marked in red) are selected. The star points are placed with distance $\pm\alpha$ from the origin. Depending on the selection of α, there are obtained different variants of CCD. For example, $\alpha = 1$ results in a face-centerd CCD. Other classical design schemes for fitting response surface models include Plackett-Burman designs, Box-Behnken designs, or Koshal designs. A comprehensive overview can be found, for instance, in [116] or [158].

These classical schemes are mostly used for screening purposes and the construction of low-order polynomial response surface models. They are designed more for the identification of trends rather than fitting complex metamodels. For a detailed overview of classic DoE methods, the reader is referred to [116]. Since the structural responses considered in this paper could be arbitrarily complex, the following section presents sampling methods that can be used to approximate more complex structural responses.

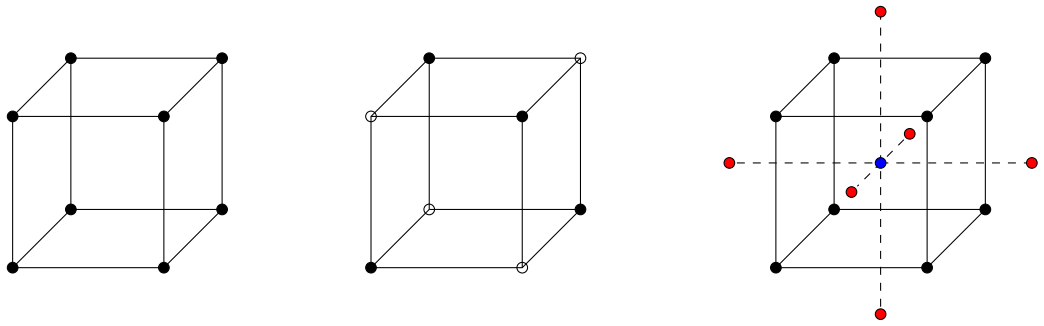

Figure 3.3: Illustration of full factorial (left), fractional factorial (middle), and central composite designs (right)

3.3.3 Design methods for computer experiments

In contrast to physical experiments, computer models are deterministic, which means that a specific input yields always the same response. Noise resulting for example from statistical influence is already included in the problem formulation and the error involved with computer simulation is mostly systemic rather than random. Sacks et al. [152] explained that the elements used in the classical schemes becomes irrelevenat if deterministic simulations are considered. Following that, **space-filling designs** have been developed, which try do spread the samples equally distributed over the entire design space. Since the system responses considered in this work may represent a complex interrelationship between many factors, in that way, all regions of the design space are treated equally. In comparison to classical sampling methods, space-filling designs

are in the most cases not restricted by the use of a certain metamodel type. A goal of setting this points could be for example to minimize the integrated mean squared error (IMSE) over the entire design space, which results in IMSE-optimal designs. Some commonly employed space-filling designs comprise Monte-Carlo sampling, orthogonal arrays, uniform designs, and latin hypercube sampling. A further class can be described by so-called optimality criteria optimal designs. These designs try to fulfill for example a distance criterion. An overview of different approaches can be found in [152]. Because of their importance in the context of this work, latin hypercube (LH) designs are described in more detail in the following.

Latin hypercube sampling (LHS)

LHS was introduced in 1979 by McKay et al. [110] and belongs to the class of statistical sampling methods. It is one of the most popular DoE method used in connection with computationally intensive applications. LHS has the main advantage that it can be initialized with an arbitrary number of samples and does not scale with the dimension of the design space. This is especially relevant for high-dimensional problems, since the computational effort can be reduced to a reasonable level compared to classical (e.g., factorial) designs and also some other modern DoE schemes. The creation of the sample points in LHS can be described as follows. In a first step, the number of experiments (sample size) m has to be defined. The domain for each factor is normalized to the interval [0,1]. This makes large differences between feasible variable spaces for different factors comparable. These intervalls are segmented into m equal-sized strata (size $1/m$), so that the entire design space is subdivided into m^n cells. For the selection of the first sampling point, one cell is chosen randomly. In most cases, the sample is centered inside that cell, but in general the position of the sample in the cell can be chosen to follow a given probability densitiy function. For the selection of the second sampling point, all rows and columns containing the former sample are not allowed to be selected. This will be repeated, until all m sample points are placed inside the hypercube. The restriction that only a single sampling point is permitted in each row and column leads to an equal distribution of the samples in the factor spaces and the advantageous projection properties (by projection in 1D, each strata is filled with a single sampling point). Another advantage of that scheme is, if negligible variables occur, the drawback of replicated points gaining no further information as this would be in other space-filling designs will be avoided. According to Koehler and Owen [92], the LH matrix can be formally constructed as

$$D_{ij} = \frac{\pi_j(i) - U_{ij}}{m} \tag{3.2}$$

with $1 \leq i \leq m$ and $1 \leq j \leq n$. In (3.2), $\pi_j(i)$ are independent random perturbations of the integer sequence $1, ..., m$ and U_{ij} is a uniform random value in the intervall $[0, 1]$. A

simple and commonly used variant of LH sampling is the lattice sampling with $U_{ij} = 0.5$, which means that the samples are centered in the strata. As explained in Section 3.3.1, LH sampling leads to a design matrix $\boldsymbol{D}$ with levels as rows and the associated factor settings in the columns. Following the construction rules, it is clear that there is no unique distribution of the samples. In fact, a LH design can have poor space-filling properties. This can be illustrated by considering a two-dimensional LH design in which each cell diagonal is sampled, so the resulting sampling scheme has poor space-filling properties (see Fig. 3.4, left). To overcome this disadvantages, several improvements were developed. These try to optimize the sample distribution by optimizing a certain distance criterion. For example, the so-called maximin approach of Morris and Mitchell [120] tries to optimize the distance of the sampling points. Such a design is called a maximin LH design. Another approach is to minimize the correlation between the samples. The employed LH design is such an improved version of LHS. It is based on an optimization of the sample distribution using the enhanced stochastic evolutionary algorithm [80] and is implemented in the surrogate modeling toolbox (Python library SMT) [22]. In Fig. 3.4 (right), a LH design for two factors ($n = 2$) and $m = 10$ with improved space-filling properties is illustrated.

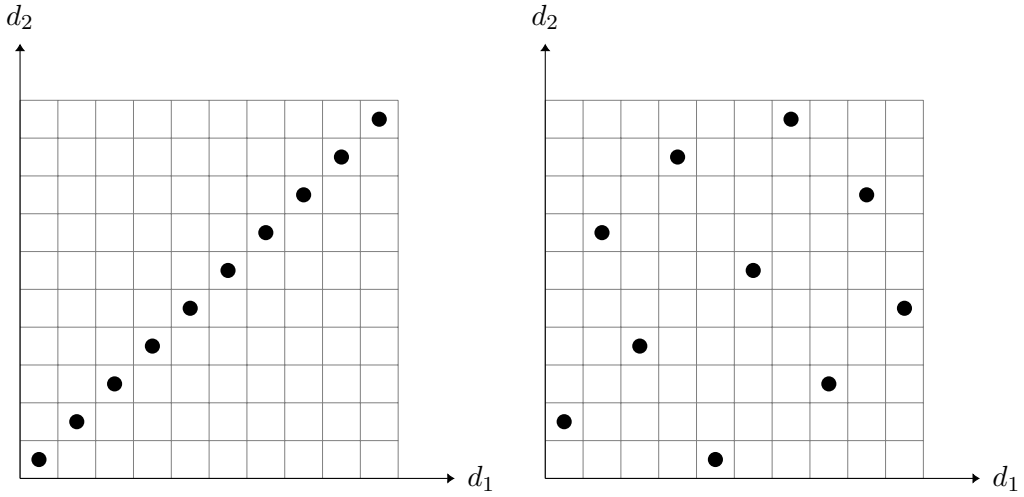

Figure 3.4: Two-dimensional LH design for $m = 10$ with poor (left) and improved space-filling properties (right)

3.4 Generation of representative volume elements (RVEs)

The determination of a specific effective property $\boldsymbol{\Psi}_{\text{eff}} = \boldsymbol{\Psi}_{\text{eff}}(\boldsymbol{d})$ of a microstructural design represented by the design vector $\boldsymbol{d}$ requires the creation of an RVE. For the

generation of three-dimensional RVEs of particle reinforced and short fiber reinforced polymers, the GrainGeo [64] and FiberGeo [65] modules integrated in the voxel-based software GeoDict [14] (`https://www.math2market.com/index.html`) are employed. Beside the generation of particle reinforced structures, GrainGeo allows the generation of granular and sintered materials, which are relevant in various technical applications. In these modules, all parameters required for the specification of the geometrical microstructure can be defined. This includes the specification of the geometrical shape and the size distribution of the particles, the filler volume fractions (respectively the weight fractions, the number of particles, or the density of the composite), as well as the orientation of the fillers. Moreover, the distribution of the particles within the polymer matrix can be defined in different ways. The implemented structure generation algorithms randomly places the particles inside the matrix and then gradually removes the overlap through several operations. The statistical distribution of the particles within the matrix can be controlled by a random number (called random seed), which allows the generation of different random RVEs. As RVE parameters, the edge length l and the resolution (expressed by the voxel length h) of the structure must be specified. In the work at hand, only cubical volume elements are considered. The particles are not allowed to touch each other, which can be specified by the definition of an isolation distance. For the generation of RVEs of SFRPs, there exists the so-called sequential addition and migration method [159]. This algorithm allows the precise generation of structures with large fiber aspect ratios and large volume fractions. A comprehensive review of methods for generating three-dimensional RVEs can be found in [13].

3.5 Micromechanics and homogenization

In this section, first, a concise summary of basic concepts and analytical methods of micromechanics is provided. Secondly, the formulation of BVPs on the microscale in the context of numerical homogenization is presented.

3.5.1 Heterogeneous materials - Basics and length scales

Most materials that are observed on a finer length scale exhibit a more or less pronounced heterogeneity. These can be, for example, micropores, cracks, or grain boundaries in alloys. For the materials considered in this work, this heterogeneity is due to different reinforcements such as fibers or other filler particles. The subject of micromechanics is the investigation of the impact of these heterogeneities on the macroscopic material behavior. Since these heterogeneities occur at different length scales, an essential task of these theories is to link these scales in a suitable way. For that purpose, a coupling between a finer scale (the microscale) and the macroscale is performed by assigning to each macroscopic point the corresponding microstructure. Within this concept, a micro-macro transition in terms of appropriate averaging technique is carried out, reffered to

as homogenization. The properties of a homogeneous reference material determined in this way are called effective or macroscopic material properties and describe the macroscopic constitutive behavior. For the determination of effective properties, a sample of the heterogeneous material is considered, which must be representative to adequately delineate the underlying microstructure. In the following, the prerequisites for the determination of such a representative volume element suggested by Hill [67] is introduced. A condition for the size of the RVE is that the characteristic length l of the RVE must be much smaller than the characteristic length L of the macroscopic sample. That means, if

$$l \ll L \tag{3.3}$$

seperation of scales holds and the RVE can be regarded as a material point on the macroscopic level. For the determination of an RVE, the effective properties must be independent of the shape and size as well as the statistical distribution of the heterogeneities. Thus, another condition is that the RVE under consideration must contain a sufficiently large number of heterogeneities. This can be expressed as

$$d_h \ll l \tag{3.4}$$

with the characteristic length d_h of the heterogeneities. These characteristic length scales are illustrated in Fig. 3.5. If these conditions are fulfilled, the volume element is denoted as representative volume element. In the mathematical theory of homogenization [11], the ratio l/L is introduced. For $l/L \to 0$ this results in homogenized properties. The determination of a sufficient size of the RVE is described in more detail in Section 3.5.7.

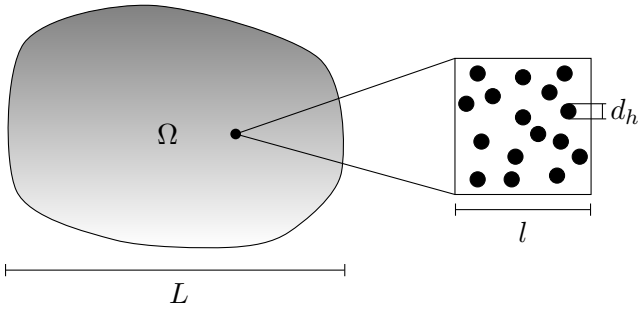

Figure 3.5: Considered length scales

In recent decades, there have been tremendous advances in the science as well as the technological development of heterogeneous materials. The multiscale methods developed in this context can essentially be divided into two categories: (Semi-)analytical, hybrid, and computational methods. Some of them will be briefly reviewed in the following.

3.5.2 Bounds

An indication of the lower and upper bounds of the effective properties is provided by the averaging rules proposed by Voigt [186] and Reuss [146]. Assuming a linear material behavior of the constituents, these are obtained by averaging the properties of the individual constituents, weighted according to their volume fractions. If a constant macroscopic strain $\langle \boldsymbol{\epsilon} \rangle$ is supposed in the individual constituents of the material, following Voigt [186], an upper bound of the overall stiffness tensor is given as

$$\boldsymbol{C}_{\text{Voigt}} = \sum_{p=1}^{P} V_{f_p} \boldsymbol{C}_p. \tag{3.5}$$

This assumption can be regarded as a simplified stiffness model of a composite where the constituents are arranged in parallel, as illustrated in Fig. 3.6 (left). Respectively, following Reuss [146], a lower bound of the overall stiffness tensor is given as

$$\boldsymbol{C}_{\text{Reuss}}^{-1} = \sum_{p=1}^{P} V_{f_p} \boldsymbol{C}_p^{-1}, \tag{3.6}$$

subjecting the constitutents to a uniform macroscopic stress $\langle \boldsymbol{\sigma} \rangle$, which corresponds to a simplified stiffness model where constituents are arranged in series, see Fig. 3.6 (right). In summary, the overall stiffness tensor $\boldsymbol{C}_{\text{eff}}$ of a composite ranges between these two bounds, i.e,

$$\boldsymbol{C}_{\text{Reuss}} \leq \boldsymbol{C}_{\text{eff}} \leq \boldsymbol{C}_{\text{Voigt}}. \tag{3.7}$$

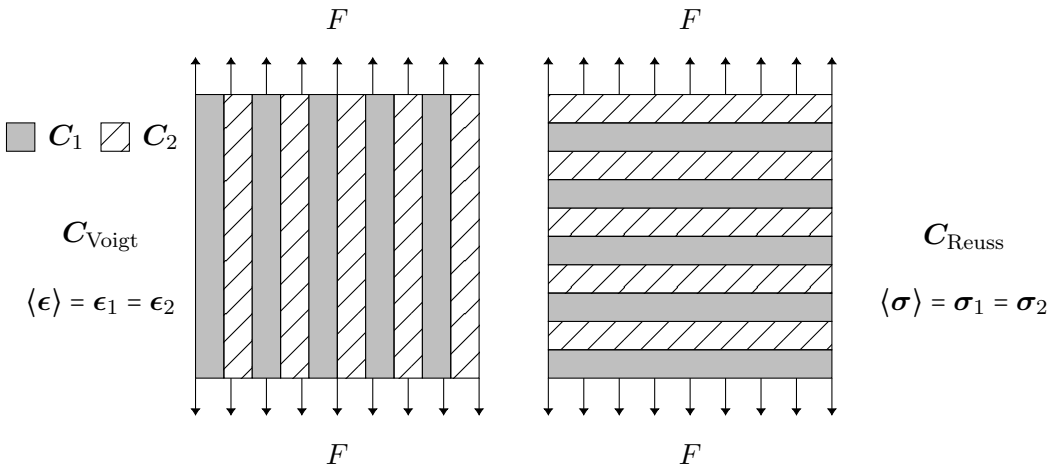

Figure 3.6: Simplified 2D material model with $P = 2$ for extraction of lower (right) and upper (left) bounds

In (3.5) and (3.6), V_{f_p} ($\sum_{p=1}^{P} V_{f_p} = 1$) denotes the volume fraction of phase p with stiffness tensor $\boldsymbol{C}_p$ of a material consisting of P phases. Theses relations apply analogously to all other linear material properties. Hence, substituting $\boldsymbol{C}_p$ in (3.5) and (3.6) by the thermal conductivity tensors $\boldsymbol{k}_p$, the so-called Wiener bounds are obtained, which represent the upper and lower bounds of the thermal conductivity. The derivation of the upper Wiener bound is based on the assumption of a constant macroscopic temperature gradient and the heat flux results as the weighted sum of the heat fluxes through all phases. Respectively, the derivation of the lower Wiener bound is based on the assumption of a constant macroscopic heat flux vector and the temperature gradient results as the weighted sum of temperature gradients across all phases. It is obvious that these bounds do not take into account the morphology of the microstructure. Moreover, especially in the case of large contrasts in the properties (e.g., stiffness, conductivity) of the constituents, the range between the upper and the lower bound can be quite large. For example, the upper Wiener bound [190] implies a fully percolating network. Extensions of these bounds for isotropic materials in the form of variational concepts are given by the Hashin-Shtrikman bounds [60], which are known to be more rigorous than the Voigt-Reuss bounds. Hereby a polarization field is introduced and a BVP is formulated using that field relative to a reference material.

3.5.3 Analytical homogenization methods

The most simple approaches for the determination of effective properties is based on the so-called rule of mixture. This only considers the properties of the individual phases and their phase fractions by volume averaging of the phase properties weighted by their volume percentages (see (3.5) and (3.6)) and yields a very coarse estimation of the effective properties. A common class of analytical methods is represented by the mean-field approaches, which relate back to the inclusions theorie of Eshelby [43] suggested before the advent of computers. These mean-field approximations are based on the analytical solution of a boundary value problem in which an infinitely extended matrix with a single elliptical inclusion under constant load is considered. The geometry of this inclusion is taken into account by specification of microstructural tensors [54]. Extensions have been developed to account for the interaction of multiple inclusions through the interaction of their microscopic solution fields. The self-consistent scheme [97], [66], [26] considers a single inclusion embedded in a material with the effective (unknown) properties and achieves quite good approximations when the geometry exhibits some regularity. However, it is not suitable for more complex microstructures with large volume fractions and large contrast in the individual phases. Another approach considering the interaction of different particles by taking the effective field operating on each inclusion in terms of the field average across the matrix is provided by the approach of Mori and Tanaka [119]. The Mori-Tanaka approach coincides with the Hashin-Shtrikman bounds [54]. Extension of this approach are given in [17]. These methods are only sufficiently

accurate for simple (basically elliptical) inclusions, low contrasts in the phase properties and low volume fractions. For example, if a void volume fraction of 50% is considered, the self-consistent approach yields a bulk and shear moduli tending to zero. Analytical approximation methods generally cannot capture the strongly fluctuating microfields of complex microstrucutres such as those considered in this work. A comprehensive introduction into micromechanics can be found, for example, in the textbook of Aboudi [1] or Torquato [179]. The utilization of the mentioned methods for the determination of effective conductivity properties can be found in [82].

3.5.4 Computational homogenization

In this section, the computation of the effective thermal conductivity and the linear elastic properties of composite materials within the concept of first-order computational homogenization is presented. First, the basic concepts of coupling microscopic and macroscopic quantities in terms of averaging relations are introduced. Then, in the following subsections, focus is put onto the associated BVPs formulated at the RVE level and the derivation of appropriate BCs from macroscopic quantities. Finally it will be shown, how effective properties can be extracted from the solution of the microscopic solution fields.

First-order computational homogenization were first adressed in [145] in the context of mechanical properties and are used in some multiscale methods. As stated in [94], the principles of first-order homogenization techniques can be summarized in four steps:

- Definition of an RVE including the specification of the constitutive behavior of all constituents
- Selection of suitable BCs derived from macroscopic quantities and application on the boundary of the RVE (macro-micro transition)
- Determination of macroscopic properties from the solution of the micromechanic BVP (micro-macro transition)
- Extraction of the effective material properties from the relation between prescribed microscopic input and computed output variables

These principle steps are illustrated in Fig. 3.7 for heat conduction problems. On both scales, the continuum mechanic framework introduced in Chapter 2 is valid. Because linear properties and small deformations are considered in that work, a precomputation of the effective properties needed for component simulations can be performed and no microscopic problem has to be solved in parallel. However, the scheme is not restricted to linear material behavior, thus arbitrary nonlinear material behavior and finite deformations can be considered within a nested solution scheme, see [45], [94] or [172] for

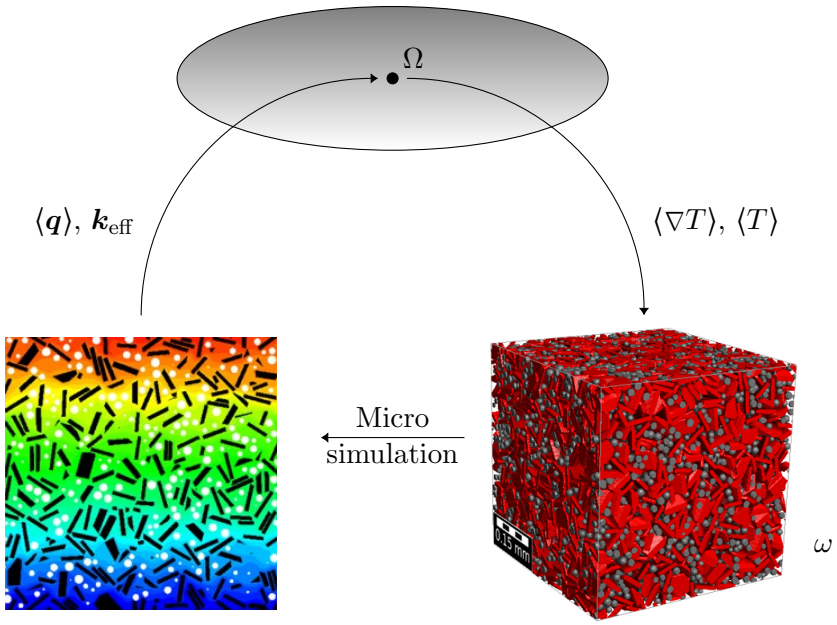

Figure 3.7: First-order computational homogenization for heat conduction

further details of handling such problems. In the first step, an RVE as defined in Section 3.5.1 describing the geometrical and physical properties of the underlying microstructure has to be identified. If a spatially varying microstructure has to be considered, each macroscopic point is assigned a corresponding RVE. The selection of the size of the RVE will be discussed in more detail in Section 3.5.7. In the remainder of this section, it is assumed that a RVE that captures the physical behavior of the underlying microstructure has been identified. To distinguish between micro- and macroscale, the following notations are introduced. A physical point of the macrostructure $\boldsymbol{X} \in \Omega \subset \mathbb{R}^3$ is associated with an RVE with the domain $\omega = (0, l)^3 \subset \mathbb{R}^3$ and the boundary $\partial\omega$. A macroscopic quantity at the position $\boldsymbol{X}$ is denoted as $\langle \boldsymbol{a} \rangle$ and the microscopic one at position $\boldsymbol{x} \in \omega$ is designated with plain letters $\boldsymbol{a}$. In the second step, a BVP is formulated on the microscale by specifying a macroscopic quantity. This could be a strain tensor in the mechanical case or a temperature gradient in the thermal case. The derivation of suitable BCs from macroscopic quantities and the formulation of a BVP on the microscale is treated in more detail in the following subsections. In the third step, the macroscopic properties are obtained from the computed microscopic solution fields by a volume-averaging process. The volume-averaging procedure of an arbitrary microscopic quantity $\boldsymbol{a}$, denoted with angle brackets $\langle \boldsymbol{a} \rangle$, is defined as

$$\langle \boldsymbol{a} \rangle = \frac{1}{|\omega|} \int_{\omega} \boldsymbol{a}(\boldsymbol{x}) \, \mathrm{d}\omega. \tag{3.8}$$

If seperation of scales holds (see Section 3.5.1), it is postulated that a macroscopic quantity $\langle \boldsymbol{a} \rangle$ on a material point at the macroscale can be described by the volume average of the quantity $\boldsymbol{a}$ over the RVE domain. This averaging process describes the scale-transition relations. Finally, the effective material properties can be derived from an energy-based criterion, which demands the equivalence of thermal, respectively mechanical energy on micro- and macroscale.

To compute the associated microscopic field values, so-called localization problems to be solved within the RVE domain ω are introduced in the following. The derivation of appropriate BCs in terms of macroscopic quantities is described. The computation of the effective thermal conductivity and the linear elastic stiffness tensor is outlined.

3.5.5 Effective thermal conductivity properties

For the determination of effective thermal material properties, the local quantities to be computed are the heat flux vector $\boldsymbol{q}(\boldsymbol{x})$ and the temperature gradient $\nabla T(\boldsymbol{x})$. In each point of the microscopic (RVE) domain ω, the thermal equilibrium equation (see Section 2.2)

$$\operatorname{div} \boldsymbol{q}(\boldsymbol{x}) = 0 \tag{3.9}$$

has to be fulfilled. The heat flux $\boldsymbol{q}(\boldsymbol{x})$ and the temperature gradient $\nabla T(\boldsymbol{x})$ are linked via Fourier's law 2.22. The solution of (3.9) requires the selection of appropriate BCs in terms of macroscopic quantities. The requirement of equivalance of thermal energy on both micro- and macroscale can be expressed as

$$\langle \boldsymbol{q} \cdot \nabla T \rangle = \frac{1}{|\omega|} \int_{\omega} \boldsymbol{q} \cdot \nabla T \, \mathrm{d}\omega = \langle \boldsymbol{q} \rangle \cdot \langle \nabla T \rangle. \tag{3.10}$$

It can be shown that the energy criterion (3.10) is valid (not exclusively) for the following BCs:

- Periodic BCs expressed as

$$T(\boldsymbol{x}) = \langle \nabla T \rangle \cdot \boldsymbol{x} + \tilde{T}(\boldsymbol{x}) \quad \boldsymbol{x} \in \partial\omega \tag{3.11}$$

  with a periodic temperature fluctuation $\tilde{T}(\boldsymbol{x})$ in ω.

- Dirichlet BCs in terms of a macroscopic temperature gradient as

$$T(\boldsymbol{x}) = \langle \nabla T \rangle \cdot \boldsymbol{x} \quad \boldsymbol{x} \in \partial\omega. \tag{3.12}$$

- Neumann BCs in terms of a macroscopic heat flux vector as

$$\boldsymbol{q}(\boldsymbol{x}) = \langle \boldsymbol{q} \rangle \cdot \boldsymbol{n}(\boldsymbol{x}) \quad \boldsymbol{x} \in \partial\omega \tag{3.13}$$

  where $\boldsymbol{n}$ denotes the unit outward normal on $\partial\omega$.

In this work, only periodic BCs (3.11) are considered because it is known that they lead to a more accurate estimation and faster convergence (with respect to the size of the RVE) [84] of the effective conductivity. The local temperature gradient field may be expressed in terms of the transferred macroscopic temperature gradient and an fluctuating part due to the heterogeneities of the microstructure as

$$\nabla T(\boldsymbol{x}) = \langle \nabla T \rangle + \nabla \tilde{T}(\boldsymbol{x}). \tag{3.14}$$

Note that this splitting operation can be used analogously for all other microscopic field values. The periodic BVP for the homogenization of the thermal properties in the RVE domain ω can be summarized as follows: For a given macroscopic temperature gradient $\langle \nabla T \rangle$, find the temperature fluctuations $\tilde{T}$ such that

$$\begin{aligned}
&\operatorname{div} \boldsymbol{q}(\boldsymbol{x}) = 0 && \boldsymbol{x} \in \omega \\
&\boldsymbol{q}(\boldsymbol{x}) = -\boldsymbol{k}(\boldsymbol{x}) \cdot \nabla T(\boldsymbol{x}) && \boldsymbol{x} \in \omega \\
&\nabla T(\boldsymbol{x}) = \langle \nabla T \rangle + \nabla \tilde{T}(\boldsymbol{x}) && \boldsymbol{x} \in \omega \\
&\tilde{T}(\boldsymbol{x}) \quad \# && \boldsymbol{x} \in \partial\omega \\
&\boldsymbol{q}(\boldsymbol{x}) \cdot \boldsymbol{n}(\boldsymbol{x}) \quad -\# && \boldsymbol{x} \in \partial\omega.
\end{aligned} \tag{3.15}$$

The notation # means periodicity, so the fluctuation on opposite edges ($\partial\omega^+$ and $\partial\omega^-$) of the RVE are equal. Respectively, $-\#$ means antiperiodicity, i.e., the heat flux vector on opposite edges shows into opposite directions. The thermal conductivity tensors $\boldsymbol{k}$ of the individual phases are assumed to be temperature independent, which is a valid assumption for the considered materials and the considered temperature ranges. Moreover, perfect bonding between the filler particles and the matrix is considered. However, it is also possible to consider contact resistance between the individual phases. The macroscopic temperature gradient can be chosen arbitrarily for a constant temperature. Finally, the effective thermal conductivity (ETC) tensor $\boldsymbol{k}_{\text{eff}}$ is derived from the energy equivalence criterion. If a single component of the macroscopic temperature gradient (e.g., in x_1-direction) is prescribed, the macroscopic constitutive law can be expressed as

$$\begin{pmatrix} \langle q_1 \rangle \\ \langle q_2 \rangle \\ \langle q_3 \rangle \end{pmatrix} = \begin{pmatrix} k_{11,\text{eff}} & k_{12,\text{eff}} & k_{13,\text{eff}} \\ k_{12,\text{eff}} & k_{22,\text{eff}} & k_{23,\text{eff}} \\ k_{13,\text{eff}} & k_{23,\text{eff}} & k_{33,\text{eff}} \end{pmatrix} \cdot \begin{pmatrix} \langle \nabla T_1 \rangle \\ 0 \\ 0 \end{pmatrix}. \tag{3.16}$$

By specification of three perpendicular components of the heat flux vector (and setting the remaining to zero), the full ETC tensor $\boldsymbol{k}_{\text{eff}}$ can be computed (see Fig. 3.7 for illustration). This computations are performed with the ConductoDict module [15] of GeoDict [14] employing the EJ-HEAT solver [189]. If an isotropic orientation and uniform distribution of the fillers is considered, $\boldsymbol{k}_{\text{eff}}$ reduces to a scalar value, i.e., $\boldsymbol{k}_{\text{eff}} = k_{\text{eff}}\boldsymbol{I}$ and it is sufficient to compute a single load case.

3.5.6 Effective linear elastic properties

For the extraction of the effective linear elastic material properties, the local quantities to be computed are the displacements $\boldsymbol{u}(\boldsymbol{x})$, strains $\boldsymbol{\epsilon}(\boldsymbol{x})$, and stresses $\boldsymbol{\sigma}(\boldsymbol{x})$. In each point of the microscopic (RVE) domain ω, the static balance equation (see Section 2.1.2 by neglecting volume forces $\boldsymbol{f}$)

$$\operatorname{div} \boldsymbol{\sigma}(\boldsymbol{x}) = \mathbf{0} \tag{3.17}$$

has to be fulfilled. The stresses $\boldsymbol{\sigma}(\boldsymbol{x})$ and strains $\boldsymbol{\epsilon}(\boldsymbol{x})$ are related via Hooke's law 2.14. Perfect bonding between the filler particles and the matrix is considered. The requirement of equivalance of mechanical energy on both micro- and macroscale can be expressed as

$$\langle \boldsymbol{\sigma} : \boldsymbol{\epsilon} \rangle = \frac{1}{|\omega|} \int_{\omega} \boldsymbol{\sigma} : \boldsymbol{\epsilon} \, \mathrm{d}\omega = \langle \boldsymbol{\sigma} \rangle : \langle \boldsymbol{\epsilon} \rangle. \tag{3.18}$$

It can be shown that energy is preserved (condition (3.18) is valid) over both scales (not exclusively) for the following BCs:

- Periodic BCs expressed as

$$\boldsymbol{u}(\boldsymbol{x}) = \langle \boldsymbol{\epsilon} \rangle \cdot \boldsymbol{x} + \tilde{\boldsymbol{u}}(\boldsymbol{x}) \quad \boldsymbol{x} \in \partial\omega \tag{3.19}$$

  whith a periodic displacement fluctuation $\tilde{u}(\boldsymbol{x})$ in ω.

- Dirichlet BCs in terms of a macroscopic strain as

$$\boldsymbol{u}(\boldsymbol{x}) = \langle \boldsymbol{\epsilon} \rangle \cdot \boldsymbol{x} \quad \boldsymbol{x} \in \partial\omega. \tag{3.20}$$

- Neumann BCs in terms of a macroscopic stress as

$$\boldsymbol{t}(\boldsymbol{x}) = \langle \boldsymbol{\sigma} \rangle \cdot \boldsymbol{n}(\boldsymbol{x}) \quad \boldsymbol{x} \in \partial\omega. \tag{3.21}$$

Following the same arguments as in the thermal case, only periodic BCs are considered in this work. The displacement fluctuations on opposite edges ($\partial\omega^+$ and $\partial\omega^-$) of the RVE are equal and the traction vectors show in opposite directions. This is illustrated in Fig. 3.8. By decomposing the microscopic strain field into a constant macroscopic strain (which is transferred according to (3.19)) and a fluctuating part, the following kinematic relation

$$\boldsymbol{\epsilon}(\boldsymbol{x}) = \langle \boldsymbol{\epsilon} \rangle + \boldsymbol{\epsilon}(\tilde{\boldsymbol{u}}) \tag{3.22}$$

is obtained. The strain fluctuations $\boldsymbol{\epsilon}(\tilde{\boldsymbol{u}})$ result from the heterogeneity of the microstructure and are given as

$$\boldsymbol{\epsilon}(\tilde{\boldsymbol{u}}) = \frac{1}{2}(\nabla \tilde{\boldsymbol{u}} + \nabla^T \tilde{\boldsymbol{u}}). \tag{3.23}$$

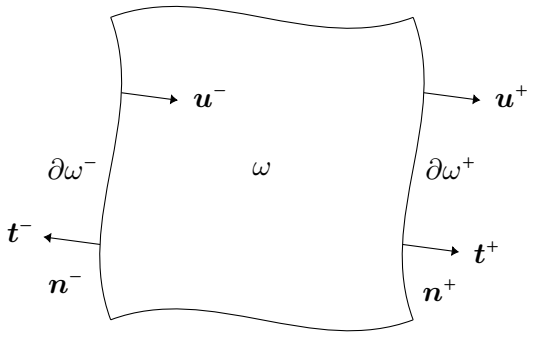

Figure 3.8: Illustration of periodic boundary conditions

The periodic BVP for the computation of the effective linear elastic properties in the RVE domain ω can be summarized as follows: For a given macroscopic strain $\langle\boldsymbol{\epsilon}\rangle$, find the displacement fluctuation field $\tilde{\boldsymbol{u}}$ such that

$$\begin{aligned}
&\operatorname{div}\boldsymbol{\sigma}(\boldsymbol{x}) = 0 && \boldsymbol{x}\in\omega\\
&\boldsymbol{\sigma}(\boldsymbol{x}) = \boldsymbol{C}(\boldsymbol{x}) : \boldsymbol{\epsilon}(\boldsymbol{x}) && \boldsymbol{x}\in\omega\\
&\boldsymbol{\epsilon}(\boldsymbol{x}) = \langle\boldsymbol{\epsilon}\rangle + \frac{1}{2}(\nabla\tilde{\boldsymbol{u}}(\boldsymbol{x}) + \nabla^T\tilde{\boldsymbol{u}}(\boldsymbol{x})) && \boldsymbol{x}\in\omega\\
&\tilde{\boldsymbol{u}}(\boldsymbol{x}) \quad\quad \# && \boldsymbol{x}\in\partial\omega\\
&\boldsymbol{\sigma}(\boldsymbol{x})\cdot\boldsymbol{n}(\boldsymbol{x}) \quad -\# && \boldsymbol{x}\in\partial\omega.
\end{aligned} \tag{3.24}$$

Finally, the full linear elastic stiffness tensor $\boldsymbol{C}_{\text{eff}}$ is derived from the energy equivalence criterion. The macroscopic elastic constants can be computed by the specification of a single component of a macroscopic strain (e.g., in x_1-direction and setting the remaining to zero) as:

$$\begin{pmatrix}\langle\sigma_1\rangle\\ \langle\sigma_2\rangle\\ \langle\sigma_3\rangle\\ \langle\sigma_4\rangle\\ \langle\sigma_5\rangle\\ \langle\sigma_6\rangle\end{pmatrix} = \begin{pmatrix} C_{11,\text{eff}} & C_{12,\text{eff}} & C_{13,\text{eff}} & C_{14,\text{eff}} & C_{15,\text{eff}} & C_{16,\text{eff}}\\ C_{12,\text{eff}} & C_{22,\text{eff}} & C_{23,\text{eff}} & C_{24,\text{eff}} & C_{25,\text{eff}} & C_{26,\text{eff}}\\ C_{13,\text{eff}} & C_{23,\text{eff}} & C_{33,\text{eff}} & C_{34,\text{eff}} & C_{35,\text{eff}} & C_{36,\text{eff}}\\ C_{14,\text{eff}} & C_{24,\text{eff}} & C_{34,\text{eff}} & C_{44,\text{eff}} & C_{45,\text{eff}} & C_{46,\text{eff}}\\ C_{15,\text{eff}} & C_{25,\text{eff}} & C_{35,\text{eff}} & C_{45,\text{eff}} & C_{55,\text{eff}} & C_{56,\text{eff}}\\ C_{16,\text{eff}} & C_{26,\text{eff}} & C_{36,\text{eff}} & C_{46,\text{eff}} & C_{56,\text{eff}} & C_{66,\text{eff}}\end{pmatrix} \cdot \begin{pmatrix}\langle\epsilon_1\rangle\\ 0\\ 0\\ 0\\ 0\\ 0\end{pmatrix}. \tag{3.25}$$

By specification of six perpendicular components of the macroscopic strain (and setting the reamining components to zero), the full linear elastic stiffness tensor can be computed. These computations are performed with an FFT-based solution scheme implemented in the ElastoDict module [148] of GeoDict [14]. If an isotropic orientation and uniform particle distribution is considered, only two load cases (one tension and one shear load) need to be simulated to predict the linear elastic stiffness tensor.

3.5.7 Determination of numerical RVEs

This subsection presents the procedure for determining a sufficient size of the RVE. It is obvious that it is not possible to compute effective properties of RVEs with arbitrarily large size l due to limited computational resources. For this purpose, numerical RVEs [123] are considered, which need to exhibit sufficient accuracy for engineering purposes. As mentioned in the previous section, the convergence of the effective properties with respect to the size of the RVE also depends on the applied BCs. To determine a sufficient size of the RVE, the most common approach is to carry out a convergence study examining an ensemble size criterion and a volume size criterion [123]. A rigorous procedure for the determination of the size of RVEs can be found, e.g., in [84] and applications are given in [112], [177]. To account for the influence of the statistical realization of the microstructure (the distribution of the fillers within the matrix) [132], the ensemble average

$$\langle\!\langle \boldsymbol{\Psi}_{\text{eff}} \rangle\!\rangle_N = \frac{1}{N} \sum_{k=1}^{N} \boldsymbol{\Psi}_{\text{eff},k} \tag{3.26}$$

with the effective property of interest $\boldsymbol{\Psi}_{\text{eff,k}}$ of the kth statistical realization and the number of realizations N is considered. In GeoDict [14], different statistical realizations can be defined by a random number, the so-called random seed. The number of realizations N might be chosen until the effective property saturates within a specified tolerance. As a measure of the influence of these statistical realizations, the standard deviation

$$s_N = \sqrt{\frac{1}{N-1} \sum_{k=1}^{N} (\boldsymbol{\Psi}_{\text{eff},k} - \langle\!\langle \boldsymbol{\Psi}_{\text{eff}} \rangle\!\rangle_N)^2} \leq \epsilon_{ens} \tag{3.27}$$

can be regarded. The value ϵ_{ens} can be chosen according to the individual requirements. In order to determine a sufficient RVE size in form of the edge length l, the following volume size criterion is used:

$$\frac{\| \langle\!\langle \boldsymbol{\Psi}_{\text{eff}} \rangle\!\rangle_{N_{l+1}} - \langle\!\langle \boldsymbol{\Psi}_{\text{eff}} \rangle\!\rangle_{N_l} \|_2}{\| \langle\!\langle \boldsymbol{\Psi}_{\text{eff}} \rangle\!\rangle_{N_l} \|_2} \leq \epsilon_{vol}, \tag{3.28}$$

where the relative change of the ensemble average of the quantity of interest is observed by enlarging l. Again, the choice of ϵ_{vol} is made depending on the desired accuracy. Please note that the larger the RVE, the lower the influence of the statistical realizations, so sometimes criteria accounting for such statistical influences (e.g., (3.27)) are examined to determine a sufficient edge length [84]. In order to determine a sufficient resolution of the structure in form of the voxel length h, a similar approach can be adopted. For this purpose, the effective property is computed for different resolutions, and the relative deviation is observed:

$$\frac{\| \langle\!\langle \boldsymbol{\Psi}_{\text{eff}} \rangle\!\rangle_{N_{h+1}} - \langle\!\langle \boldsymbol{\Psi}_{\text{eff}} \rangle\!\rangle_{N_h} \|_2}{\| \langle\!\langle \boldsymbol{\Psi}_{\text{eff}} \rangle\!\rangle_{N_h} \|_2} \leq \epsilon_{res}. \tag{3.29}$$

In conclusion, the required size depends on the considered microstructural configuration, which means that the specific settings (and ranges) of the design variables must be taken into account in the context of this work.

3.6 Surrogate modeling

As shown in the previous sections, the computation of the effective properties includes the generation of an RVE and the performance of a computationally expensive simulation. In context of optimization, sensitivity analysis, and uncertainty quantification the (expensive) system response has to be evaluated numereous times with different factor settings of the design variables. Even with the strong increment in computer power and the use of parallel processing, a direct use of the numerical model is often too time consuming (ranges from minutes to several hours). To overcome the computational burden, the use of surrogate models is a widely used technique in engineering [141], [168]. A surrogate model can be regarded as a model of a model (e.g., of a simulation model). It serves as a global approximation of this original physical model. Surrogate models are also referred to as response surface model, enumator, or just model. If such a model is available, the analysis of the model output can be performed very fast, as it replaces the computationally intensive simulation model. Surrogate modeling can be considered as supervised machine-learning model. Based on a set of training data, the model can predict the output for arbitrary model inputs.

Based on the observations made from the DoE scheme, an appropriate function type has to be selected. There can be distinguished between approximation and interpolation models and there exist different approaches for both. If the surrogate model type is selected, the model parameters have to be chosen based on training data. In the following, the output of a surrogate model is denoted simply as scalar y and the input is represented by the design variables vector $\boldsymbol{d}$. A metamodel attempts to approximate or interpolate the model output y as a function of $\boldsymbol{d}$, i.e., $y = f(\boldsymbol{d})$.

The benefits of surrogate models can be summarized as follows:

- Providing overall knowledge of the problem in the design domain.
- Reducing the cost of computational analysis by approximating the simulation model.
- Supporting the optimization process.
- Parallel computing possible.

By using a surrogate model for optimization, it is in general not required to have a model which covers the true behavior in every point of the design space with high accuracy.

Only in the vicinity of the optimum, the quality should be sufficient enough. Another case is the use of the surrogate for design space approximation. In the context of this work, such a design space approximation can be relevant, if the model should be used as material model for example as an input for component simulations and for that purpose, the accuracy in the whole design space has to be sufficient enough.

3.6.1 Response surface models (RSM)

The term response surface model (RSM) [125], [23] is mostly denoted to low-order polynomial regression models, although the term is sometimes used as a synonym for metamodels in a more general sense. In an RSM, a regression model of the form

$$y(\boldsymbol{d}) = \hat{y}(\boldsymbol{d}, \boldsymbol{\beta}) + \epsilon, \tag{3.30}$$

with the approximation (response surface) $\hat{y}(\boldsymbol{d}, \boldsymbol{\beta})$ and a normally distributed random error ϵ with mean zero is postulated. The functional relationship between dependent and independent variable is established by regression [117], i.e., fitting the regression model (3.30) to a set of m sampling points $\boldsymbol{d}^l$ and the corresponding responses y_l usually by the method of least squares. If the regression model is linear in $\boldsymbol{\beta}$, it is referred to as a linear regression problem. In general, the regression model is not limited to polynomials and can take various forms. The most simplest approach is given in terms of a first-order polynomial to describe linear relationships. For the frequently used second-order (quadratic) polynomial model, $\hat{y}(\boldsymbol{d}, \boldsymbol{\beta})$ can be expressed in n design variables as

$$\hat{y}(\boldsymbol{d}, \boldsymbol{\beta}) = \beta_0 + \sum_{i=1}^{n} \beta_i d_i + \sum_{i=1}^{n} \sum_{j \geq 1}^{n} \beta_{ij} d_i d_j, \tag{3.31}$$

where here only second-order interactions (effects involving two independent variables) are considered. This results in a total number of $p = (n+1)(n+2)/2$ scalar regression coefficients $\boldsymbol{\beta}$ to be determined. In general, also higher-order effects can be included. If the response is evaluated at m sampling points $\boldsymbol{d}^l$, the vector of the m responses $\hat{\boldsymbol{y}}$ can be expressed in matrix form as

$$\hat{\boldsymbol{y}} = \boldsymbol{D}\boldsymbol{\beta}, \tag{3.32}$$

with the $m \times p$ design matrix $\boldsymbol{D}$ and the vector of the p regression coefficients $\boldsymbol{\beta}$. The model can be expressed as a system of linear equations (in $\boldsymbol{\beta}$):

$$\begin{pmatrix} \hat{y}_1 \\ \hat{y}_2 \\ \vdots \\ \hat{y}_m \end{pmatrix} = \begin{pmatrix} 1 & d_{11} & \cdots & d_{1n} & d_{11}^2 & d_{11}d_{12} & \cdots & d_{1(n-1)}d_{1n} & d_{1n}^2 \\ 1 & d_{21} & \cdots & d_{2n} & d_{21}^2 & d_{21}d_{22} & \cdots & d_{2(n-1)}d_{2n} & d_{2n}^2 \\ \vdots & \vdots & \ddots & \vdots & \vdots & \vdots & \ddots & \vdots & \vdots \\ 1 & d_{m1} & \cdots & d_{mn} & d_{m1}^2 & d_{m1}d_{m2} & \cdots & d_{m(n-1)}d_{mn} & d_{mn}^2 \end{pmatrix} \cdot \begin{pmatrix} \beta_0 \\ \beta_1 \\ \vdots \\ \beta_p \end{pmatrix}. \tag{3.33}$$

The regression coefficients are determined by the method of least squares [124] by minimizing the sum of squared errors

$$\min_{\boldsymbol{\beta}} \sum_{i=1}^{m} \epsilon_i^2 = \min_{\boldsymbol{\beta}} \sum_{i=1}^{m} (y_i - \hat{y}(\boldsymbol{d}^i, \boldsymbol{\beta}))^2. \tag{3.34}$$

The coefficient vector is given by

$$\boldsymbol{\beta} = (\boldsymbol{D}^{\boldsymbol{T}} \boldsymbol{D})^{-1} \boldsymbol{D}^{\boldsymbol{T}} \boldsymbol{y}, \tag{3.35}$$

where $p < m$ is a necessary condition for invertibility, so a minimum of p sampling points needs to be chosen. Once the coefficients are computed, the response at untried points can be obtained by (3.31). In the current work, the Python library scikit-learn [138] is used for the creation of the regression model.

3.6.2 Kriging

Kriging models are named after the South African mining engineer Danie G. Krige and originate from mining and geostatic applications [108]. Since established within the "Design and analysis of computer experiment" framework by Sacks et al. [153] in 1989, they have been extensively used as global approximation technique for the interpolation of deterministic computer simulations with various applications to structural optimization problems [166], [90], [167]. A Kriging model can be described as

$$y(\boldsymbol{d}) = f(\boldsymbol{d}) + Z(\boldsymbol{d}), \tag{3.36}$$

with a known approximation model $f(\boldsymbol{d})$, e.g., a polynomial model as mentioned in Section 3.6.1 plus the realization of a stochastic process $Z(\boldsymbol{d})$ with mean zero, variance σ^2, and non-zero covariance. While the polynomial provides a global trend of the underlying functional behavior, the stochastic process influences the local behavior and leads to the interpolating characteristic due to "local deviations" from the polynomial model. If a constant term is used ($f(\boldsymbol{d}, \boldsymbol{\beta}) = \beta$), this is denoted as ordinary Kriging (respectively if a constant and known term is used this is denoted as simple Kriging). A universal Kriging model is characterized by the use of an arbitrary linear regression model and can be expressed as

$$\hat{\boldsymbol{y}} = \boldsymbol{D}\boldsymbol{\beta} + \boldsymbol{Z} \tag{3.37}$$

with the design matrix $\boldsymbol{D}$ and the regression coefficients $\boldsymbol{\beta}$ introduced in the previous section and $\boldsymbol{Z}$ is a vector describing the stochastic process. The spatial covariance function of the stochastic process Z is given by

$$\mathrm{Cov}[Z(\boldsymbol{d}^i), Z(\boldsymbol{d}^j)] = \sigma^2 \boldsymbol{R}([R(\boldsymbol{d}^i, \boldsymbol{d}^j)]) \tag{3.38}$$

with the $m \times m$ symmetric correlation matrix $\boldsymbol{R}$ with a unit diagonal and the correlation function $R(\boldsymbol{d}^i, \boldsymbol{d}^j)$ between any combinations $\boldsymbol{d}^i$ and $\boldsymbol{d}^j$ of the m sampling points. The

correlation function has to be defined by the user and there exist different approaches [113]. A frequently used correlation function, that is also used in this work, is the Gaussian correlation function, which can be expressed as

$$R(\boldsymbol{d}^i, \boldsymbol{d}^j) = \prod_{l=1}^{n} \exp[-\theta_l |d_l^i - d_l^j|^2] \quad , \quad \theta_l \in \mathbb{R}^+ \tag{3.39}$$

with the associated unknown correlation parameters θ_l to be determined, and $|d_l^i - d_l^j|$ describing the distance of the lth component of the m sampling points $\boldsymbol{d}^i$ and $\boldsymbol{d}^j$. In some applications it is sufficient to use a single correlation parameter, which is then referred to as a isotropic model. The correlation paramters θ_l affects the influences of the stochastic process near the associated sampling points. A low value indicates a large correlation of the sampling points. For the construction of the Kriging model, the regression coefficients $\boldsymbol{\beta}$, the process variance σ^2, and the correlation parameters θ_l can be derived by maximum likelihood estimation. The estimated regression parameter are given by

$$\hat{\boldsymbol{\beta}} = (\boldsymbol{D}^T \boldsymbol{R}^{-1} \boldsymbol{D})^{-1} \boldsymbol{D}^T \boldsymbol{R}^{-1} \boldsymbol{y}. \tag{3.40}$$

One can observe the similarity with (3.35) for the response surface model. The estimation of the variance between the global model $f(\boldsymbol{d})$ and y is given as

$$\hat{\sigma}^2 = \frac{(\boldsymbol{y} - \boldsymbol{D}\hat{\boldsymbol{\beta}}) \boldsymbol{R}^{-1} (\boldsymbol{y} - \boldsymbol{D}\hat{\boldsymbol{\beta}})}{m}. \tag{3.41}$$

Both $\hat{\boldsymbol{\beta}}$ and $\hat{\sigma}^2$ are a function of $\boldsymbol{R}$ (and hence θ_l) and result by setting the partial derivatives of the natural logarithm of the likelihood function $\ln(L)$ with respect to these parameters equal to zero. For the derivation of the correlation parameters, no analytical solution can be derived in this way for many correlation functions. That means, estimations $\hat{\theta}_l$ have to be determined numerically by maximizing $\ln(L)$ as

$$\ln(L(\boldsymbol{\theta})) = -\frac{1}{2}[m \ln(\hat{\sigma}^2) + \ln|\boldsymbol{R}|] \rightarrow \max_{\theta_l > 0}, \tag{3.42}$$

where $|\boldsymbol{R}|$ denotes the determinant of $\boldsymbol{R}$. The n-dimensional nonlinear optimization problem (3.42) can be solved with a global optimization algorithm such as simulated annealing. The correlation matrix may be ill-conditioned if the sampling points are located close to each other and if special sampling schemes are used (the corresponding columns in $\boldsymbol{R}$ are then almost identical). If the correlation parameter θ_l are computed, both $\hat{\sigma}^2$ and $\hat{\boldsymbol{\beta}}$ can be predicted by (3.40) and (3.41). After the model parameter has been identified, the Kriging prediction $\hat{y}$ at unobserved points $\boldsymbol{d}$ can be expressed as

$$\hat{y} = \boldsymbol{f}^T(\boldsymbol{d})\boldsymbol{\beta} + \boldsymbol{r}^T(\boldsymbol{d})\boldsymbol{R}^{-1}(\boldsymbol{y} - \boldsymbol{D}\boldsymbol{\beta}), \tag{3.43}$$

where the vector $\boldsymbol{f}(\boldsymbol{d})$ corresponds to the row of $\boldsymbol{d}$ in $\boldsymbol{D}$, the correlation vector $\boldsymbol{r}^T(\boldsymbol{d}) = [R(\boldsymbol{d}, \boldsymbol{d}^1), R(\boldsymbol{d}, \boldsymbol{d}^2), \ldots, R(\boldsymbol{d}, \boldsymbol{d}^m)]^T$ describing the individual correlations between an

untried point $\boldsymbol{d}$ and the sampling points $\{\boldsymbol{d}^1, ..., \boldsymbol{d}^m\}$, the vector $\boldsymbol{y}$ containing the values of the sample responses, and the residual vector $(\boldsymbol{y} - \boldsymbol{D\beta})$. In the current work, the surrogate modeling toolbox (Python library SMT) [22] is used for the creation of Kriging models. There are also Kriging models with special correlation functions leading to approximation models that are used, for example, in the presence of noise [48]. It can be shown that Gaussian process regression, which is especially used in machine learning applications, provide identical expressions as the Kriging model under the assumption of a multivariate normal distribution of the response data [144].

3.6.3 Surrogate model validation

Each surrogate model is just an approximation of the original (e.g., simulation) model and must be verified with respect to its accuracy. In general, this is done by evaluating its residuals, i.e., the difference between the exact model response, denoted in the following as f_i and the predicted response from the surrogate $\hat{f}_i$ at different points in the design space. For interpolating models the function value is equal to the value of the numerical model, so it makes no sense to acces the quality of the surrogate using these points. Different strategies and several error measures can be used to account for the accuracy of the surrogate model [88]. The most simple approach is to split the dataset into a training and a test data set. In that case, the surrogate model is created only with the training data and the test data are used to access the accuracy of the model. Typical sizes of these sets are 80% of all samples for the training and the remaining 20 % serve as validation data. That method has the drawback that the error highly depends on the chosen test data set, especially if the data set is relatively small. It is therefore important to use a sufficiently large data set that covers the entire design space. Often, additional datasets have to be created by performing additional simulations. To overcome this, cross validation [111] (CV) methods have been developed. In k-fold CV, the sample data are split in k subsets. The surrogate is fitted k times using $k-1$ subsets for the training of the model and the remaining subset for the validation of the model. The error e of the model can be then predicted by the mean average of the k errors. If k equals the sample size, the method is called leave-one-out CV. In the following, l denotes the number of validation points. There exist several error measure to account for the accuracy of the surrogate model. The mean squared error

$$e_{\mathrm{MSE}} = \frac{\sum_{i=1}^{l}(f_i - \hat{f}_i)^2}{l}, \tag{3.44}$$

the root mean squared error

$$e_{\mathrm{RMSE}} = \sqrt{\frac{\sum_{i=1}^{l}(f_i - \hat{f}_i)^2}{l}}, \tag{3.45}$$

the mean absolut error

$$e_{\mathrm{MAE}} = \frac{\sum_{i=1}^{l} \left| f_i - \hat{f}_i \right|}{l}, \tag{3.46}$$

the mean absolut percentage error

$$e_{\mathrm{MAPE}} = \frac{\sum_{i=1}^{l} \frac{|f_i - \hat{f}_i|}{f_i}}{l} \cdot 100\%, \tag{3.47}$$

the maximum absolute error

$$e_{\mathrm{MaxAE}} = \max \left| f_i - \hat{f}_i \right|, i = 1, ..., l, \tag{3.48}$$

and the coefficient of determination, denoted as R^2 score

$$R^2 = 1 - \frac{\sum_{i=1}^{l} (f_i - \hat{f}_i)^2}{\sum_{i=1}^{l} (f_i - \overline{f})^2} = \frac{\sum_{i=1}^{l} (\hat{f}_i - \overline{f})^2}{\sum_{i=1}^{l} (f_i - \overline{f})^2} \tag{3.49}$$

where $\overline{f}$ represent the mean value of the responses and a value of 1 indicates a perfect fit. While e_{MSE}, e_{RMSE}, e_{MAE}, and e_{MAPE} provide measures for the overall accuracy, e_{MaxAE} accounts for the local accuracy of the surrogate model. The advantage of the e_{MAPE} is that it accounts for the relative deviations, which is useful if the responses differ strongly in their values.

3.7 Sensitivity analysis

The functional relationship $\Psi_{ij,\mathrm{eff}} = \Psi_{ij,\mathrm{eff}}(\boldsymbol{d})$ can be viewed as a black box model describing a more or less complex relation that might not be well understood. Gaining an understanding of which design variables have the greatest impact on the effective properties is crucial in material design. In order to evaluate the contribution of individual input parameters to the variability of the output, sensitivity analysis methods [77] are suitable and commonly used in engineering. As stated in Saltelli [155], sensitivity analysis is the study of how the uncertainty in the output of a mathematical model (numerical or otherwise) can be divided and allocated to different sources of uncertainty in its inputs. These methods can be classified into local and global sensitivity analysis methods [70]. In line with the objective of this work, the focus here is on global methods to get a deeper understanding of the SPR within the entire design domain. In the following, some basic concepts of variance-based sensitivity analysis are briefly reviewed and Sobol' indices [170] are introduced as corresponding sensitivity measures. The importance of surrogate models for the computation of these indices is highlighted. A comprehensive introduction to global sensitivity analysis can be found in the textbook of Saltelli et al. [156] and Saltelli [154].

3.7.1 Sobol' indices

In variance-based sensitivity analysis [155], [171], the variance of the model output is decomposed into terms attributed to the model input parameters and their interactions. Assuming the model of interest as a function $y = f(\boldsymbol{x})$ with the independent parameter $\boldsymbol{x} = (x_1, ..., x_n)$ being a square-integrable function defined in the n-dimensional unit hypercube, i.e., $\boldsymbol{x} \in [0,1]^n$, it can be shown that y can be expressed as

$$f(\boldsymbol{x}) = f_0 + \sum_{i=1}^{n} f_i(x_i) + \sum_{i<j}^{n} f_{ij}(x_i, x_j) + ... + f_{12...n}(x_1, x_2, ..., x_n), \tag{3.50}$$

where in the following the notations $f_i(x_i) = f_i$, $f_{ij}(x_i, x_j) = f_{ij}$, etc. will be used. This expansion is unique [171], if the orthogonality condition

$$\int_0^1 f_{i_1...i_s}(x_{i_1}, ..., x_{i_s})\, \mathrm{d}x_{i_w} = 0 \tag{3.51}$$

with $1 \leq w \leq s$ and $\{i_1, ..., i_s\} \subseteq \{1, ..., n\}$ holds. Due to this orthogonality, the terms in (3.50) can be described by the conditional expectations of y as

$$\begin{aligned} f_0 &= E(y), \\ f_i &= E_{\boldsymbol{x}_{\sim i}}(y|x_i) - f_0, \\ f_{ij} &= E_{\boldsymbol{x}_{\sim ij}}(y|x_i, x_j) - f_i - f_j - f_0, \end{aligned} \tag{3.52}$$

and so on for higher-order terms, where the notation $\boldsymbol{x}_{\sim i}$ denotes the set of all factors except x_i. This means that f_i describes the effect of the sole variation of x_i. Furthermore, f_{ij} reflects the effect of a simultaneous variation of x_i and x_j in addition to the effect of their individual variations, hence it is called a second-order interaction. Squaring both sides of (3.50) and integration over the hypercube yields the variance of the model output

$$V = \int_0^1 f^2(\boldsymbol{x})\, \mathrm{d}\boldsymbol{x} - f_0^2 = \sum_{i=1}^{n} V_i + \sum_{i<j}^{n} V_{ij} + ... + V_{12...n} \tag{3.53}$$

with

$$\begin{aligned} V_i &= V_{x_i}[E_{\boldsymbol{x}_{\sim i}}(y|x_i)], \\ V_{ij} &= V_{x_{ij}}[E_{\boldsymbol{x}_{\sim ij}}(y|x_i, x_j)] - V_i - V_j, \end{aligned} \tag{3.54}$$

and so on. Expression (3.53) indicates that the variance of the model output can be decomposed into terms that can be assigned to the individual model inputs and their interactions. Based on this, the following global sensitivity indices are derived.

First-order indices

The first-order Sobol' indices S_i [171] are given as

$$S_i = \frac{V_i}{V(y)} \tag{3.55}$$

and can be interpreted as the contribution of the output variance by varying x_i alone (depicting the main effect of x_i). Dividing (3.53) by $V(y)$, it can be observed that the sum of all $2^n - 1$ first and higher-order indices sum up to one, i.e.,

$$\sum_i^n S_i + \sum_{i<j}^n S_{ij} + ... + S_{12...n} = 1. \tag{3.56}$$

The indices related to higher-order terms (S_{ij}, etc.) are formed in an analogous manner and represent the fraction of V caused by interaction effects of the corresponding inputs.

Total-order index

The so-called total-order index S_{T_i} [70] is defined as

$$S_{T_i} = \frac{E_{\boldsymbol{x}_{\sim i}}[V_{x_i}(y|\boldsymbol{x}_{\sim i})]}{V(y)} = 1 - \frac{V_{\boldsymbol{x}_{\sim i}}[E_{x_i}(y|\boldsymbol{x}_{\sim i})]}{V(y)}. \tag{3.57}$$

Compared to the first-order indices, the total-order index indicates the contribution to the model output variance caused not only by the main effects of x_i, but also by all higher-order interactions of x_i with any other model input parameter. The S_{T_i} is often used to rank the importance of the individual inputs for the model response and to identify insensitive model parameters. Please note that contrary to the first-order indices, $\sum_i^n S_{T_i} \geq 1$ due to the fact that interactions contribute to each individual S_{T_i}. They only sum up to one if there exist no interactiones, i.e., only main effect occur.

Computation of the indices

Since the variances cannot be determined analytically by evaluating the integral expressions of the functional decomposition, a standard practice is to estimate the indices based on the following sampling schemes [155]:

$$\begin{aligned} V_{x_i}[E_{\boldsymbol{x}_{\sim i}}(y|x_i)] &\approx \frac{1}{N}\sum_{j=1}^{N} f(\mathbf{B})_j (f(\mathbf{A}_{\mathbf{B}}^{(i)})_j - f(\mathbf{A})_j), \\ E_{\boldsymbol{x}_{\sim i}}[V_{x_i}(y|\boldsymbol{x}_{\sim i})] &\approx \frac{1}{2N}\sum_{j=1}^{N} (f(\mathbf{A})_j - f(\mathbf{A}_{\mathbf{B}}^{(i)})_j))^2. \end{aligned} \tag{3.58}$$

In 3.58, $\mathbf{A}$ and $\mathbf{B}$ are $(m \times n)$ sampling matrices created by m sampling points within the n-dimensional input space and $(\mathbf{A})_j$ denotes the jth row of $\mathbf{A}$. Moreover, $\mathbf{A}_{\mathbf{B}}^{(i)}$ indicates that the ith column from $\mathbf{B}$ is the ith column of $\mathbf{A}$, while the other columns remain unchanged. For the creation of the matrices, different sampling schemes can be used. A common approach is the use of (quasi) Monte-Carlo sampling [170] or LHS. The usually large number of samples required to appropriately compute the indices can be considered as a main drawback of this method and again emphasizes the benefits of surrogate models. In the work at hand, the Python library SALib [78], [63] is used to compute the Sobol' indices.

3.8 Optimization

In this section, some basic terms and definitions of structural optimization are summarized. The standard form of structural optimization problems is introduced and some common optimization methods for solving such problems are briefly reviewed. A comprehensive description of these methods is beyond the scope of this thesis, so reference is made to literature at appropriate places. Solely the optimization algorithms used in this thesis are described in more detail.

3.8.1 Basic terms and definitions

In structural optimization, a classical distinction is made between three different disciplines: Sizing, shape optimization and topology optimization. In **size optimization**, the shape and topology of the structure are kept fixed, and the design variables provide a description of the dimension (the size) of the structure, e.g., the thickness of sheets. In **shape optimization** problems, the objective is to determine an optimal geometry of the structure and the design variables represent the shape of the material boundaries. In contrast, **topology optimization** considers the overall shape (topology) of the structure by determining a distribution of the material. The problems considered in this work can be assigned to the discipline of sizing. A review about structural optimization and its historical development can be found for example in the publications [182], [183]. Furthermore, there exist several excellent textbooks, e.g., [87], [57], or more recently [33], which present a comprehensive insight to structural optimization methods.

The standard formulation of a structural optimization problem is given as follows:

$$\begin{aligned} & J(\boldsymbol{d}) \rightarrow \min && \boldsymbol{d} \in \mathbb{R}^n \\ \text{s. t.} \quad & g_j(\boldsymbol{d}) \leq 0 && j = 1, ..., J \\ & h_k(\boldsymbol{d}) = 0 && k = 1, ..., K \\ & d_{i,low} \leq d_i \leq d_{i,up} && i = 1, ..., n. \end{aligned} \tag{3.59}$$

The target of optimization is to find values of the design variables $\boldsymbol{d}$ that minimize the objective function J without violating some constraints. The constraints are distinguished between **inequality constraints** $g_j(\boldsymbol{d})$ and **equality constraints** $h_k(\boldsymbol{d})$. If there are neither inequality or equality constraints, the problem is called an **unconstrained** optimization problem, otherwise it is a **constrained** problem. The design variables $\boldsymbol{d}$ are limited by lower and upper bounds $d_{i,low}$ and $d_{i,up}$, also called **side constraints**, defining the **design space**. If the design variables can take any value within these bounds, they are **continous** while they are called **discrete** if they can take only certain values within the design space. In this thesis, only continous design variables are considerd. Designs that fulfill the constraints are denoted as **feasible** designs. If the objectives and constraints are linear in their design variables, the problem is called a **linear programming** problem. In general, this is not the case, and (3.59) describes a **nonlinear** structural optimization problem. The solution vector of the optimization problem is denoted as $\boldsymbol{d}^*$ and can be a **local** or a **global** optimum. Please note that a maximation problem $J(\boldsymbol{d}) \rightarrow \max$ can be transferred into a minimization problem by the expression $-J(\boldsymbol{d}) \rightarrow \min$. If there is more then one objective function to be minimized, the problem becomes a **multi-objective optimization** (MOO) problem. That special case will be described in Section 3.8.6 in more detail. An optimization problem can be classified if it is convex or not. The notion of convexity for the objective function and the admissible set will be introduced now. A set of points $\boldsymbol{S}$ is called a convex set, if for all $\boldsymbol{d}^1, \boldsymbol{d}^2 \in \boldsymbol{S}$ and all $0 \leq \alpha \leq 1$ the following condition holds:

$$\alpha \boldsymbol{d}^1 + (1-\alpha)\boldsymbol{d}^2 \in \boldsymbol{S}. \tag{3.60}$$

Roughly spoken, condition (3.60) means that each line segment between two arbitrary points $\boldsymbol{d}^1$ and $\boldsymbol{d}^2$ lies completely in $\boldsymbol{S}$. This is illustrated in Fig. 3.9.

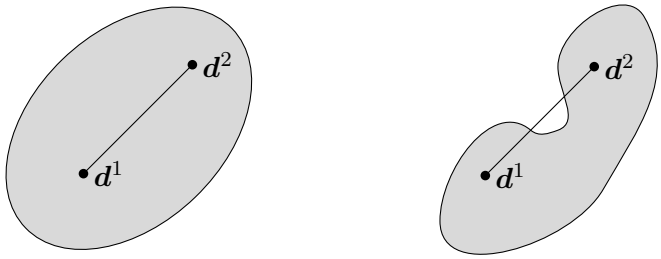

Figure 3.9: Convex (left) and non-convex set (right)

A function is denoted as convex if it is defined on a convex set and if the following condition holds:

$$J(\alpha \boldsymbol{d}^1 + (1-\alpha)\boldsymbol{d}^2) \leq \alpha J(\boldsymbol{d}^1) + (1-\alpha) J(\boldsymbol{d}^2). \tag{3.61}$$

This is illustrated in Fig. 3.10. An optimization problem is denoted as **convex** if the objective function is convex and the feasible set described by the constraints is a

convex set. Such convex problems possess the important property that there exist only one optimum, which is also the global optimum. In engineering practice it is generally difficult to prove (also in the considered material optimization problems) if a optimization problem is convex or not since there is no explicit expression for the objective function. There are some algorithms that rely on the construction of local convex subproblems of the nonlinear optimization problem to find an optimal solution. A very efficient method of this kind is the so-called sequential quadratic programming (SQP) method [129], which uses quadratic approximations of the objective function and linear approximations of the constraints.

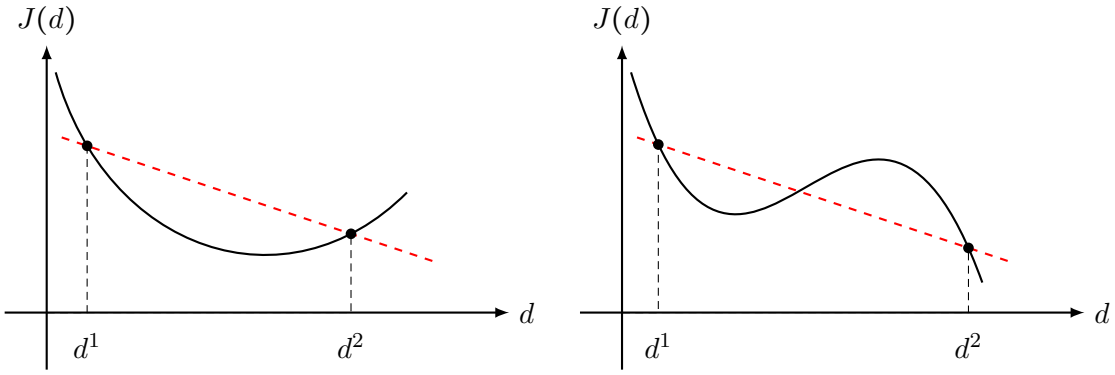

Figure 3.10: Convex (left) and non-convex function (right)

3.8.2 Optimization concepts

Most optimization methods attempt to iteratively determine the solution of the optimization problem, which involves evaluating the objective function and constraints. In the majority of engineering applications, it is not possible to explicitly formulate the objective function and the constraints, and these can only be determined pointwise by the evaluation of a simulation model (e.g., a finite element (FE) model). Two basic concepts can be distinguished in the optimization process. If the optimization is performed on the basis of the simulation model, this is often denoted as **direct optimization**. This approach seems intuitive and might be appropriate if the simulation is not too time-consuming and/or if relatively few iterations are required to find the optimum solution. In the context of this work, the evaluation of a design point involves the generation of a RVE and the application of different load-cases, which can be a time-consuming process. In such cases, it can be useful to create an approximation of the simulation model and to perform **metamodel-based optimization** [141]. The metamodel representation allows a fast evaluation of the system responses, so the efficiency of the optimizer (number of function evaluations) is not as important compared to direct optimization.

However, the main drawback of this procedure is that the approximation of the simulation model is always accompanied with an error. It must therefore be ensured that the metamodel can represent the exact simulation model sufficiently accurately and a validation of the optimization result must be performed by evaluating the numerical model. Metamodel-based optimization is widely used in simulation-based optimization with application in aerospace and automotive industry and has proven to be a powerful tool. In metamodel-based optimization, a distinction is often made between single and sequential approaches. In **single level** approaches, a metamodel of the entire design space is created with a fixed number of sampling points. If the approximation accuracy of that model is sufficient, optimization can be performed on this metamodel. There are also methods that, based on an initially created metamodel, **sequentially** add points in the design space to obtain the vicinity of the optimum. One of the most common methods make use of the so-called EI criterion, which is also considered in this thesis and described in further detail in Section 3.8.5. For a comprehensive overview of such sequential strategies, please refer to, e.g., [48], [141], and [187].

3.8.3 Overview of optimization algorithms

There are a variety of different methods for solving optimization problems in terms of (3.59). The selection of a suitable method needs to be chosen on the basis of the inidividual problem statement, e.g., if constraints are imposed or not, if the problem is convex or non-convex, or whether continuous or discrete design variables are to be considered. Due to these different circumstances, there is no "optimal" method that can be applied to every optimization task and is superior to all others. In the following, some of the most common optimization methods in structural optimization are briefly reviewed and only the methods used in the context of this work are mentioned in more detail. To get a more in-depth overview, reference is made to literature at the appropriate place.

There exist several ways to classify optimization methods. One often used is to differentiate between local and global methods. A **local** optimization method attempt to find a local optimum that is not guaranteed to be the global optimum if the optimization problem is non-convex. This means that in the presence of several local minima, different optima can be obtained depending for different starting points. The most common local optimization methods are gradient-descent algorithms. These make use of gradient information of the objective function and constraints to iteratively descend from a chosen starting point towards the closest local optimum. This can be described by the following generic rule:

$$\boldsymbol{d}^{i+1} = \boldsymbol{d}^{i} + \alpha \boldsymbol{s}^{i} \tag{3.62}$$

where in the first step, a search direction $\boldsymbol{s}^i$ is determined by making use of the gradient information. In the second step, a line-search is conducted and the step size $\alpha > 0$ to establish the next iterate $\boldsymbol{d}^{i+1}$ along the search direction is provided. This iterative

procedure is repeated until a specific termination criterion is met. The several gradient-descent algorithms differ in the kind to determine the search direction and the step size. They can be distinguished by the required order of gradient information. For example, the steepest descent method uses the direction of the steepest descent (the opposite gradient direction of the objective function) as search direction. This methods are widely used and are often very efficient with view of the number of iterations, even for high-dimensional problems. These methods are generally not suitable in discrete optimization problems and dealing with numerical noise can be difficult to handle. A detailed overview of these methods including the handling of constraints and further theoretical investigations like optimality conditions can be found in one of the numerous textbooks, e.g., [169], [8], or [57]. Since the gradients are usually not available in analytical form, they can be approximated by finite differences (FD). However, this is associated with a considerable additional effort and requires n additional analyses. It is particularly advantageous if the gradients can be determined analytically or semi-analytically from the simulation model via a sensitivity analysis, as is the case, for example, by linear FE analyses. This procedure allows a generally more efficient and more accurate determination of the gradients compared to the determination by FD. For the sake of completeness, it should be mentioned here that there are also local methods that do not use gradients (also denoted as non-derivative or zero-order methods). Two well-known non-derivative methods are Powell's method [139] and the Nelder-Mead method [127].

In many cases, one is interested in finding the global optimum of (3.59). In such cases, **global** optimization algorithms provide a better chance of finding the global optimum compared to local methods. A simple and common strategy of global optimization is to use a so-called multistart approach [34] whereby multiple local optimizations are performed from different starting points. These starting points can be generated for example with a DoE-scheme. According to [199], global optimization methods can be classified in deterministic and stochastic methods. Most of the deterministic methods make certain mathematical demands on the optimization problem, which usually do not exist in structural optimization problems. Because of that they will not be described in more detail here and reference should be made for example to [128]. Most stochastic methods are inspired by evolution in nature inspired by Darwin's theory of survival of the fittest. Evolutionary algorithms are probably the best known representatives of these stochastic methods. Pioneering work in evolutionary computation was carried out in the 1960s by Holland (genetic algorithms) [68] and by Rechenberg and Schwefel (evolution strategies) [19]. They employ randomly selected design points represented by a population and the individuals are rated by their fitness (objective function value). These methods contain elements like selection, crossover, mutation, and reproduction and attempt to iteratively find better solutions. Compared to gradient descent algorithms discussed so far, they do not require derivative informations and offer the advantages of being very robust (e.g., in the handling of noise) and being simple to implement. Some drawback of these methods

is that they often require significantly more iterations compared to local optimization methods, and the handling of constraints demands special attention. Further common stochastic methods are particle swarm optimization [85] and simulated annealing [86]. A more recent powerful stochastic method, differential evolution, will be described in more detail in the following due to its importance in the context of this work. Finally, it should be noted that there is no procedure that guarantees the finding of the global optimum and the term global should rather be understood in the sense of the global property regarding global optimization methods.

3.8.4 Differential evolution (DE)

Differential evolution (DE) belongs to the class of evolutionary algorithms and was first introduced by R. Storn and K. V. Price in [175] with the target to find the global optimum of objective functions defined in continous design spaces. Similar to other evolutionary algorithms DE is population-based, stochastic in its nature and includes evolutionary features like mutation, crossover, and selection. Unlike to other evolutionary algorithms, in DE, the candidate solutions are represented as real-value vectors and new candidates are generated by adding weighted differences between two vectors to a third vector. Due to its mode of operations it does not require derivative information and the presence of noise does in generally not lead getting stuck in a local optimum as this might be the case if a gradient descent method is used. There is no proof of convergence for DE, but it has been shown to be a simple and efficient method for a wide range of engineering optimization problems [37]. For example, DE was shown to be superior to simulated annealing in [175]. An overview of the state of the art relating to DE can be found in [37] or more recently in [6].

The main steps of the DE algorithm include initialization, mutation, crossover, and selection and are illustrated in Fig. 3.11. The three last steps are repeated until a certain termination criterion is met. In DE, only three parameters need to be specified, namely the population size N_p, the mutant factor F, and the crossover probability P_{cross}.

Initialization

In the first step, an initial population with a size of N_p individuums is randomly selected in the n-dimensional design space. In the following, the N_p parameter vectors (candidate solutions)

$$\boldsymbol{d}_{i,G} = [d_{1,i,G}, d_{2,i,G}, ..., d_{n,i,G}] \tag{3.63}$$

with $i = 1, ..., N_p$ and G denoting the generation number (respectively the iteration no.) are introduced. The initial candidate solutions $(G = 0)$ are generated as

$$d_{j,i,0} = d_{j,low} + \text{rand}_{i,j}[0,1] \cdot (d_{j,up} - d_{j,low}) \tag{3.64}$$

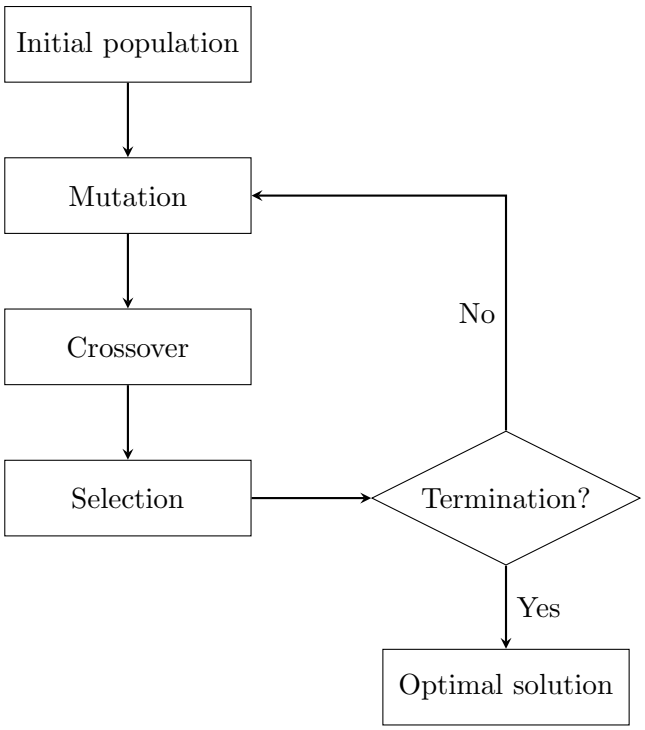

Figure 3.11: Main steps of the DE algorithm

expressed by the lower and upper bounds of the jth component of $\boldsymbol{d}_i$ and $\text{rand}_{i,j}$ describes uniformly distributed random numbers lying between 0 and 1.

Mutation

In the mutation phase, mutant vectors $\boldsymbol{v}_{i,G}$ are generated by a mutation operation on the basis of parent vectors from the actual generation, the so-called target vectors. There exist several mutation strategies. In the DE literature, different schemes are represented in the format DE/x/y/z, where x describes the base vector randomly perturbed in the mutation process, y is the number of involved difference vectors, and z stands for the type of crossover. Four commonly used mutation schemes are given as follows:

DE/rand/1:

$$\boldsymbol{v}_{i,G} = \boldsymbol{d}_{r_1,G} + F(\boldsymbol{d}_{r_2,G} - \boldsymbol{d}_{r_3,G}) \tag{3.65}$$

DE/rand/2:

$$\boldsymbol{v}_{i,G} = \boldsymbol{d}_{r_1,G} + F(\boldsymbol{d}_{r_2,G} - \boldsymbol{d}_{r_3,G}) + F(\boldsymbol{d}_{r_4,G} - \boldsymbol{d}_{r_5,G}) \tag{3.66}$$

DE/best/1:

$$\boldsymbol{v}_{i,G} = \boldsymbol{d}_{\text{best},G} + F(\boldsymbol{d}_{r_1,G} - \boldsymbol{d}_{r_2,G}) \tag{3.67}$$

DE/best/2:

$$\boldsymbol{v}_{i,G} = \boldsymbol{d}_{\text{best},G} + F(\boldsymbol{d}_{r_1,G} - \boldsymbol{d}_{r_2,G}) + F(\boldsymbol{d}_{r_3,G} - \boldsymbol{d}_{r_4,G}) \tag{3.68}$$

where $r_1, r_2, ..., r_5 \neq i \in [1, N_p]$ are indices of the candidate solutions and distinct from each other. The index r_1 denotes the base vector of the population and $r_2, ..., r_5$ are the indices of randomly selected candidate solutions used to construct the mutant vector. These indices were generated once for each mutant vector. The resulting mutant vector is called the donor vector. $\boldsymbol{d}_{\text{best},G}$ represents the best candidate solution used as target vector. F is a mutant factor in the range between 0 and 1. A value closer to 0 can be considered as a mutation strategy with more local character, while a value close to 1 has a more exploitative character. Thus, an appropriate choice of F is crucial for the convergence towards the global optimum [37].

Crossover

After the donor vector has been generated, a crossover operation is applied to maintain the diversity of the population. During the crossover, a so-called trial vector $\boldsymbol{u}_{i,G} = [u_{1,i,G}, u_{2,i,G}, ..., u_{n,i,G}]$ is formed by exchanging components from the donor vector and the target vector. In the binomial (uniform) crossover method, the trial vector is built as

$$u_{j,i,G} = \begin{cases} v_{j,i,G} & \text{if } \text{rand}[0,1] \leq P_{\text{cross}} \text{ or } j = k \\ d_{j,i,G} & \text{else} \end{cases} \tag{3.69}$$

with the crossover probability P_{cross} lying in the range between 0 and 1. $k \in [1, n]$ is a randomly chosen index instantiated once for each candidate solution per generation that ensures that the trial vector contains at least one element of the donor vector. Beside the uniform crossover, another crossover operation is given by exponential crossover [37].

Selection

In the selection phase, it will be determined which candidate solutions are considered during the next iteration. It is determined whether the trial vector or the target vector "survives" and builds the next generation. This can be desribed as

$$\boldsymbol{d}_{i,G+1} = \begin{cases} \boldsymbol{u}_{i,G} & \text{if } J(\boldsymbol{u}_{i,G}) \leq J(\boldsymbol{d}_{i,G}) \\ \boldsymbol{d}_{i,G} & \text{else.} \end{cases} \tag{3.70}$$

If the fitness (value of the objective function) of the trial vector $\boldsymbol{u}_{i,G}$ yields a lower value than the fitness of the target vector $\boldsymbol{d}_{i,G}$, the trial vector replaces the target vector for the next generation. Otherwise the target vector is retained. If the population of the

next generation has been formed, the steps of mutation, crossover, and selection are iteratively repeated (with the same number of individuums N_p) until termination. A version of DE to handle constraints using the concept of Pareto dominance (see Section 3.8.6) in the constrained design space is described in [100].

3.8.5 Efficient global optimization (EGO)

The efficient global optimization (EGO) algorithm was proposed in 1998 by Jones [81] and belongs to the class of Bayesian optimization [114] approaches. The method seems promising for optimization problems with an expensive to evaluate and potentially noisy objective function, where derivative informations are not available. In such techniques, the objective function is treated as a black box function and a statistical model is used to construct a surrogate model. Then, a sequential approach is used in an attempt to process as much information as possible about the underlying functional relationship to find the global optimum within a few iterations. Due to this mode of operation, the method seems highly suitable for solving the type of optimization problems considered in this work. As stated in the introduction, such approaches have been utilized in recent years in the context of material design [32].

The basic steps of EGO can be described as follows: In a first step, a limited number of sampling points will be selected based on a DoE scheme. As mentioned in Section 3.3.3, this should be a space-filling design gaining as much information as possible. The initial sampling points $\boldsymbol{D} = [\boldsymbol{d}^1, \boldsymbol{d}^2, ..., \boldsymbol{d}^m]$ are evaluated by the computer code yielding the responses $\boldsymbol{Y} = [y_1, y_2, ..., y_m]$, which are used to fit an initial Kriging surrogate $y = y(\boldsymbol{D}, \boldsymbol{Y})$ with mean prediction $\hat{y}(\boldsymbol{d})$ and (local) variance $\hat{s}^2(\boldsymbol{d})$. If the best observation of the initial designs is denoted by $y_{\min} = \min(\boldsymbol{Y})$, the improvement is defined as

$$I(\boldsymbol{d}) = \max(y_{\min} - y, 0). \tag{3.71}$$

The next sampling point (design) is selected based on a so-called aquisition function. As acquistion function, often the expected improvement (EI) [81], [160], defined as

$$E[I(\boldsymbol{d})] = E[\max(y_{\min} - y, 0)] \tag{3.72}$$

with the Kriging model output y is used. Expressing the expected value E in (3.72) by an integral and applying integration by parts leads to the following form of the expected improvement:

$$E[I(\boldsymbol{d})] = (y_{\min} - \hat{y}(\boldsymbol{d}))\Phi\left(\frac{y_{\min} - \hat{y}(\boldsymbol{d})}{\hat{s}(\boldsymbol{d})}\right) + \hat{s}(\boldsymbol{d})\phi\left(\frac{y_{\min} - \hat{y}(\boldsymbol{d})}{\hat{s}(\boldsymbol{d})}\right) \tag{3.73}$$

if $\hat{s}(\boldsymbol{d}) > 0$ and $E[I(\boldsymbol{d})] = 0$ otherwise. Moreover, Φ and ϕ denote the cumulative and probability density function of the standard normal distribution, respectively. Besides

the EI criterion, also other acquisition functions have been proposed. One of the most popular alternatives is the lower confidence bound (LCB), given as

$$\mathrm{LCB}(\boldsymbol{d}) = \hat{y}(\boldsymbol{d}) - \kappa \hat{s}(\boldsymbol{d}) \tag{3.74}$$

with a constant $\kappa > 0$. The next sampling point is computed by optimizing the acquisition function (e.g., maximizing the EI criterion), i.e.,

$$\boldsymbol{d}^{m+1} = \arg\max_{\boldsymbol{d}} \left(E[I(\boldsymbol{d})]\right). \tag{3.75}$$

By means of the EI criterion, an attempt is made to select those points in the design space at which the probability of an optimum is large, while also taking modeling inaccuracies into account. The first term in (3.73) is the exploitation term, where exploitation means sampling in areas of low mean prediciton. The second term is the exploration term, where exploration means sampling at locations of large uncertainty (variance of the model). Hence, EGO performs a trade-off between local (exploitation) and global (exploration) search to find the global optimum.

The individual steps of the employed EGO algorithm, implemented in the Python surrogate modeling toolbox (Python library SMT) [22], can be summarized as follows:

1. Select a relatively small set of an experimental design $\boldsymbol{D}$ and evaluate the responses $\boldsymbol{Y}$ at these points by running the computer simulation. Set counter to $i = 0$.
2. Use this data to create a Kriging surrogate model $y = y(\boldsymbol{D}, \boldsymbol{Y})$.
3. Select the next sampling point $\boldsymbol{d}^{i+1}$ by maximizing the EI criterion (3.73).
4. Evaluate the response at the new sample point $y_{i+1} = y(\boldsymbol{d}^{i+1})$ and expand the data set, $\boldsymbol{D} = [\boldsymbol{D}, \boldsymbol{d}^{i+1}], \boldsymbol{Y} = [\boldsymbol{Y}, y_{i+1}]$.
5. If the termination criteria is not satisfied, set counter to $i = i + 1$ and go back to step 2.

Finally, the algorithm returns the best solution find so far $y_{\min}$. Please note that no validation run is necesseray for this determined optimum, since this evaluation was performed directly on the mathematical (simulation) model. As termination criteria, for example, the value of the EI during the iterations can be considered until it is smaller than a specified value. The operation of the EGO algorithm is illustrated in Fig. 3.12 by means of a one-dimensional objective function. It can be observed that the exploiting term leads to the first sampling point near a local optimum. In the second iteration, the exploitation term is dominant and the next sampling point is selceted in the area of large variance. After a few iterations, the method detects the global optimum. An extention of the EI criterion to hande constraint is given in [161].

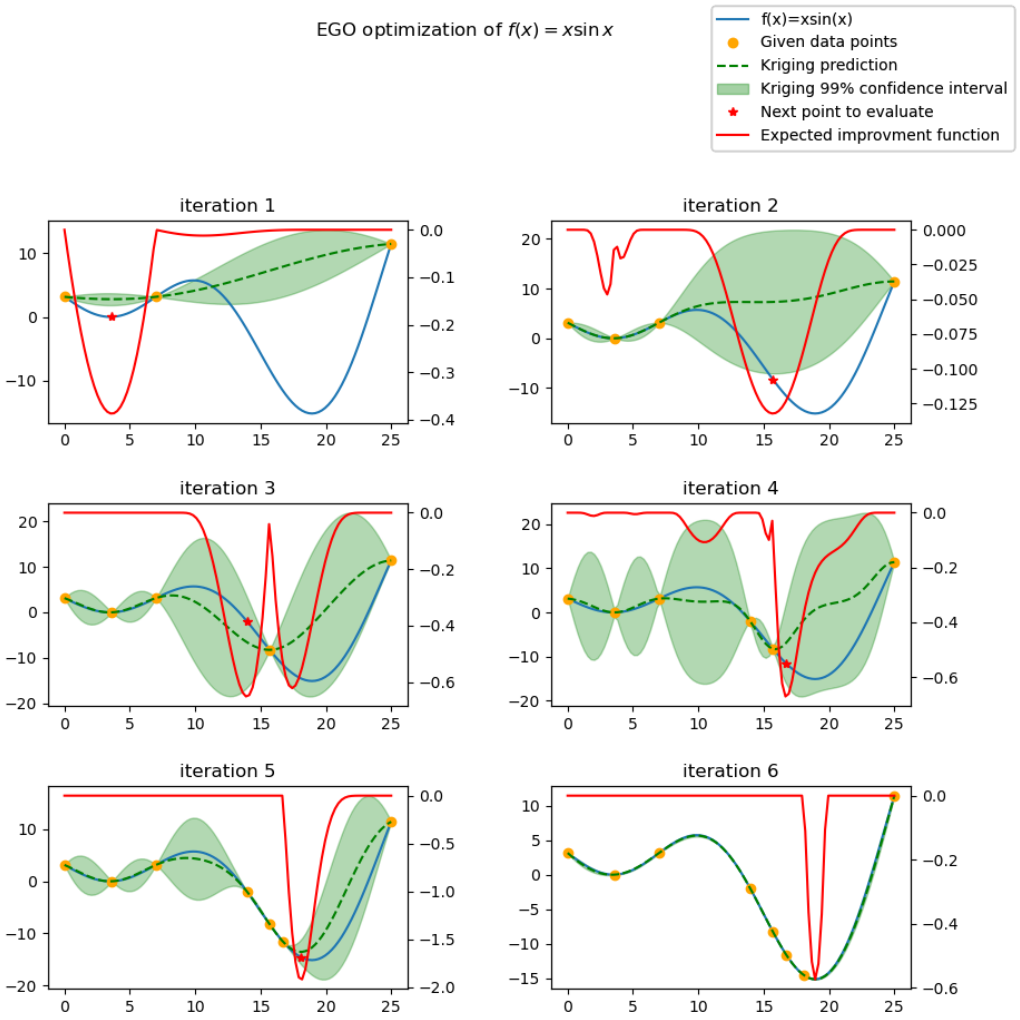

Figure 3.12: Operation of the EGO algorithm for a specified analytical objective function (Fig. taken from Python surrogate modeling toolbox (SMT) `https://smt.readthedocs.io/en/latest/_src_docs/applications/ego.html`, [22])

3.8.6 Multi-objective optimization (MOO)

Many technical applications require the consideration of several different design objectives. Because the focus of this thesis is on the optimization of thermal and mechanical material properties, simultaneous requirements on both physical material properties can be addressed by the formulation of multiple design objectives in a multi-objective optimization (MOO) problem. In the following, some basic notations and solution techniques for MOO problems are introduced. The general formulation of a MOO problem is given as

$$\begin{aligned} & J_m(\boldsymbol{d}) \rightarrow \min && m = 1, ..., M, \quad \boldsymbol{d} \in \mathbb{R}^n \\ \text{s. t.} \quad & g_j(\boldsymbol{d}) \leq 0 && j = 1, ..., J \\ & h_k(\boldsymbol{d}) = 0 && k = 1, ..., K \\ & d_{i,low} \leq d_i \leq d_{i,up} && i = 1, ..., n \end{aligned} \tag{3.76}$$

with $M \geq 2$ objective functions represented by the design objective vector $\boldsymbol{J}(\boldsymbol{d})$ to be minimized, so sometimes MOO is referred as vector optimization. The remaining notations introduced for the standard form of nonlinear (single-objective) optimization problems (see (3.59)) apply here analogously. Due to the consideration of multiple design objectives, each desicion vector $\boldsymbol{d} \in \mathbb{R}^n$ can be mapped into an design objective space $\boldsymbol{J}(\boldsymbol{d}) = \boldsymbol{z} = (z_1, ..., z_M)^T \in \mathbb{R}^M$. This is illustrated in Fig. 3.13. Compared to single-objective optimization problems, there exist in general no feasible decision vector that minimizes all design objectives simultaneously. MOO problems possess a set of solutions that can be regarded as the best trade-offs between competing design objectives. More precisley, a solution of (3.76) is indicated by a feasible desicion vector $\boldsymbol{d}^*$ (and the corresponding design objective vector $\boldsymbol{z}^*$) that cannot be improved in any objective without deteriorating at least one other design objective. Such a solution is called Pareto optimal or Pareto efficient. For a more formal definition of Pareto optimal solutions, the notion of dominance is introduced. A decision vector $\boldsymbol{d}^1$ is said to dominate another decision vector $\boldsymbol{d}^2$ if it is feasible and

$$\forall\, m \in \{1, ..., M\}, J_m(\boldsymbol{d}^1) \leq J_m(\boldsymbol{d}^2) \quad \wedge \quad \exists\, m \in \{1, ..., M\}, J_m(\boldsymbol{d}^1) < J_m(\boldsymbol{d}^2). \tag{3.77}$$

The Pareto optimal set is given by the set of all non-dominated (Pareto optimal) solutions and the representation of this set in the design objective space is denoted as Pareto front. This is illustrated in Fig. 3.13 for $n = m = 2$.

Several methods have been developed to solve MOO problems [55]. The selection of a method depends, inter alia, whether single solutions of the front are sufficient or if the entire front should be determined. According to [75], these methods can be categorized as non-preference, a priori, a posteriori, and interactive methods, depending on the point in time at which a decision is made between different solutions. In the following, a basic

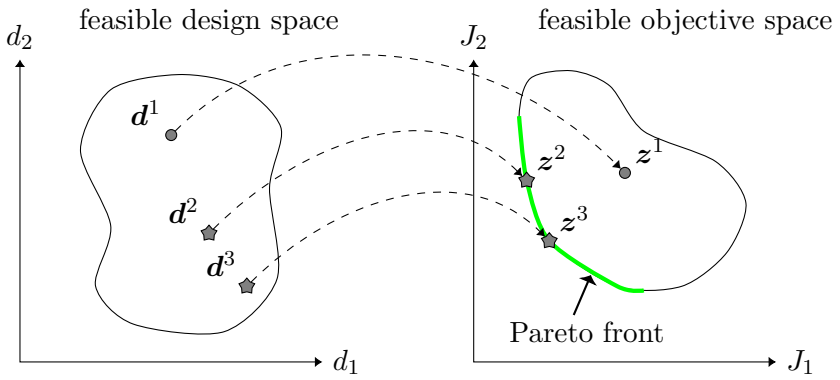

Figure 3.13: Design variable space (left) and objective function space (right)

overview of essential solution concepts will be provided. For a comprehensive overview, please refer to the specialist literature, e.g., [24], [41].

The most basic idea is to transform the MOO problem (3.76) into a single-objective problem that can then be solved by standard methods. A common approach is to formulate the single-objective function as a weighted sum of the individual design objectives as $\tilde{J}(\boldsymbol{d}) = \sum_{i=1}^{M} w_i J_i$ [36]. The selection of the weighting factors is based on the relative importance of the respective objective function. Depending on the choice of these weighting factors, different points of the Pareto front are obtained. However, it is not possible to find solutions in this way if the Pareto front is not convex. Another approach is to optimize only a single objective function (typically the most important one) and to treat all other objectives as constraints, as in the ϵ-constraint method [200]. These methods belong to the class of a priori methods because by the definition of the weights or the definition of the constraints one selects preference information before a solution of the MOO problem is found. Both approaches suffer from the disadvantage that good knowledge of the optimization problem (i.e., the relevance of the individual design objectives) is required, which is often not the case. Moreover, only individual points of the Pareto front are obtained, i.e., several optimization runs are necessary to determine an approximation of the Pareto front.

In the context of this work, it is of interest to obtain a wide variety of solutions. For that purpose, multi-objective evolutionary algorithms (MOEAs) have been developed over the past three decades and are nowadays frequently used in engineering applications [181], [38]. Because MOEAs operate on a set of candidate solutions exchanging information with each other, they are promising for finding different Pareto optimal solutions within a single optimization step. The requirements for these algorithms are generally to find a set of solutions that are close to the Pareto front (convergence), to

find well-distributed solutions that represent the entire Pareto front (diversity), and to cover the entire Pareto front (coverage). There are a multitude of different approaches, which are reflected in a corresponding amount of different MOEAs. A classification of MOEAs can be found in [181]. The basic elements of MOEAs should be explained by the well-known NSGAII algorithm, which is also used in this work. There are also indicator-based and decomposition-based MOEAs specifically designed for MOO problems, as well as hybrid MOEAs. These cases are not covered in this thesis, so these methods are not described further.

In the NSGAII algorithm, three main elements are applied: Ranking, elitism, and diversity preservation. Ranking is performed by iteratively assigning a rank to the candidate solutions based on their dominance (the dominance criterion is used to rate the fitness). Such a ranking based on Pareto dominance was first proposed in 1989 by Goldberg [52]. In a first step, all candidates that are not dominated by any other individual are assigned the best rank, rank 1. Subsequently, the non-dominated individuals with rank 1 are removed and the individuals that are not dominated by any of the remaining candidates are assigned rank 2. This process is repeated until all candidates have been assigned a rank. The steps of the NSGAII algorithm can be summarized as follows:

1. Initialize a population of size N_p and evaluate the corresponding objective and constraint functions. Rank the individuals using the non-dominance criterion. Determine the crowding distance of each candidate.

2. Generate a child population of size N_p by applying evolutionary operators such as selection, crossover, and mutation and evaluate the child population.

3. Combine parent- and child population. Perform ranking and compute the crowding distances.

4. Employ elitism: Select the N_p best individuals from the combined population on the basis of the ranking and the crowding distances. These individuals build the parents of the next generation.

5. If termination criteria is not met, repeat and go back to step 2.

The crowding distance is a simple measure to compare the relative closeness (the diversity) of a solution in the design objective space to other solutions. If individuals have the same rank, this measure allows to differentiate between them and the most distant solutions are preferred to preserve the diversity of the Pareto optimal solutions. The elitism approach ensures that Pareto optimal solutions are not deleted during the iterations by selecting only the individuals with the best rank. The MOEAs belong to the class of a posteriori methods, because preference information is given after a set of Pareto optimal solutions has been identified. A simple extension for dealing with constraints is provided in [38].

3.9 Robust design optimization

3.9.1 Introduction

In the generic material optimization problem (3.1), the design variables were treated as deterministic values. The solution of this optimization problem with one of the optimization methods presented in Section 3.8 yields a deterministic optimal design. When manufacturing a material, it is almost impossible to realize such an optimal design exactly, as there exist various uncertainties along the PSP processing chain. This should be illustrated by means of the parameterized PRC introduced in Section 3.1.1. The design variables of the geometrical microstructure may exhibit deviations in terms of the size of the filler particles d_{sp} or the filler volume fraction V_f. There may also be deviations in the design variables of the material properties. In the context of this example, this means deviations in the conductivities of the matrix k_m and the filler k_p. These uncertainties can lead to a design that is very sensitive to variations in the design variables. Hence, one is interested in a design that is robust. Roughly spoken, a design can be said to be robust, if it is unsensitive in view of uncertainties in the design variables. The question of how these uncertainties affect the performance of a design and how to identify a robust solution is the subject of robustness evaluation and robust design optimization techniques [101], [135]. The concept of robust optimization is illustrated in Fig. 3.14 using a 1D function. As depicted in this example, a variation in the design variables Δd may result that the robust optimum differs from the global optimum. In the following, the kind of uncertainty as well as the robustness measure considered in that work are introduced. Based on that, the evaluation of the robustness of a microstructural design and the formulation and solution of the robust design optimization problem is mentioned. A comprehensive survey of robust optimization is provided by [20].

3.9.2 Robustness evaluation and solution of robust optimization problems

To account for uncertainties in the design variables during material design, they need to be included in the material optimization problem (3.1). Within the scope of this work, the uncertainties are not modeled in terms of a probability density function, so the robust optimization approach considered here is non-probalistic (deterministic). The reason for this is that such functions are not known in general. There exist different measures to quantify the robustness of a design. Commonly used metrics are, e.g., the expected value and the variance. But there are many other statistical measures, including standard deviation, quantile, and so on. An comprehensive overview can be found, for example, in [147]. In this work, the worst-case criterion is employed for the quantification of the robustness of microstructural designs. For this purpose, a hypercube

$$U(\boldsymbol{d}^{\star}, \delta) = \{\xi \in \mathbb{R}^n \mid d_i^{\star}(1-\delta) \leq \xi \leq d_i^{\star}(1+\delta)\} \tag{3.78}$$

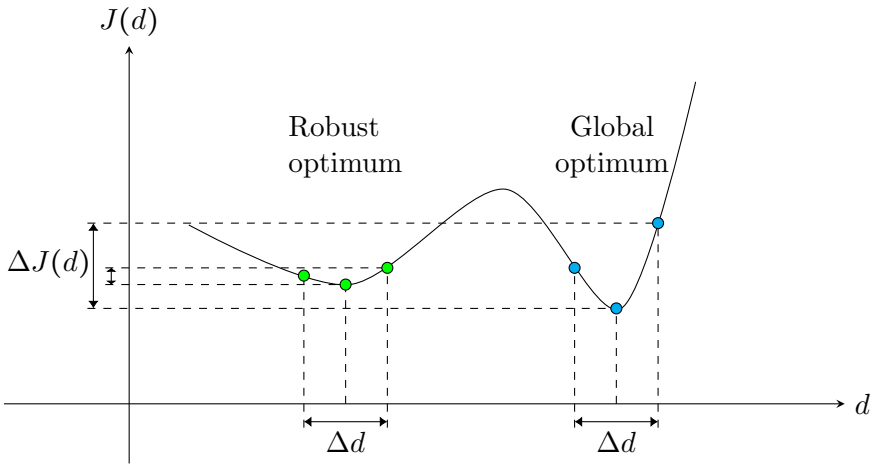

Figure 3.14: Global- and robust optimum

with $i = 1, ..., n$ centered around an optimal design $\boldsymbol{d}^*$ is considered. The size of the hypercube is specified by the parameter δ and should be selected to cover the relevant variations of the design variables (see Fig. 3.14 for an illustration). The worst-case criterion assigns $J(\boldsymbol{d}^*)$ the maximum value of the objective function within the hypercube

$$\rho_R(\boldsymbol{d}^*) = \max_{\xi \epsilon U(\boldsymbol{d}^*, \delta)} J(\xi). \tag{3.79}$$

In robust optimization, the objective function is replaced by a robust counterpart. Criterion (3.79) can be used to form this robust counterpart. In that way, a design is obtained, where the maximum of the objective function within the hypercube (the worst-case) is minimal, so it is often referred to as min-max principle [39] or robust regularization [102]. The selection of the robustness measure depends on the requirements of the considered problem. For example, the worst-case criterion should be chosen, if the worst-case should be avoided in each case. If the result should be quite good in an average sense, the expected value is a more appropriate criterion, whereas the standard deviation is a good choice, if the variance is to be taken into account. Finally, the robust optimization problem has to be solved with appropriate methods. The crucial point in the computation of robustness measures is in general the high computational effort because it often requires the evaluation of integrals. Common strategies of how to do so are sampling methods, especially Monte-carlo sampling or Taylor series expansions. A detailed overview is beyond the scope of this work and can be found, e.g., in [20] or [16]. For the worst-case criterion, this includes an (additional) optimization to evaluate the criterion. From the construction of the criterion, it can be observed that (3.79) is not differentiable. For the evaluation of this maximization problem, the DE algorithm according to Section 3.8.4 is employed in this work. Since surrogate-based optimization is performed, the com-

putational burden associated with the evaluation of (3.79) as well as the optimization procedure itself becomes managable.

Chapter 4

Polymer matrix composites

4.1 Introduction

Composites are materials composed of two or more materials that are bonded together. With the use of composites one attempts to combine the beneficial properties of the individual constituents into a new material. As illustrated in Fig. 4.1, composites can be distinguished by the type of reinforcements [149] into particle reinforced, fiber reinforced, and sheet molding composites. Composites can also be classified according to the base material, the so-called matrix. A distinction is made here between polymers, metals and ceramics. The focus of this work is on polymer matrix composites consisting of fibers or particulate fillers embedded in a continuous polymer matrix.

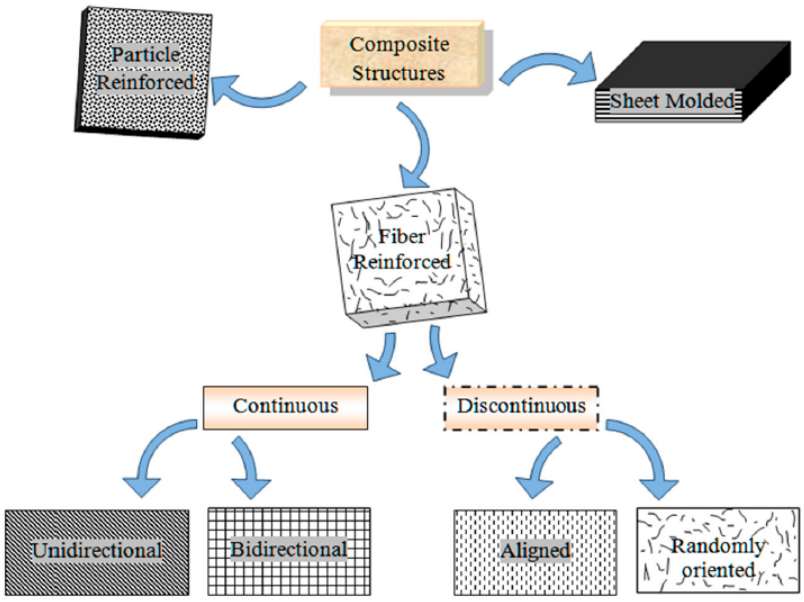

Figure 4.1: Classification of composites according to the type of reinforcement (Fig. taken from [142])

Polymers are commonly employed as matrix materials in engineering applications due to their low density, easy moldability, and low costs. The use of certain fillers is an attempt to achieve a material property required for a specific application. Therefore, the term functional fillers is often used. Various filler particles with different physical properties and geometric shapes are available for this purpose. It should be noted that only fillers in the micrometer range are considered in this work, so nanocomposites are not covered here. The properties of the composite depend essentially on the physical properties of the individual constituents, their composition, the structure of the fillers, and the effects at the interfaces of matrix and filler. These properties are also influenced by the manufacturing process. This section provides an overview of fiber reinforced and particle reinforced polymers. The technical relevance of these materials is addressed and common matrix and filler materials are described.

4.2 Fiber reinforced polymers

Fiber reinforced polymers (FRPs) consists of a polymer matrix reinforced with fibers of high stiffness and strength. The combination of polymer and fibers results in a composite with beneficial stiffness/strength-to-weight ratio. Therefore, these materials are predestined for use in lightweight construction applications. FRPs offer other exceptional properties [142], such as superior durability, damping properties, flexural strength, and resistance to wear, impact, and corrosion. Hence, FRPs are increasingly replacing traditional materials such as neat polymers and steels in the automotive industry [105]. Further applications can be found in the civil, mechanical, aerospace, biomedical, and marine sectors, see [142] or [104] for an overview. Due to the possibility of aligning the fibers in different (load) directions, FRPs generally exhibit a direction-dependent material behavior. This provides the opportunity to design anisotropic composites according to specific macroscopic requirements. FRPs can be distinguished according to the length of the fibers in continuous (long) and discontinuous (short) fiber reinforced polymers. The fibers are referred as continuous fibers if they have a length of more than a few millimeters. Continuous fiber reinforced polymers often contain a large fiber volume fraction (e.g., 60 %) and the fibers are aligned along the load direction. In order to achieve maximum strength and stiffness in multiple load directions, continuous fibers are prefabricated in the form of woven fabrics embedded in a thermoset polymer. In contrast, short fibers typically have a length of less than 1 millimeter and are often randomly aligned. In the context of this work, only SFRPs are considered. The probably most common SFRPs are glass fiber reinfored polymers (GFRPs). In 2014, a total of 1.043 kt of GFRPs was processed in Europe [96]. Most components made of GFRP are manufactured via cost-effective injection molding. As raw material, the already reinforced polymer is usually supplied prefabricated by the manufacturer in the form of pellets. During injection molding, the fibers in the molten mass orient more or less strongly in

the flow, resulting in a generally anisotropic material behavior. A microscopic image of a SFRP is depicted in Fig. 4.2 (left). For a comprehensive overview of manufacturing processes, please refer to, for example [93], [104] or [142].

4.2.1 Polymer matrix materials

Following [104], the matrix of the composite has the following roles: "(1) to keep the fibers in place, (2) to transfer stresses between the fibers, (3) to provide a barrier against an adverse environment, such as chemicals and moisture, and (4) to protect the surface of the fibers from mechanical degradation (e.g., by abrasion)". The polymer matrix plays a major role in the transfer of mechanical loads in the transverse fiber direction and has a great influence on the shear strength of the composite. It also prevents the fibers from buckling under compressive load. Polymers can be distinguished between two broad classes: Thermoplastics and thermosets. In thermoplastics, the individual molecules are not chemically bonded to each other. Only weak intermolecular forces are acting between the molecular chains. A distinction must also be made here between amorphous and semi-crystalline thermoplastics. While the molecular chains of amorphous thermoplastics are disordered, semi-crystalline polymers show domains with a regular arrangement of these chains. When exposed to heat, these chains dissolve and the polymer can be deformed. When cooling down, the molecular chains remain in their new configuration. Therefore, thermoplastics can be melted down and reshaped as often as desired. An important term to describe the temperature-dependent behavior is the glass transition temperature, denoted as T_g. Below T_g the energy-elastic range is present, where brittle behavior can be observed to some extent. Approaching T_g, a softening of the material, i.e., a decrease in stiffness can be observed. In the glass transition area, a pronounced creep behavior can be found. Moreover, the coefficient of thermal expansion and the damping increase. If the temperature is increased further, this behavior becomes even more pronounced until the polymer finally melts. Semi-crystalline plastics can also be used above T_g depending on their crystallinity. Commonly used thermoplastics include polyamides, polypropylene, polyethylene, and polybutylenterephthalat. An overview with some corresponding material properties can be found in Table 4.1. In contrast to thermoplastics, the molecules of thermosets are chemically bonded to each other, forming a cross-linked three-dimensional network. Therefore, thermosets cannot be deformed by heating after they have cured and exhibit better thermal stability and a lower tendency to creep. Thermosets are often used as matrix material in continuous fiber reinforced polymers. Examples of common thermoset materials are epoxy, polyester, and vinyl ester.

Table 4.1: Different polymer materials and their properties [162], [47], [104], [157], [31]

Polymer material	ρ	E	Tensile strength	ν	k
Units	g/cm^3	GPa	MPa	1	W/mK
Epoxy resin	1.20	3.4	90	0.35	0.17-0.21
Polyester resin	1.22	4.8	60	-	-
Vinyl ester resin	1.14	4.0	83	-	-
Polyamide 6.6	1.14	1.7	57	0.40	0.30
Polypropylene	0.90	1.3	37	0.40	0.18-0.24
Polyphenylene sulfide	1.36	3.3	82.7	-	0.30

4.2.2 Fiber materials

Due to their relatively high stiffness and strength, the fibers carry out a major part of the load-bearing function of composites. The most relevant fibers employed in polymer matrix composites are synthetic glass fibers, carbon fibers, and aramid fibers. Glass fibers are the most frequently used polymer reinforcements in technical applications, mainly due to their low cost. Two commonly used glass fiber types are E-glass and S-glass [104]. E-glass is the lower cost and most widely used variant. The types differ slightly in their chemical composition [140]. The raw materials for the production of glass fibers are silicon oxide as main ingredients and also parts of other oxides such as aluminum oxide and calcium oxide. These ingredients are melted at temperatures of about 1370 °C. The molten mass emerges from small diameter spinnerets and is pulled out at high speed into thin long filaments before being cooled. The filaments are then coated and, depending on the desired form of delivery, bonded into a strand, for example. Sometimes the coating contains an adhesive that provides a better bond with the matrix. Typical dimensions of discontinuous glass fibers are a diameter of 10 µm and a length of 200 µm and are also affected by the manufacturing process (e.g., injection molding). If even higher requirements are placed on the stiffness and strength of the composite, carbon fibers [29] can be considered as an alternative to glass fibers. Carbon fibers exhibit high electrical and thermal conductivities and show a more or less pronounced anisotropic material behavior. Due to their excellent stiffness-to-weight ratio, they are often used in aerospace, sports, and automotive applications. Natural fibers are increasingly gaining attention, especially from a sustainability perspective [44], [126]. The combination of different fiber types in a hybrid composite material has also been investigated, e.g., to toughen composite materials [176]. An overview of different fiber materials and their properties is given in Table 4.2. A comprehensive overview of other fiber types can be found, for example, in [142], [104]. The overall properties of the composite can be significantly affected by the selection of the fiber type, the fiber volume fraction, the fiber orientation, and the fiber length.

Table 4.2: Overview of different fiber materials and their properties [104]

Fiber material	ρ / (g/cm^3)	E / GPa	Tensile strength / GPa	ν
E-Glass	2.54	72.4	3.45	0.20
S-Glass	2.49	86.9	4.30	0.22
PAN Carbon	1.76	231	3.65	0.20
Kevlar	1.45	131	3.62	0.35
Boron	2.70	393	3.10	0.20
Aluminum oxide	3.90	380	3.10	-

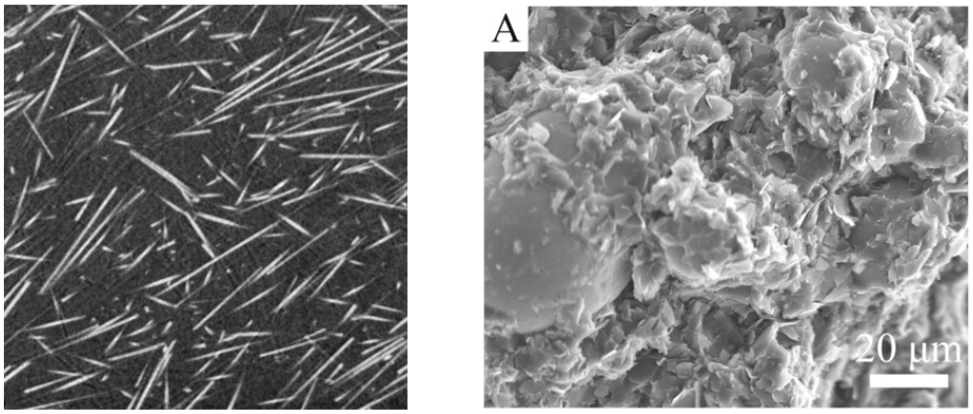

Figure 4.2: Microscopic image of a SFRP [40] (left) and a PRP [50] (right)

4.3 Thermally conductive polymer composites

In view of the current trend towards miniaturization of electrical devices, thermal management is of crucial importance [74]. Due to their electrical insulation, low density, easy moldability and low costs, plastics are a commonly used material for such applications, e.g., electronic packaging [137]. In this context, the main disadvantage of polymers is their intrinsic low thermal conductivity, typically in the narrow range of 0.1 - 0.5 W/mK. An overview of the thermal conductivities of common polymers is given in Table 4.1. The limited thermal conductivity of plastics can be considerably increased by adding thermally conductive fillers [118], [31]. The use of such functional materials can prevent thermal damage by improving heat dissipation, thus ensuring the performance and service life of electronic devices. There are many ceramic and mineral fillers available for this purpose [192]. In the context of this work, only electrically insulating particles are of interest, since electrical insulation is required in the considered applications. Examples of these fillers are aluminum oxide, magnesium oxide, aluminosilicate, aluminum nitride,

Table 4.3: Different thermally conductive fillers and their thermal conductivities [31]

Filler material	k / (W/mK)
Aluminum oxide	30
Silicon nitride	103-200
Aluminum nitride	100-300
Boron nitride	185-300

silicon carbide and boron nitride [71]. Some of them are listed in Table 4.3 with their associated thermal conductivity. The particles are available in various sizes and geometrical shapes. Apart from spherical particles, there are also platelet-shaped particles that can be used to achieve anisotropic thermal conductivity dependent on their distribution during the manufacturing process. A microscopic image of a PRP is shown in Fig. 4.2 (right). If electrical insulation is not required or if electrical conductivity is even to be achieved, metallic or carbonaceous fillers are also conceivable. In general quite high filling levels are necessary to achieve technically relevant conductivities. At low filler levels, the conductivity of the matrix is crucial. The heat transfer in polymers is essentially caused by phonon transport [58]. In this case, the matrix separates the highly conductive fillers and acts as a kind of thermal barrier. With increasing filling level, the formation of a percolation network can be observed at some point. This is characterized by the fact that there are heat conduction paths which solely lead through the highly conductive particles. In this case, a significant increase in conductivity can be observed [98]. When platelet-shaped particles with a high aspect ratio are used, the formation of such a network can be observed even at lower filling levels compared to spherical particles. However, the realization of such high filling levels is problematic for two main reasons. On the one hand, it should be noted that highly conductive fillers are relatively expensive, so that efforts are made to keep the fraction quite low. On the other hand, high filler contents are also problematic because the compound is quite difficult to process. For example, the melt has a very high viscosity, which encourages mold wear during injection molding. Such highly filled polymers are also often quite stiff and exhibit low failure strain and low impact strength. Therefore, the choice of filler and filler fraction is always a compromise between thermal conductivity, processability, mechanical properties, and costs. Finally, the ETC of a composite is based on a complex relationship between many different parameters such as the filling level [201], the thermal conductivity of the individual constituents, the shape and size of the particles [191], [203], the interfacial thermal resistance [150], [73], surface treatment [195], [188], and the spatial distribution (including the contact area between phases). A comprehensive overview of such different influencing factors can be found in [31]. This article also addresses some recent advances in the realization of microstructures for high conductivities.

Chapter 5

Optimization of effective material properties

In this chapter, the surrogate-based multiscale optimization method proposed in Chapter 3 is demonstrated by means of specific material examples. The optimization of thermomechanical material properties is presented on the basis of a three-phase PRP. In Section 5.1, the optimization framework is used to find different design variants of this material with a desired thermal conductivity. Subsequently, the method is extended to linear viscoelastic properties of SFRPs (Section 5.2). The overall consideration of effective thermomechanical properties by multiobjective optimization techniques is discussed in Section 5.3. It is shown how robust design methods can be used to account for uncertainties that arise during manufacturing or due to deviating material parameters. The surrogate-based optimization approach enables an efficient design of functional composites considering multiphysical and anisotropic requirements imposed on material properties especially in electromobility applications. In combination with advanced manufacturing techniques, the method offers great application potential within the product development process.

5.1 Optimization of the thermal conductivity of a three-phase PRP

In this first example, the optimization of the thermal conductivity of an electrically insulating three-phase PRP is considered. More precisley, the target is to find different variants of this materials with a desired thermal conductivity. This allows a selection of those variants that are the easiest to manufacture. Beside the application of the surrogate-based optimization framework, it is shown that the use of the EGO algorithm is an attractive alternative with view of the computational effort. Furthermore, the application of a gradient-based method with adjusted step size to handle stochastic effects is demonstrated. In particular, advantages and disadvantages of the different optimization methods and other aspects such as efficiency are discussed. It turns out that the proposed methodology allows an efficient detection of different design variants accounting for different microstructural parameters, such as phase fractions and aspect ratio and their influence on the overall thermal conductivity.

5.1.1 Material description

Motivated by the research conducted in [157] and [72], a three-phase composite consisting of a polybutylenterephthalat (PBT) matrix filled with two fillers of different geometries and large contrast in conductivities is investigated. In these studies, significantly larger conductivities in the range of 2 - 5 W/mK were obtained compared to neat polymers. As the interest is in the design of a dielectric polymer, only electrically insulating particles are examined. As fillers, low-conductive spherical aluminum oxide and high-conductive flaky boron nitride particles are studied. A microscopic image of such filler particles is shown in Fig. 5.1. The use of a second filler of low-conductive spherical particles is mainly motivated by an improvement of the flow properties at large filler contents and an reduction of costs, although the ETC is not significantly reduced compared to the exclusive use of flaky (expensive) particles. The thermal conductivities of the constituents are assumed to be isotropic and are listed in Table 5.1.

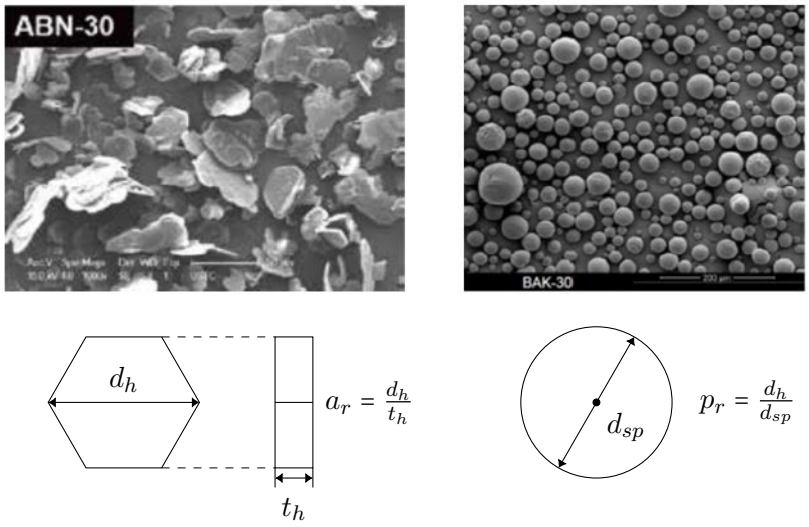

Figure 5.1: Microscopic image of flaky boron nitride (left) and spherical aluminum oxide particles (right) [163] and idealized (parameterized) geometries

Table 5.1: Thermal conductivities of the individual constituents

Phase index p	Material	k_p / (W/mK)
1	PBT	0.23
2	Aluminum oxide	30
3	Boron nitride	400

5.1.2 Optimization approach

To optimize the three-phase PRP to a desired ETC, the following minimization problem for the design variables $\boldsymbol{d}$ is formulated:

$$J(\boldsymbol{d}) = \left(\frac{\left\| \boldsymbol{k}_{\text{eff}}(\boldsymbol{d}) - \boldsymbol{k}^{*}_{\text{eff}} \right\|_2}{\left\| \boldsymbol{k}^{*}_{\text{eff}} \right\|_2} \right)^2 \rightarrow \min \qquad \text{s. t.} \quad d_{i,low} \leq d_i \leq d_{i,up}. \tag{5.1}$$

In (5.1), $\boldsymbol{k}_{\text{eff}} = \boldsymbol{k}_{\text{eff}}(\boldsymbol{d})$ is the macroscopic thermal conductivity tensor as a function of the design variables $\boldsymbol{d}$ and $\boldsymbol{k}^{*}_{\text{eff}}$ is the target ETC tensor. The target ETC tensor can be derived on the basis of a specific application (e.g., in power electronics) so that sufficient heat is dissipated and thermal damage is avoided. In this example, only descriptors of the geometrical microstructure are investigated as design variables. As mentioned in Section 4.3, it should be emphasized that the intrinsic thermal conductivity of the matrix has a significant influence on the ETC, especially for low particle volume contents. However, in practical applications one is often limited in the selection of the polymer matrix due to costs or for reasons of manufacturability. The consideration of material property descriptors of this three-phase PRP during optimization will be demonstrated in Section 5.3. In order to parametrize the geometry and size of the filler particles, the spherical particles are considered as perfect spheres and the flaky boron nitride particles are approximated by platelet-shaped particles with six edges (see Fig. 5.1). As design variables, the filler volume fraction V_f (including both filler fractions), the proportion of the platelet-shaped boron nitride particles δ_{bn}, the thickness of the platelet-shaped particles t_h, the mean aspect ratio a_r, and the mean particle size ratio p_r are selected. The aspect ratio is defined as the ratio of the diameter d_h to the thickness t_h of the platelet-shaped particles. The particle size ratio p_r results from the ratio of the diameter of the platelet-shaped particles d_h to the diameter of the spherical particles d_{sp}. The feasible set is listed in Table 5.2 and was chosen such that fillers available from material manufacturers can be taken into account. For both fillers, a Gaussian distribution of the particle diameters with a standard deviation of 16.66 % within a range of 33.33 % of the mean particle diameters (only particle diameters within these bounds are considered) is specified. In the following, the material optimization framework proposed in Chapter 3 is used for the solution of the material optimization problem (5.1). To be able to draw a comparison with other optimization techniques, the use of the EGO algorithm and a gradient-based optimizer is demonstrated. Advantages and disadvantages with respect to their use for engineering applications are discussed.

Table 5.2: Design variables with lower- and upper bounds

Index i	Design variable d_i	Lower bound $d_{i,low}$	Upper bound $d_{i,up}$
1	V_f / %	0	34
2	δ_{bn} / %	0	75
3	t_h / µm	4	6
4	a_r	4	8
5	p_r	2	4

Design of experiments

For the exploration of the material design space, 60 LH samples are selected. In Fig. 5.2, the sample distribution in the filler volume fraction-proportion boron nitride and in the filler volume fraction-aspect ratio space are illustrated. Due to the space-filling properties of the LH scheme, a quite good distribution of the samples within the entire design spaces can be observed. Each sample represents the realization of a specific microstructural configuration for which an RVE is generated. Based on these RVEs, the macroscopic thermal conductivity is determined by numerical homogenization. These steps are described in more detail in the following.

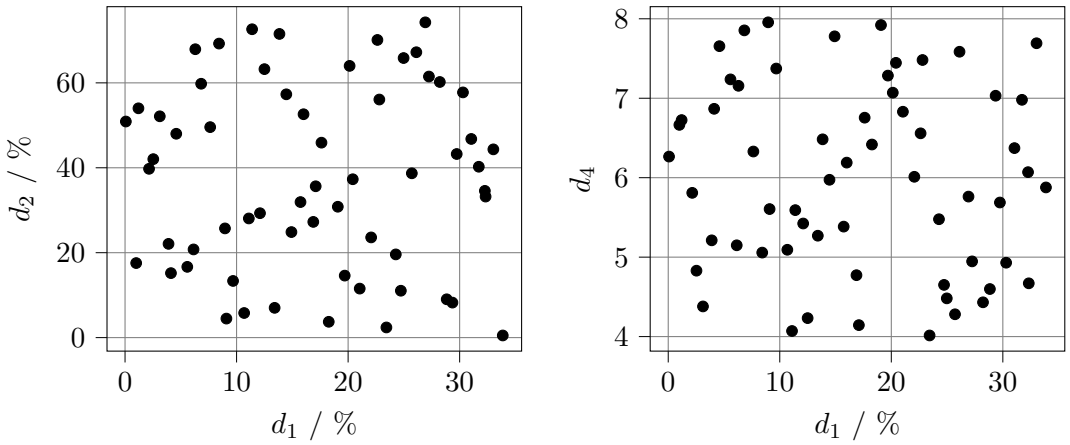

Figure 5.2: Distribution of the LH samples in the $d_1 - d_2$ (left) and $d_1 - d_4$ space (right)

Microstructure generation

Based on the experimental designs specified by the LH scheme, cubic RVEs with voxel length (resolution) h and edge length l (l = no. of voxels $\cdot$ h) are generated. A uniform particle distribution and an isotropic orientation of the filler particles within the matrix

is specified. The generation of the RVEs of the three-phase PRP is performed according to the announcements in Section 3.4. The stochastic distribution of the fillers within the matrix is controlled by the random seed, which allows the generation of different random RVEs. When touching particles are considered, it can be observed that the voxel length h has a strong influence on the ETC due to the large contrast in the conductivities of matrix and fillers. In order to obtain a resolution independent solution, only isolated (non-touching) particles are considered in that example. When carrying out examinations in which the filler volume fraction is increased (and setting the remaining design variables to their upper bounds), it can be observed that most of the contacts can be avoided until a filler volume fraction of $V_f = 34\%$. Following that, the upper bound of the filler volume fraction $d_{1,up}$ will be limited to that value. If contacts are still present, they are removed in a post-processing step by assigning the properties of the contact voxel to the conductivity of the matrix material. In Fig. 5.4, the realization of a RVE of the three-phase PRP with specified upper bounds of the design variables is depicted.

Computation of the ETC

Since in the considered example, relatively large filler levels and a large contrast in the conductivities of the individual constituents are investigated, the use of analytic methods for the computation of the ETC appears to be insufficiently accurate. Moreover, most of these approximation methods do not consider filler size effects, e.g., the influence of the aspect ratio a_r. For these reasons, the ETC is computed by numerical homogenization according to Section 3.5.5. The RVE domain $\omega = (0, l)^3 \subset \mathbb{R}^3$ of the three-phase composite consists of three subdomains (phases p) ω_p ($p = 1, 2, 3$). In each subdomain, the thermal conductivity tensor $\boldsymbol{k}(\boldsymbol{x})$ is assumed to be isotropic and constant (spatialy and temperature-independent), thus it can be expressed as a scalar value $k(\boldsymbol{x}) = k_p$ if $\boldsymbol{x} \in \omega_p$, where k_p is the thermal conductivity of phase p (see Table 5.1). The contacts between the matrix and the fillers are assumed to be perfect (no thermal resistance occurs at the interface). Please note that imperfect contacts can be taken into account in ConductoDict [15] by the specification of thermal contact resistances between the individual phases. If the particles are distributed perfectly isotropic and uniformly within the matrix, this results in an isotropic ETC tensor and the overall conductivity can be computed by solving a single BVP. To account for the influence of the statistical particle distribution and imprecise geometry generation, the full ETC tensor is computed, so the heterogeneities in all three space-dimensions are considered. In the following, the ETC tensor in (5.1) will be reduced to a scalar value $k_{\text{eff}}{=}k_{\text{eff}}(\boldsymbol{d})$, which will be determined from the mean value of the main diagonal components of the ETC tensor, i.e., $k_{\text{eff}} = \frac{1}{3}\text{tr}(\boldsymbol{k}_{\text{eff}}(\boldsymbol{d}))$. To compute the ETC tensor, the local temperature and heat flux fields are computed by solving the BVPs as described in Section 3.5.5. Periodic BCs with a prescribed macroscopic temperature gradient of $\nabla T = (294.15 - 293.15)\ \text{K}/l$ are applied. In Fig. 5.3, the absolute value of the heat flux and the temperature (within

the matrix) within an RVE with an edge length of $l = 450$ µm generated with the upper bounds of the design variables and the specification of the temperature gradient in x_3-direction is illustrated. The pronounced heterogeneity of the structure leads to strong fluctuations in the temperature field. Due to the large thermal conductivity and aspect ratio of the platelet-shaped particles, the greatest heat flux within the RVE is located in these particles. If the RVE is large enough, similar fluctuation fields in the individual space directions are generated and it seems sufficient to plot the heterogeneities for a single load case. The selection of a sufficient size of the RVE is elaborated on below.

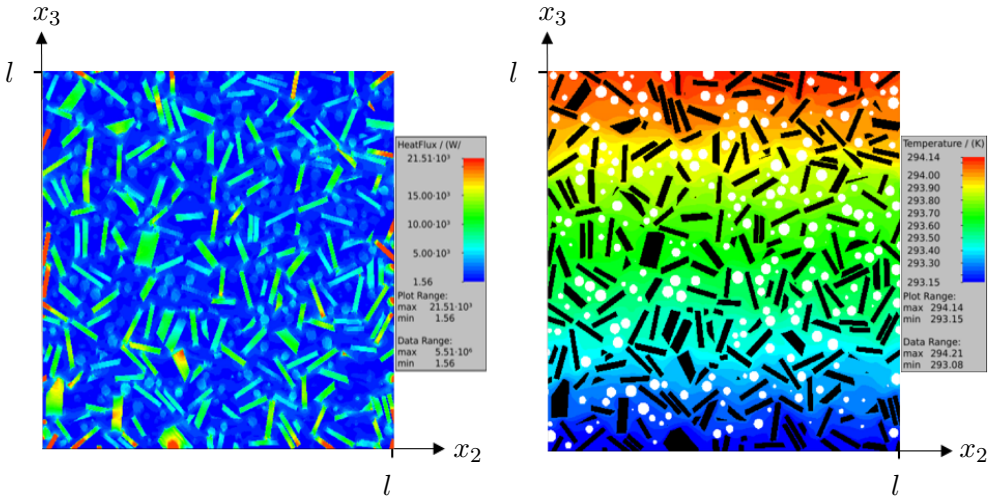

Figure 5.3: Heat flux (abslolute value, left) and temperature (right) within an RVE for prescribed periodic BCs under specification of a temperature gradient in x_3-direction

RVE convergence study

A representativeness study according to Section 3.5.7 is conducted to ensure a sufficiently accurate computation of the ETC for each experimental design specified by the LH scheme. The edge length l of the cubic RVEs is increased gradually, starting with 200 µm. A smaller edge length is not considered, because for lower edge lengths it can be observed that the specified microstructure cannot be realized with efficient accuracy (e.g., due to slight deviations in the filler level or in the phase proportions). The extreme case of setting all design variables to their upper bounds is investigated. Fig. 5.4 shows k_{eff} with an ensemble size of $N = 4$ according to (3.26) as a function of the edge length for a voxel length of 1 µm. For $\epsilon_{vol} = 3 \cdot 10^{-2}$, criterion (3.28) is fulfilled for an edge length of $l = 400$ µm (comparing the edge lengths of 400 and 500 µm). Since the specification of the upper bounds of the design variables can be regarded as a worst-case consideration for determining the size of the RVE, in the following an edge length of

$l = 450$ µm seems sufficiently accurate and each sample assigned RVE will be generated with this edge length. For this edge length, the standard deviation according to (3.27) is $6.89 \cdot 10^{-3}$ W/mK, which means that the statistical influence is quite small. After a sufficient RVE size has been determined, the influence of the resolution of the RVE on the homogenization results is investigated. For this purpose, the resolution of the structure with the voxel length of 1 µm (edge length of 450 µm) is refined by the factor of 2 and criterion (3.29) is examined. It can be observed that the difference in the ETC due to the refinement is less than 1 %. That means from a practical point of view that the ETC is independent of the resolution of the RVE and a finer resolution has no influence on k_{eff}. Based on the results of these investigations, each microstructural design specified by the LH scheme will be generated with an edge length of 450 µm and a voxel length of 1 µm, so the resulting structures consist of $450 \times 450 \times 450$ voxels.

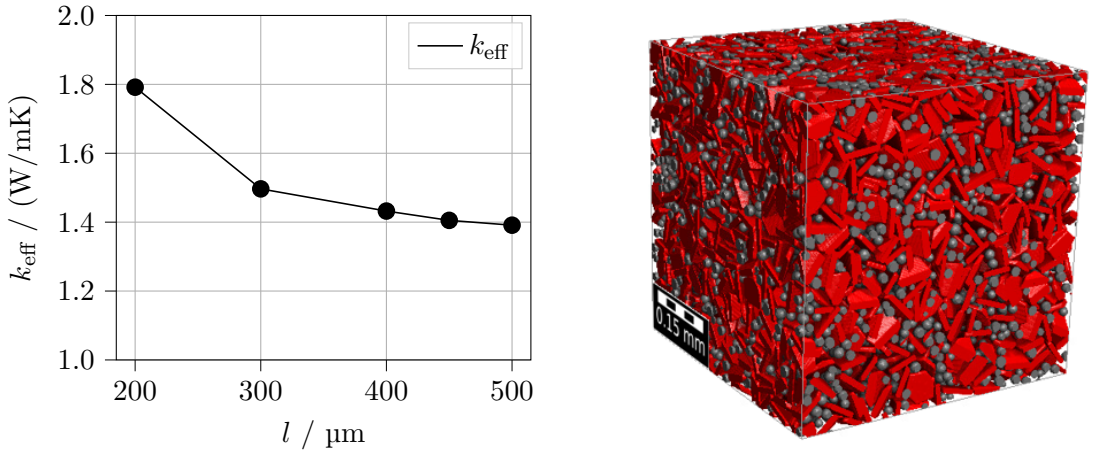

Figure 5.4: k_{eff} as a function of the edge length l and realization of an RVE of the three-phase PRP

Surrogate modeling

In order to model the k_{eff} as a function of the design variables $\boldsymbol{d}$, two types of surrogate models, second-order polynomials (RSM according to Section 3.6.1) and Kriging models (see Section 3.6.2) are investigated and compared with each other in terms of their prediction capabilities. Both surrogate models are trained by k-fold CV with $k = 5$. In each training step, the surrogates are constructed with $k - 1$ sets and the remaining test set is used to estimate the accuracy of the surrogate model. For that purpose, the coefficient of determination R^2 (3.49) and the e_{MAE} (3.46) are considered as error measures. The error measures were calculated in each of the 5 training steps and the mean values for both surrogate types are listed in Table 5.3. It can be observed that both the

second-order polynomials and the Kriging model can predict the ETC with high accuracy with R^2 scores very close to 1. Fig. 5.5 shows a comparison of the ETCs predicted by the surrogates (from the test data set where the largest e_{MAE} occurs) with the results of the micromechanical simulations. The Kriging model shows the best accuracy with e_{MAE} = 0.0048 W/mK. The predictions from the metamodel and the simulation results differ only slightly with a maximum error of 3.8 % (0.892 W/mK (Kriging interpolation) / 0.927 W/mK (simulation)). Based on these observations, in the following the Kriging model trained with all 60 samples is utilized for the solution of the material optimization problem.

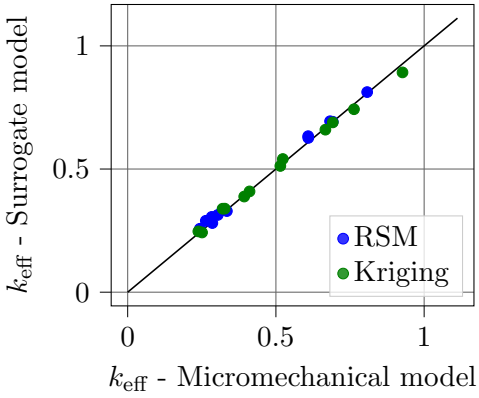

Figure 5.5: Comparison of predictions from the simulation model and the surrogate model

Model	R^2	e_{MAE} / (W/mK)
RSM	0.994	0.0106
Kriging	0.998	0.0048

Table 5.3: R^2 and e_{MAE} for the RSM and Kriging surrogate

Fig. 5.6 shows the ETC as a function of the filler volume fraction and the phase proportions (left) as well as the filler volume fraction and the aspect ratio (right) by setting the remaining design variables to their upper bound values. As expected, the filler volume fraction shows a great influence on the ETC. However, the influence of the mean aspect ratio a_r and the phase proportions δ_{bn} can also be clearly observed, especially for larger volume fractions.

Global sensitivity analysis

In order to quantitatively determine the impact of the different design variables on the ETC, a global sensitivity analysis is conducted. In this way, the most important parameters influencing the ETC can be detected and the dimension of the design space for optimization can be reduced if non-sensitive parameters are present. For this purpose, first-order and total-order Sobol' indices are computed using the Kriging surrogate representation with 2^{16} samples according to Section 3.7.1. Table 5.4 lists both indices

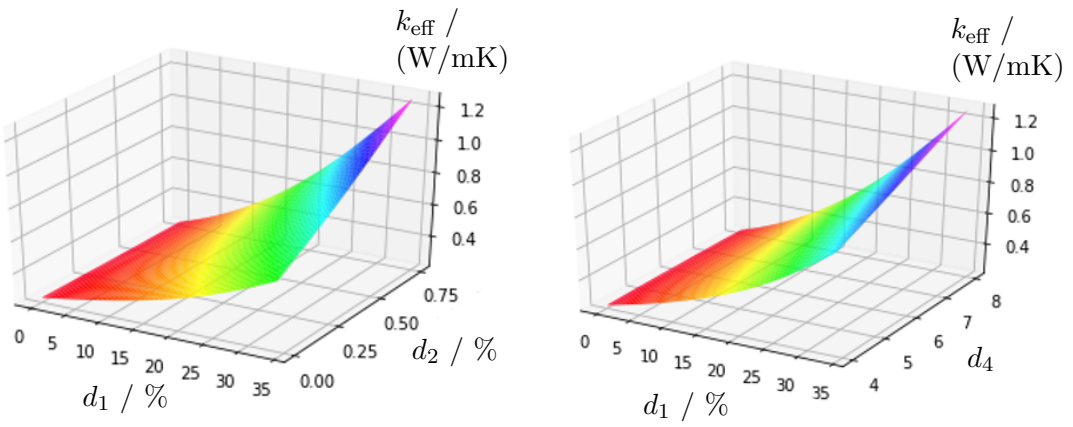

Figure 5.6: Kriging interpolation of k_{eff} as a function of d_1 and d_2 (left), and d_1 and d_4 (right)

S_i and S_{T_i} of all five design variables. The filler level is by far the most sensitive parameter, followed by the proportion of the individual phases and the mean aspect ratio. The thickness of the platelet-shaped particles and the mean particle ratio can be regarded as negligible with $S_{T_i} \leq 10^{-3}$. The comparison of first- and total-order Sobol' indices allows to detect interactions between the individual design variables. When examining the second-order indices, it can be observed that there is an interaction between d_1 and d_2 with $S_{12} = 0.0415$, d_1 and d_4 with $S_{14} = 0.0089$ as well as d_2 and d_4 with $S_{24} = 0.0051$.

Table 5.4: Sobol' indices of the individual design variables

Index i	Design variable d_i	S_i	S_{T_i}
1	V_f / %	$8.56 \cdot 10^{-1}$	$9.10 \cdot 10^{-1}$
2	δ_{bn} / %	$7.06 \cdot 10^{-2}$	$1.20 \cdot 10^{-1}$
3	t_h / µm	$3.16 \cdot 10^{-4}$	$7.76 \cdot 10^{-4}$
4	a_r	$1.43 \cdot 10^{-2}$	$3.12 \cdot 10^{-2}$
5	p_r	$4.76 \cdot 10^{-5}$	$7.54 \cdot 10^{-5}$

Optimization and identification of different design variants

Based on the results of the sensitivity analysis, design variables with $S_{T_i} \leq 10^{-3}$ will be neglected during optimization. This means that the thickness of the platelet-shaped particles t_h and the mean particle ratio p_r are neglected and the design space reduces to three dimensions (V_f, δ_{bn}, and a_r). The DE algorithm according to Section 3.8.4 implemented in the Python library SciPy [185] is used for the solution of the optimization problem (5.1). A population size of $N_p = 75$ is chosen. The initial population is uniformly distributed within the design space by LHS. The DE/best/1/bin strategy is

employed. A crossover probability P_{cross} of 0.7 is selected. The mutation constant F is chosen to be in the range between 0.5 and 1 employing dithering. The use of such population-based methods offer the advantage of providing more design candidates by exploring promising areas of the design space. As stated in Section 3.2, this goes along with a lot of function evaluations, but as the optimization is performed on the surrogate, this does not limit the use of such methods. Since various realization options for a target ETC are to be found, several runs with DE are carried out. Table 5.5 shows a set of four different realization options that were determined on the surrogate representation of k_{eff} in the three-dimensional design space for $k^*_{\text{eff}} = 0.75$ W/mK by four optimization calls. The neglected design variables were set to their mid range values (see Table 5.2). Due to the aforementioned nature of DE, an alternative way to identify different design variants is provided by considering the iteration history of the individual populations and select only those variants that exhibit an acceptable deviation from the target value.

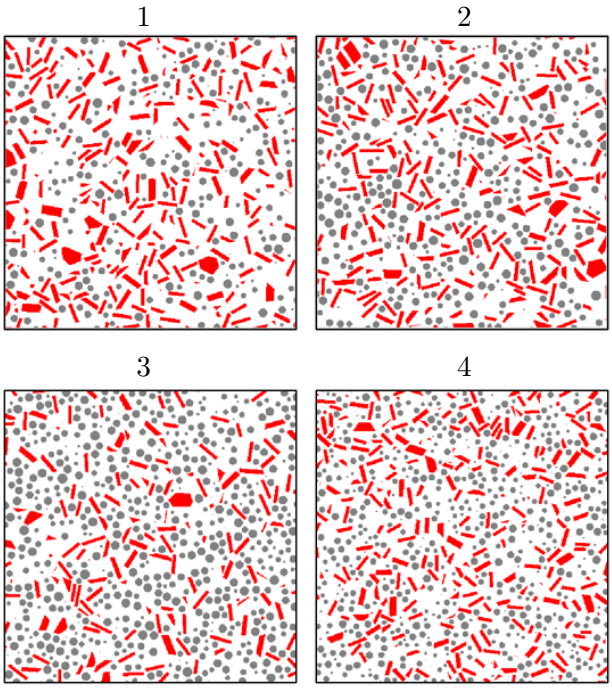

Figure 5.7: Set of four "optimal" microstructural designs

Since the optimization results were obtained by the surrogate representation of the optimization problem, an additional solver run is performed to determine $k_{\text{eff}}(\boldsymbol{d}^*)$ for each optimum utilizing the micromechanical model. When evaluating the simulation model, only minor deviations of a maximum of 2.667 % for the second design variant can be

observed. Fig. 5.7 shows sectional views of the corresponding RVEs. The choice of different realizations allows to select those variants that can be produced most easily.

Table 5.5: Approximation of optimal microstructural realizations and validation through the evaluation of the micromechanical model

Design no.	d_1^*	d_2^*	d_4^*	$J(\boldsymbol{d}_{\text{red}}^*)$	$k_{\text{eff}}(\boldsymbol{d}^*)$	Deviation
Units	%	%	1	1	W/mK	%
1	24.813	0.689	6.711	0	0.744	0.800
2	28.077	0.496	7.166	0	0.770	2.667
3	31.157	0.319	7.003	0	0.743	0.930
4	29.633	0.526	5.780	0	0.755	0.667

Efficient global optimization (EGO)

In applying the surrogate-based optimization approach, a total number of 60 samples was used to create a surrogate model that represents the entire material design space sufficiently accurately. In general, one is interested in finding a global optimum of an optimization problem with as few as possible costs (numerical effort). The EGO algorithm seems to be a suitable method for such optimization tasks, since it operates on the basis of a relatively small number of samples for the creation of an initial Kriging surrogate and then attempts to locate the next sampling points towards the global optimum by optimizing and aquisition function. In the following, the EGO algorithm as described in Section 3.8.5 is applied for the solution of the optimization problem (5.1). For the creation of the initial Kriging surrogate, 6 LH samples are specified and a fix number of 20 iterations are set to quantify the performance of the method. As acquisition functions, the expected improvement (EI) (3.73) and the lower confidence bound (LCB) (3.74) are investigated. Fig. 5.8 shows $k_{\text{eff}}(\boldsymbol{d})$ as a function of the iterations for k_{eff}^*=0.75 W/mK (red dashed line). The initial samples are shown as black dots and the samples evaluated on the basis of the infill criterias are illustrated as green dots. It can be observed that structures with almost the desired ETC are identified after only a few iterations. The EI criterion shows a slightly better performance in that example. During the optimization process, a deterioration of the design objective (deviation of k_{eff}^*) can be observed to some extent. This is due to the exploration term of the acquisition functions, where samples are added in areas of the design space where the model exhibits a large prediction variance. Table 5.6 and 5.7 list the corresponding values of the design variables for the three best identified designs (measured by the deviation from the target conductivity) using the EI and the LCB criterion, respectively. The best design variant is identified by the LCB criterion after 16 iterations.

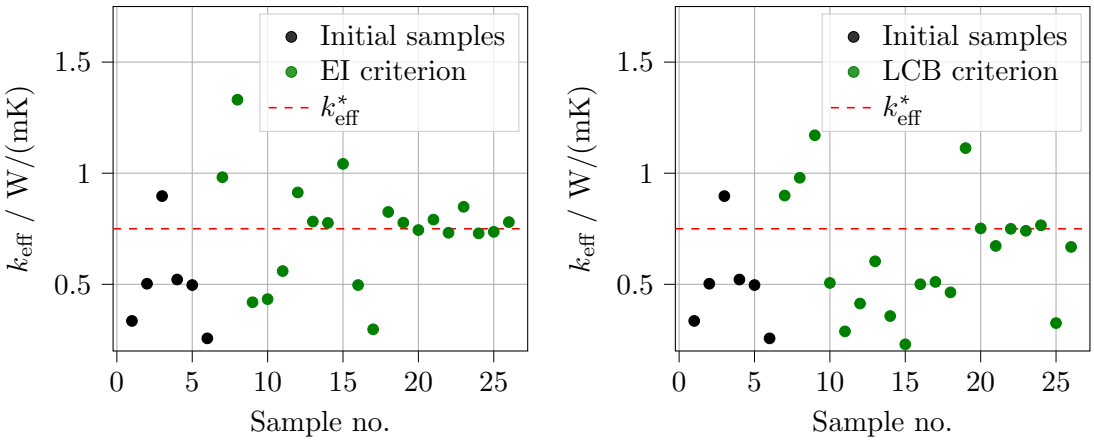

Figure 5.8: k_{eff} for the initial samples and as a function of the number of iterations of the EGO algorithm by using the EI (left) and the LCB criterion (right)

Table 5.6: Best microstructural realizations identified by the EI criterion

Iteration no.	d_1	d_2	d_3	d_4	d_5	$k_{\text{eff}}(\boldsymbol{d})$	Deviation
Units	%	%	µm	1	1	W/mK	%
14	31.92	0.32	5.60	6.30	3.78	0.744	0.8
16	27.05	0.65	6.00	5.34	3.89	0.732	2.4
19	30.15	0.34	4.00	7.54	2.26	0.736	1.9

Table 5.7: Best microstructural realizations identified by the LCB criterion

Iteration no.	d_1	d_2	d_3	d_4	d_5	$k_{\text{eff}}(\boldsymbol{d})$	Deviation
Units	%	%	µm	1	1	W/mK	%
14	34.00	0.38	5.98	4.00	2.00	0.752	0.3
16	34.00	0.12	6.00	8.00	2.24	0.750	0.0
18	21.66	0.75	6.00	8.00	2.00	0.766	2.1

Sequential quadratic programming (SQP)

In the following, it shall be demonstrated exemplarily how the difficulties resulting from the stochastic behavior of the objective function can be handled when applying a gradient-based optimization method. The sequential quadratic programming (SQP) method implemented in the Python scientific library SciPy [185] (named SLSQP) is considered. Since no analytical expression for the gradients is available, the FD method is used to approximate the gradients. The forward differential quotient D_f defined as

$$\frac{\partial J(\boldsymbol{d}^l)}{\partial d_i} \approx \frac{J(\boldsymbol{d}^l + h \cdot e_i) - J(\boldsymbol{d}^l)}{h} = D_{f_i} \tag{5.2}$$

is considered for this purpose. To prevent the method from converging in a local optimum caused by the stochastic nature of the numerical RVEs, an adjusted step size h must be selected for the computation of D_{f_i}. The step size should be chosen as small as possible to approximate the gradients as closley as possible. However, the randomness of the structure and small deviations in the geometrical microstructure from the specification should not lead to a falsification of the gradient info. For that purpose, the design variables are scaled ranging from 0 (lower bound) to 1 (upper bound). A step size of $h = 5 \cdot 10^{-3}$ is selected for the approximation of the gradients by D_{f_i}. For the computation of the gradients, $n+1$ ($n = 5$) simulations must be carried out. Central differences and local averaging methods can be used to improve the approximation quality of the gradients. There are special methods to handle such noisy optimization problems, see, e.g., [174]. However, it is obvious that this involves a large number of solver evaluations, so these methods are not further investigated in this work. In the following example, the initial values are specified as the mid range values of the design variables. A RVE size of 450 µm is considered for the computation of the ETC and only a single statistical realization is investigated. As termination criterion, a tolerance of $5 \cdot 10^{-4}$ is chosen. With these parameters, the algorithm terminates after 4 iterations and a total number of 30 function evaluations. The optimum is determined as $J(\boldsymbol{d}^*) = 1.26 \cdot 10^{-5}$ with $\boldsymbol{d}^* = (30.35,\ 0.545,\ 5.23 \cdot 10^{-6},\ 5.05,\ 2.40)$.

Comparison of the optimization methods

The purpose of this subsection is to compare the optimization methods used to solve the optimization problem (5.1). The surrogate-based optimization approach enables the application of population-based optimization methods due to the fast evaluability of the structural response. By application of the DE method, it was demonstrated that different design variants can be identified. A validation of these optima obtained the surrogate model by evaluating the numerical model revealed only minor deviations. In applying EGO, a surrogate model was generated with a very limited number of samples. It turned out that almost optimal designs could be determined after just a few iterations. The EI criterion performed slightly better compared to the LCB criterion. In view of the numerical effort this represents an attractive method. However, it is well known that EGO is not efficient in some cases, especially for high-dimensional design spaces. By applying a gradient-based method, the oscillations of the objective function could be controlled by normalizing the design variables and selecting a sufficiently large step size. However, there is a risk of getting trapped in such a local optimum if the step size for calculating the FD is choosen too small. One way to reduce the influence of such stochastic effects might be the use of larger RVEs. This must be considered separately in each

application. If different design variants are of interest or if changing target values should be considered, gradient-based method would need different optimization runs which is connected with an renewed evaluation of the numerical model. Furthermore, it is in general not known, if the found optimum is a global one. To overcome that, for example a multi-start strategy can be adopted. The comparison demonstrate the advantages of the proposed approach in comparison with other common used optimization techniques for the solution of nonlinear structural optimization problems. However, the selection of an appropriate method depends on the example considered and has to be chosen carefully from case to case. A remarkable advantage of the surrogate model is that it allows an understanding of the relationship of the ETC in dependence of the design variables. If the samples can be evaluated in parallel, this allows an faster construction of the surrogate model.

5.1.3 Experimental validation

In order to validate the numerical homogenization method, simulation results are compared with corresponding measurements. In deviation from the previous considerations, silicone (k = 0.18 W/mK) is considered as matrix material in the following for reasons of limited manufacturing possibilities. Material specimens consisting of the silicone matrix doped with spherical aluminum oxide particles with an mean diameter of 15 µm and flaky boron nitride particles with a mean diameter of 25 µm were produced. The specimens were prepared in a vacuum by Speedmixer DAC 600.1 FVZ and two specimens with a filler volume fraction of 33.16 % and 40 % were analyzed. To account for stochastic influences, the measurements were repeated five times with newly prepared specimens. The bulk ETC was measured indirectly with the stationary cylinder method according to ASTM D5470-12 [10] by TIM Tester from ZfW Stuttgart. For the simulation, cubic RVEs with an edge length of 200 µm and a voxel length of 250 nm ($800\times800\times800$) voxels and 125 nm ($1600\times1600\times1600$) voxels are generated and the particles were allowed to touch each other. The thermal conductivities of the individual constituents were selected according to Table 5.1. As in the previous studies, perfect spherical and platelet-shaped particles with a uniform distribution and isotropic orientation are analyzed. The particle diameters distributions were specified according to the data sheet from the material supplier and the aspect ratio of the platelet-shaped particles is set to 5. As can be seen in Table 5.8 (No. 3 + 4), for a voxel length of 125 nm, this results in k_{sim} = 0.81 W/mK (simulation) and k_{meas} = 0.95 W/mK (measurement, mean value) for a particle volume fraction of 33.16 % and k_{sim} = 1.08 W/mK and k_{meas} = 1.04 W/mK for a particle volume fraction of 40 %. The values in the square brackets indicate the value range of the five measurements. The deviations may result from various uncertainties, such as discrepancies in the exact conductivities of the fillers, an non-uniform distribution of the fillers in the blend, the consideration of idealized particle geometries as well as measurement errors. As mentioned above, the influence of the voxel grid (with voxel length h) on the

approximation quality of the particle contact faces must also be taken into account. For that purpose, for the three-phase material (No. 3 + 4), the ETC computed with a voxel length of 250 nm is given additionally in Table 5.8. The reduction of the ETC by using a smaller voxel length results from a better approximation quality of the particle contact areas with a fine voxel grid (decreasing particle contact areas). Due to the enormous numerical effort, it was not possible to carry out simulations with a finer resolution of the structures ($h < 125$ nm). To reduce the influence of such uncertain parameters, further validation studies will be performed. For this purpose, two compounds are investigated in which only silicone filled with spherical alumina (mean diameter of 15 µm) is examined, taking into account filler volume fractions of 40 % and 50 %. In this case, the uncertainties mentioned are much less pronounced compared to the three-phase PRP. For that material, convergence of the ETC was achieved by an edge length of 200 µm and a voxel length of 0.25 µm (according to $\epsilon_{vol} = 2.5$ % and $\epsilon_{vol} = 1$ % in relation to a RVE with the half edge length respectively the double voxel length), so the influence of the particle contact faces is by far not as dominant as in the three-phase material example. As shown in Table 5.8, this results in $k_{\mathrm{sim}} = 0.76$ W/mK and $k_{\mathrm{meas}} = 0.79$ W/mK for a filler volume fraction of 40 % and $k_{\mathrm{sim}} = 1.07$ W/mK and $k_{\mathrm{meas}} = 1.18$ W/mK for a filler volume fraction of 50 % and differs less than 10 %. In analogy to the Voigt-Reuss bounds in elasticity, the lower and upper Wiener bounds (designated as k_{WLB} and k_{WUB}) are listed in Table 5.8. For comparison purposes a relative error

$$e_{\mathrm{rel}} = \frac{|k_{\mathrm{meas}} - k_{\mathrm{sim}}|}{k_{\mathrm{WUB}} - k_{\mathrm{WLB}}} \tag{5.3}$$

is introduced. Due to the large contrast in the conductivities (especially in No. 3 + 4), the relative error is quite small. These examples demonstrate the importance of thorough material characterization in combination with the application of suitable manufacturing techniques to realize the digital material.

Table 5.8: Validation of the homogenization results by comparison with corresponding measurements

No.	d_1	d_2	k_{meas}	k_{sim}	k_{WLB}	k_{WUB}	e_{rel}
Units	%	%	W/mK	W/mK	W/mK	W/mK	%
1	40	0	0.79	0.76	0.30	12.11	0.25
2	50	0	1.18	1.07	0.36	15.09	0.75
3	14.92	18.24	0.95 [0.91-0.98]	0.81 (0.89)	0.27	77.55	0.18
4	20	20	1.04 [0.99-1.11]	1.08 (1.25)	0.30	86.11	0.047

5.2 Optimization of the linear viscoelastic properties of SFRPs

In this section, the optimization framework is applied for the optimization of the effective viscoelastic behavior of SFRPs. In contrast to the previous example, in which an isotropic orientation of the filler particles was prescribed, arbitrary fiber orientation states should now be taken into account. This results in a generally anisotropic material behavior, which must be considered in the surrogate modeling process. Beside the fiber orientation distribution, the fiber volume fraction, and the linear elastic fiber material properties are specified as design variables. The aim is to find material designs with a desired viscoelastic behavior and to examine the robustness of these designs. A generalized Maxwell model is used to model the viscoelastic behavior of the polymer matrix. In the numerical homogenization step, creep simulations are performed on RVEs and the FFT-based homogenization method is employed to compute the associated microscopic solution fields. The optimizations results allow a consideration of the local microstructure during the manufacturing of SFRPs in order to achieve a desired macroscopic viscoelastic behavior of components.

5.2.1 Viscoelastic matrix material model and parameter identification

The viscoelastic behavior of SFRPs is almost completely governed by viscous effects of the polymer matrix. The constitutive behavior of the fibers is modeled as linear elastic. In the following, a generalized Maxwell model [83] is used to model the rate-dependent viscoelastic behavior of the polymer matrix. The generalized Maxwell model can be considered as a rheological model consisting of a spring connected in parallel with N spring-damper (Maxwell) elements as sketched in Fig. 5.9. The kth Maxwell element is described by the modulus E_k $(k = 1, ..., N)$ and the relaxation constant τ_k (alternatively expressed by the viscosity $\eta_k = E_k \cdot \tau_k$). In linear viscoelasticity, the stresses and strains are connected via a convolution integral, considering arbitrary strain histories by the superposition principle as follows:

$$\boldsymbol{\sigma}(t) = \int_0^t \boldsymbol{\Gamma}(t-s) : \frac{\partial \boldsymbol{\epsilon}(s)}{\partial s} \mathrm{d}s. \tag{5.4}$$

In (5.4), $\boldsymbol{\Gamma}$ describes a symmetric fourth-order relaxation tensor. For the generalized Maxwell model considered in the following, it is assumed that the relaxation tensor can be expressed in a normalized form as

$$\boldsymbol{\Gamma}(t) = \psi(t) \cdot \boldsymbol{C}^r \tag{5.5}$$

with the normalized relaxation function

$$\psi(t) = 1 + \sum_{k=1}^{N} \gamma_k \cdot \exp\left(-\frac{t}{\tau_k}\right) \tag{5.6}$$

including the normalized relaxation coefficients $\gamma_k = \frac{E_k}{E_0}$. For $t \to \infty$, $\mathbf{\Gamma}(t)$ tends to the relaxed stiffness tensor $\boldsymbol{C}^r$ and results in a pure linear elastic (relaxed) material described by a single spring element. A detailed description, including a discretized form of the viscoelasticity model, can be found in [83].

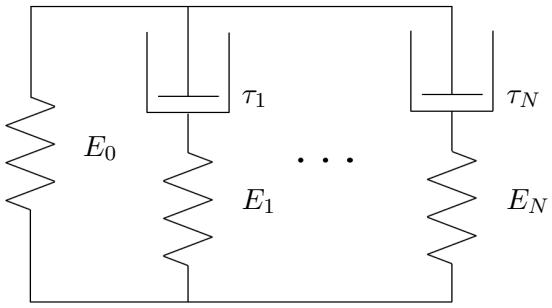

Figure 5.9: Principal sketch of the generalized Maxwell model

Element k	E_k / MPa	τ_k / s	γ_k
1	47.40	$1 \cdot 10^1$	0.095
2	15.00	$1 \cdot 10^2$	0.030
3	187.61	$1 \cdot 10^3$	0.376
4	197.39	$1 \cdot 10^4$	0.396
5	200.04	$1 \cdot 10^5$	0.401
6	200.30	$1 \cdot 10^6$	0.402
7	145.39	$1 \cdot 10^7$	0.292
8	99.91	$1 \cdot 10^8$	0.200
9	51.24	$1 \cdot 10^9$	0.103
10	20.35	$1 \cdot 10^{10}$	0.041

Table 5.9: Identified viscoelastic material parameter ($N = 10$) for PA 66

Polyamide (PA) 66 (Zytel 101) is investigated as polymer material, which is a commonly used material for technical applications. In [196] and [197], corresponding measurements including a master curve for this material are presented. To specify the viscoelastic behavior of the matrix material, the material parameters E_k and τ_k (respectively η_k) in (5.6) have to be determined. Following [99], a constant Poisson's ratio $\nu = 0.38$ is assumed for the isotropic polymer matrix. As a rule of thumb, according to [95] 10 Maxwell elements ($N = 10$, one for each time decade) are used to model the viscoelastic material behavior in the time intervall $t \in [0, 10^{10.7}]$ s. The relaxation constants τ_k are specified to be constant, see Table 5.9. Consequently, only 10 stiffness parameters E_k and E_0 have to be determined. For that purpose, the following least squares optimization problem is formulated:

$$J(E_0, E_1, ..., E_{10}) = \sum_{i=1}^{M} (\epsilon_{i,\text{model}}(E_0, E_1, ..., E_{10}) - \epsilon_{i,\text{exp}})^2 \to \min. \tag{5.7}$$

In (5.7), $M = 10$ strain values at each time decade $(10^1, 10^2, ..., 10^{10})$s are regarded. The bounds for the stiffness of the individual springs are set to $E_0 \in [0.2, 2]$ GPa and $E_k \in [0.015, 1]$ GPa for the remaining spring elements. For solving (5.7), the sequential quadratic programming (SQP) method implemented in the Python scientific library SciPy [185] is used. As start values, $E_0 = 0.5$ GPa and $E_k = 0.1$ GPa for the remaining spring elements are chosen. The optimum is calculated as $J^* = 3.84 \cdot 10^{-4}$, which

seems to be sufficiently accurate for engineering purposes. This results in a stiffness of $E_0 = 498.5$ MPa for the single spring element. The identified viscoelastic material parameter of the 10 Maxwell elements are summarized in Table 5.9.

5.2.2 Optimization approach

The overall (anisotropic) viscoelastic behavior of SFRPs can be expressed by the macroscopic creep compliance tensor (respectively the relaxation tensor), which is generally defined by 21 independent material parameters. In the following, the interaction between normal stresses and shear strains will be neglected. This means that the effective constitutive material behavior is treated as orthotropic. Further investigations show that the neglected parameters are quite small compared to these orthotropic parameters. Hence, the description of the effective viscoelastic behavior of SFRPs will be reduced in the following to the consideration of 9 time-dependent elastic constants. These parameters are comprised of three Young's moduli $E_{1,\mathrm{eff}}$, $E_{2,\mathrm{eff}}$, $E_{3,\mathrm{eff}}$, three shear moduli $G_{12,\mathrm{eff}}$, $G_{13,\mathrm{eff}}$, $G_{23,\mathrm{eff}}$, and three Poisson's ratios $\nu_{12,\mathrm{eff}}$, $\nu_{13,\mathrm{eff}}$, $\nu_{23,\mathrm{eff}}$ and can be identified in the Voigt notation of the creep compliance tensor as follows:

$$\boldsymbol{\Upsilon}_{\mathrm{eff}}(t) = \begin{bmatrix} \frac{1}{E_{1,\mathrm{eff}}(t)} & -\frac{\nu_{21,\mathrm{eff}}(t)}{E_{2,\mathrm{eff}}(t)} & -\frac{\nu_{31,\mathrm{eff}}(t)}{E_{3,\mathrm{eff}}(t)} & 0 & 0 & 0 \\ -\frac{\nu_{12,\mathrm{eff}}(t)}{E_{1,\mathrm{eff}}(t)} & \frac{1}{E_{2,\mathrm{eff}}(t)} & -\frac{\nu_{32,\mathrm{eff}}(t)}{E_{3,\mathrm{eff}}(t)} & 0 & 0 & 0 \\ -\frac{\nu_{13,\mathrm{eff}}(t)}{E_{1,\mathrm{eff}}(t)} & -\frac{\nu_{23,\mathrm{eff}}(t)}{E_{2,\mathrm{eff}}(t)} & \frac{1}{E_{3,\mathrm{eff}}(t)} & 0 & 0 & 0 \\ 0 & 0 & 0 & \frac{1}{G_{23,\mathrm{eff}}(t)} & 0 & 0 \\ 0 & 0 & 0 & 0 & \frac{1}{G_{13,\mathrm{eff}}(t)} & 0 \\ 0 & 0 & 0 & 0 & 0 & \frac{1}{G_{12,\mathrm{eff}}(t)} \end{bmatrix}. \tag{5.8}$$

Please note that $\boldsymbol{\Upsilon}_{\mathrm{eff}}$ is symmetric, i.e., $\Upsilon_{ij,\mathrm{eff}} = \Upsilon_{ji,\mathrm{eff}}$ $(i,j = 1,2,...,6)$. In order to find a microstructural design with a desired viscoelastic behavior, the following minimization problem for the design variables $\boldsymbol{d}$ is considered:

$$\begin{aligned} J(\boldsymbol{d}) = &\left(\frac{E_{1,\mathrm{eff}}(\boldsymbol{d}) - E^*_{1,\mathrm{eff}}}{E^*_{1,\mathrm{eff}}}\right)^2 + \left(\frac{E_{2,\mathrm{eff}}(\boldsymbol{d}) - E^*_{2,\mathrm{eff}}}{E^*_{2,\mathrm{eff}}}\right)^2 + \left(\frac{E_{3,\mathrm{eff}}(\boldsymbol{d}) - E^*_{3,\mathrm{eff}}}{E^*_{3,\mathrm{eff}}}\right)^2 + \\ &\left(\frac{G_{12,\mathrm{eff}}(\boldsymbol{d}) - G^*_{12,\mathrm{eff}}}{G^*_{12,\mathrm{eff}}}\right)^2 + \left(\frac{G_{13,\mathrm{eff}}(\boldsymbol{d}) - G^*_{13,\mathrm{eff}}}{G^*_{13,\mathrm{eff}}}\right)^2 + \left(\frac{G_{23,\mathrm{eff}}(\boldsymbol{d}) - G^*_{23,\mathrm{eff}}}{G^*_{23,\mathrm{eff}}}\right)^2 + \\ &\left(\frac{\nu_{12,\mathrm{eff}}(\boldsymbol{d}) - \nu^*_{12,\mathrm{eff}}}{\nu^*_{12,\mathrm{eff}}}\right)^2 + \left(\frac{\nu_{13,\mathrm{eff}}(\boldsymbol{d}) - \nu^*_{13,\mathrm{eff}}}{\nu^*_{13,\mathrm{eff}}}\right)^2 + \left(\frac{\nu_{23,\mathrm{eff}}(\boldsymbol{d}) - \nu^*_{23,\mathrm{eff}}}{\nu^*_{23,\mathrm{eff}}}\right)^2 \rightarrow \min \\ &\text{s. t.} \qquad d_{i,low} \leq d_i \leq d_{i,up}. \end{aligned} \tag{5.9}$$

Formulation (5.9) includes the 9 viscoelastic material parameters as a function of the design variables and the desired values. In the following, the design variables are defined that span the material design space for optimization. Both design variables of the geometrical microstructure and material property descriptors are taken into account. As design variables of the geometrical microstructure, the fiber volume fraction V_f and the fiber orientation distribution are investigated, which are recognized to have a significant influence on the overall mechanical (and viscoelastic) behavior. V_f ranges from 5-20 %, which is a commonly found range in most materials used for engineering applications. For the representation of the fiber orientation distribution state, the second-order symmetric Advani-Tucker tensor [4]

$$\boldsymbol{A} = \frac{1}{N} \sum_{i=1}^{N} \boldsymbol{p}_i \otimes \boldsymbol{p}_i \tag{5.10}$$

is investigated, in which $\boldsymbol{p_i}$ describes the normalized fiber direction vector of fiber i and N denotes the number of fibers. Please note that (5.10) is only valid for fibers with same length. It is obvious that the expression (5.10) does not provide a unique description of the fiber orientation distribution state, since the spatial distribution of the fibers is not fully covered. However, it is the common output of injection molding software and the larger the RVE considered, the less pronounced the influence of the spatial fiber distribution on the overall properties. An overview of measures for the fiber orientation distribution using higher-order moments can be found, e.g., in [115]. If $\boldsymbol{A}$ is the only available measure of the fiber distribution, some homogenization methods requires a closure approximation [115]. By making use of an eigenvalue decomposition (principal component analysis), $\boldsymbol{A}$ can be expressed in terms of an orthogonal rotation matrix $\boldsymbol{R}_{\text{rot}}$ defined by three Euler angels θ, γ, $\beta \in [0, \pi]$ and two independent parameters λ_1 and λ_2 as

$$\boldsymbol{A} = \boldsymbol{R}_{\text{rot}}(\theta, \gamma, \beta) \cdot \text{diag}(\lambda_1, \lambda_2, \lambda_3) \cdot \boldsymbol{R}_{\text{rot}}(\theta, \gamma, \beta) \tag{5.11}$$

with $\lambda_1 \geq \lambda_2 \geq \lambda_3 = 1 - (\lambda_1 + \lambda_2)$ and $\text{tr}(\boldsymbol{A})=1$. Compared to the description of $\boldsymbol{A}$ by (5.10), expression (5.11) depends on only two (λ_1 and λ_2) instead of five independent parameters. The fiber orientation states can be visualized within the fiber orientation triangle space, spanned by λ_1 and λ_2 satisfying the inequalities

$$\frac{1}{3} \leq \lambda_1 \leq 1 \quad \text{and} \quad \frac{1}{2}(1 - \lambda_1) \leq \lambda_2 \leq \min(\lambda_1, 1 - \lambda_1). \tag{5.12}$$

Köbler et al. [89] introduced a special coloring-scheme to characterize the different fiber orientation states. The three special cases of isotropic, unidirectional, and planar isotropic fiber orientation are described by the corners of the fiber orientation triangle

as depicted in Fig. 5.10. To characterize the material behavior for arbitrary fiber orientation states, each tangential stiffness tensor can be transformed as follows:

$$\boldsymbol{C}'_{\mathrm{eff},V} = \boldsymbol{R}_{\mathrm{rot}} \cdot \boldsymbol{R}_{\mathrm{rot}} \cdot \boldsymbol{C}_{\mathrm{eff,V}} \cdot \boldsymbol{R}^{T}_{\mathrm{rot}} \cdot \boldsymbol{R}^{T}_{\mathrm{rot}}. \tag{5.13}$$

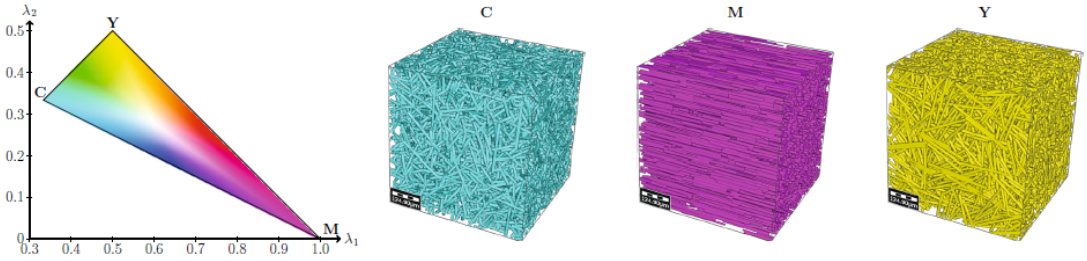

Figure 5.10: Illustration of the fiber orientation state (Fig. taken from [89]) by the fiber orientation triangle and RVEs of the three extreme orientation states (isotropic, unidirectional, and planar isotropic)

As material property descriptors, the linear elastic constants of the fiber material are specified. These are the Young's modulus E_f ranging from 25-250 GPa and the Poisson's ratio ν_f ranging from 0.2 to 0.4. This enables the consideration of many fiber materials relevant in engineering. It is important to mention that due to the consideration of arbitrary orientation states in a post-processing step by specification of three Euler angles θ, γ, β in (5.13), the dimension of the design space to be considered in the numerical model of the time-dependent viscoelastic behavior can be reduced from 8 to 5 independent design variables. This is an important aspect, since reducing the dimension of the design space generally leads to a reduction in the number of samples required and thus the numerical effort can be reduced. The design variables including their lower and upper bounds are listed in Table 5.10.

Design of experiments

The LH scheme according to Section 3.3.3 is utilized to specify the samples to be evaluated within the five-dimensional material design space. This requires the consideration of the feasible area of the constraint fiber orientation space described by inequality (5.12) to avoid unphysical descriptors. The samples that lie outside the feasible range are neglected. A total number of $m = 48$ samples (experiments) spread in the feasible area of the material design space are selected. In Fig. 5.11, the sample distribution in the geometrical microstructure descriptor and in the fiber material property descriptor space is illustrated. One can observe a quite uniform distribution of the samples over the entire design spaces. An RVE is created for each sample and six load cases needs to

Table 5.10: Design variables with lower- and upper bounds

Index i	Design variable d_i	Lower bound $d_{i,low}$	Upper bound $d_{i,up}$
1	V_f / %	5	20
2	λ_1	$0.3\overline{3}$	1
3	λ_2	$0.5(1-\lambda_1)$	$\min(\lambda_1, 1-\lambda_1)$
4	E_f / GPa	25	250
5	ν_f	0.2	0.4
6	θ / rad	0	π
7	γ / rad	0	π
8	β / rad	0	π

be computed to yield the full anisotropic compliance tensor in the form of (5.8). This results in a total number of $48 \cdot 6 = 288$ required simulations. The corresponding material database comprises n_{samp} sets of six inputs $\boldsymbol{d} \in \mathbb{R}^6$ (since the orthotropic parameters are time-dependent, the time can be assumed as additional parameter and $n_{\text{samp}} = m \cdot$ no. of time-increments have to be considered in the surrogate model) and the nine orthotropic parameters $\boldsymbol{y} \in \mathbb{R}^9$ ($y \rightarrow E_{1,\text{eff}}$, $E_{2,\text{eff}}$, $E_{3,\text{eff}}$, $G_{12,\text{eff}}$, $G_{13,\text{eff}}$, $G_{23,\text{eff}}$, $\nu_{12,\text{eff}}$, $\nu_{13,\text{eff}}$, $\nu_{23,\text{eff}}$ as outputs as

$$\{(\boldsymbol{d}^{(1)}, \boldsymbol{y}^{(1)}), (\boldsymbol{d}^{(2)}, \boldsymbol{y}^{(2)}), ..., (\boldsymbol{d}^{(n_{samp})}, \boldsymbol{y}^{(n_{samp})})\}. \tag{5.14}$$

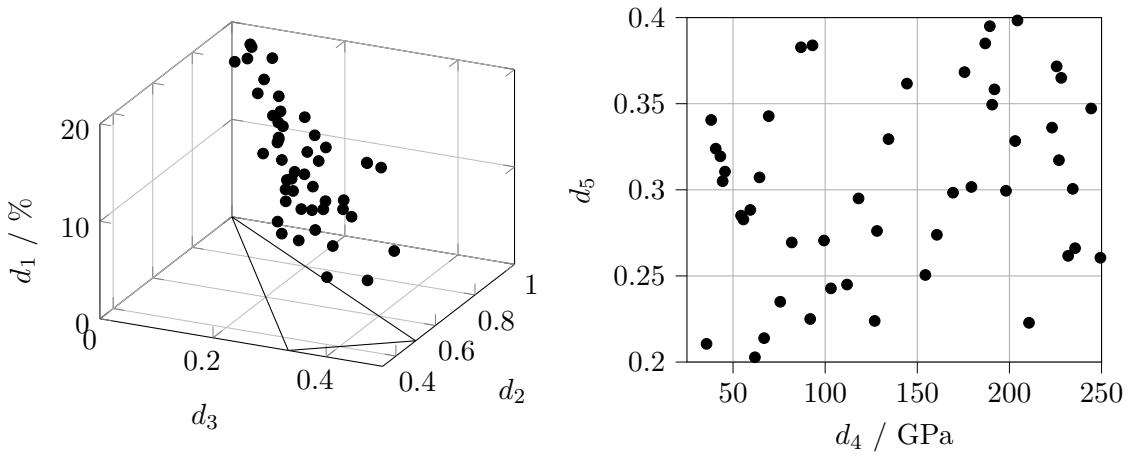

Figure 5.11: LH sample distribution in the geometrical microstructure descriptor (left) and in the fiber material property space (right)

Microstructure generation

The generation of RVEs of SFRPs is performed according to the announcements in

Section 3.4. In order to describe the microstructure of SFRPs, the fiber orientation tensor $\boldsymbol{A}$, the fiber volume fraction as well as the fiber length and the fiber diameters needs to be specified. Fibers with a constant length of 200 µm and an aspect ratio (=fiber length/fiber diameter) of 20 are investigated, which are typical values for SFRPs in industrial applications. The fibers are not allowed to touch each other during the generation of the structure. As RVE parameters, the voxel length h and the number of voxels in each spatial dimension (respectively the edge length l = no. of voxels $\cdot$ h) has to be defined. Only cubical volume elements are considered in the following.

Computation of the effective viscoelastic material parameter

In the following, based on the explanations in Section 3.5.6, the transient microscopic BVP in the RVE domain ω is described. Virtual creep experiments are carried out to determine the overall viscoelastic material behavior in terms of (5.8). For this purpose, a constant macroscopic stress

$$\langle \boldsymbol{\sigma} \rangle = \frac{1}{|\omega|} \int_{\omega} \boldsymbol{\sigma}(\boldsymbol{x}, t) \, \mathrm{d}\omega \tag{5.15}$$

will be applied by the associated traction vector at the boundary $\partial\omega$ of the RVE. The microscopic quantities to be computed are the local stresses $\boldsymbol{\sigma}$, the fluctuating periodic displacement fields $\tilde{\boldsymbol{u}}$, and the macroscopic strain $\langle \boldsymbol{\epsilon} \rangle$. The static balance equation within the RVE domain ω and the considered time intervall reads

$$\operatorname{div} \boldsymbol{\sigma}(\boldsymbol{\epsilon}(\boldsymbol{x}, t)) = 0 \quad \boldsymbol{x} \in \omega \ , \ t \in [0, T]. \tag{5.16}$$

As described in Section 3.5.6, the kinematic compatibility equation for the local strain fields can be expressed in the small strain regime as

$$\boldsymbol{\epsilon}(\boldsymbol{x}) = \langle \boldsymbol{\epsilon} \rangle + \frac{1}{2}(\nabla \tilde{\boldsymbol{u}}(\boldsymbol{x}) + \nabla^T \tilde{\boldsymbol{u}}(\boldsymbol{x})) \quad \boldsymbol{x} \in \Omega. \tag{5.17}$$

The following mixed BCs are prescribed on the boundary $\partial\omega$ of the RVE

$$\begin{aligned} \boldsymbol{t}(\boldsymbol{x}, t) &= \langle \boldsymbol{\sigma} \rangle \cdot \boldsymbol{n}(\boldsymbol{x}) && -\# \quad \boldsymbol{x} \in \partial\omega \\ \tilde{\boldsymbol{u}}(\boldsymbol{x}, t) & && \# \quad \boldsymbol{x} \in \partial\omega, \end{aligned} \tag{5.18}$$

where $\boldsymbol{n}$ is a unit normal vector and $\boldsymbol{t}$ is the applied traction vector resulting from the specification of a macroscopic stress (5.15). As denoted in Section 3.5.6, # in (5.18) means equal strain fluctuations $\tilde{\boldsymbol{u}}$ on opposite RVE sides and $-\#$ means that the traction vector $\boldsymbol{t}$ shows in opposite directions on opposite RVE sides in order to consider static balance. The constitutive behavior of the the polymer material is modeled as linear viscoelastic according to Section 5.2.1. Linear elastic (isotropic) material behavior

is assumed for the fiber material, which is fully described by the specification of the Young's modulus E_f and the Poisson's ratio ν_f. Perfect bonding between the fibers and the matrix is assumed. The unknown overall viscoelastic behavior is assumed to be viscoelastic too. In strain formulation and by using the Voigt notation, it can be expressed in the following form:

$$\langle \epsilon_i \rangle = \int_0^t \Upsilon_{ij,\mathrm{eff}}(t-s) \cdot \langle \frac{\partial \sigma_j(s)}{\partial s} \rangle \, \mathrm{d}s, \quad (i,j = 1,2,...,6). \tag{5.19}$$

Therein, $\boldsymbol{\Upsilon} : [0,T] \rightarrow \mathbb{R}^3 \otimes \mathbb{R}^3 \otimes \mathbb{R}^3 \otimes \mathbb{R}^3$ corresponds to the fourth-order symmetric macroscopic creep compliance tensor to be determined. By specification of the jth component of a stepped macroscopic stress tensor $\langle \sigma_j \rangle = H(t-t_0) \cdot \sigma_0$, the components of the creep compliance tensor

$$\Upsilon_{ij,\mathrm{eff}} = \frac{\langle \epsilon_i \rangle}{\langle \sigma_j \rangle}, \quad (i,j = 1,2,...,6) \tag{5.20}$$

can be computed by the solution of six BVPs (by prescibing three tension and three shear loads according to (5.18) in perpendicular coordinate directions). The transient BVP can be interpreted as a linear elastic problem to be solved in each time step. In the following, a stress value of $\sigma_0 = 1$ MPa is specified. The considered time interval is set to $T = 10^4$ s. Investigations with varying step size reveal that 32 time increments (8 per decade) equally spread over the logarithmic time scale provide sufficient accuracy. For the solution of (5.16)-(5.18), an FFT-based solution scheme is applied. The conjugate gradient (CG) method [53] with a tolerance of $5 \cdot 10^{-5}$ is used. The computations are performed by the FeelMath solver integrated in the ElastoDict module [148] of GeoDict [14]. In Fig. 5.12, the RVE representation for a sample (left) and the creep curves for the applied tensile and shear load are illustrated. The corresponding von Mises strain fields within a cross-sectional area of the RVEs are illustrated in Fig. 5.13 for the last time increment. Due to the relatively large stiffness of the fibers, the largest strain values are localized in the matrix material, especially in the immediate vicinity of the fibers.

RVE convergence study

In this subsection, the influence of the size of the RVEs and the influence of the resolution on the homogenization results are examined. To investigate the influence of the edge length, a RVE with an edge length of 1200 µm and a voxel length of 1 µm (10 voxels per fiber diameter) is considered as reference. The three extreme orientation states (isotropic, planar isotropic, and unidirectional) with $V_f = 20$ % are investigated and the edge length is gradually increased by 200 µm starting at 400 µm. As error metric, the relative error of the macroscopic creep compliance tensor according to (5.8) in the Frobenius norm is computed. The corresponding results evaluated at $t = 10^4$ s are illustrated

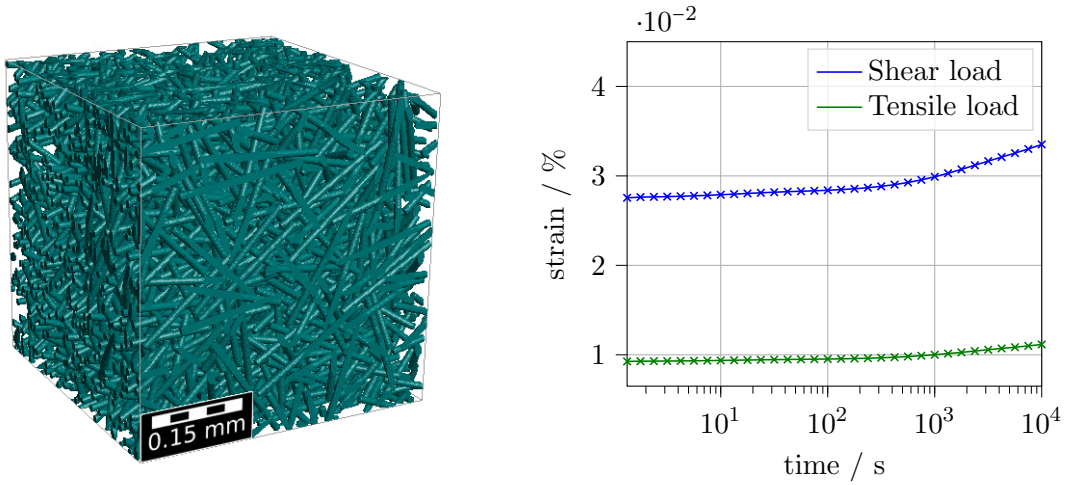

Figure 5.12: RVE representation of a sample with $d_1 = 16.635$ %, $d_2 = 0.543$, $d_3 = 0.399$ (left) and creep curves for a prescribed macroscopic tensile load in x_1-direction and a macroscopic shear load of 1 MPa in the x_1x_2-plane (right)

in Fig. 5.14 (left). It can be observed that for the isotropic and unidirectional fiber orientation state, the error decreases from about 10 % for the smallest edge length to less than 5 % for an edge length of 800 µm. The error of the planar isotropic orientation state shows a nearly constant value of about 8 %. This may be due to the fact that for the orientation states and fiber volume fractions considered here, the generation of the geometrical microstructures at different edge lengths shows slight deviations from each other. The influence of the resolution of the structure is investigated by varying the number of voxels per fiber diameter. For this purpose, an RVE with an edge length of 600 µm and a voxel number of 1200 (20 voxels per fiber diameter) is considered as a reference. The resolution is gradually increased by 2 voxels per fiber diameter starting with 6 voxels per fiber diameter. Again, the three extreme fiber orientation states are examined. The relative error in the Frobenius norm for $t = 10^4$ s is depicted in Fig. 5.14 (right). By specification of 14 voxels per fiber diameter, the relative error is below 5 % for all orientation states. It should be noted that this can be considered as a worst-case assumption, since both the extreme fiber orientation states and the maximum stiffness contrast are considered here. In the following, cubic RVEs with an edge length of 500 µm and a voxel length of 1 µm are generated for each sample, which seems to be a reasonable tradeoff between computational effort and accuracy.

Surrogate modeling

Based on the created material database (5.14), Kriging surrogate models for the nine

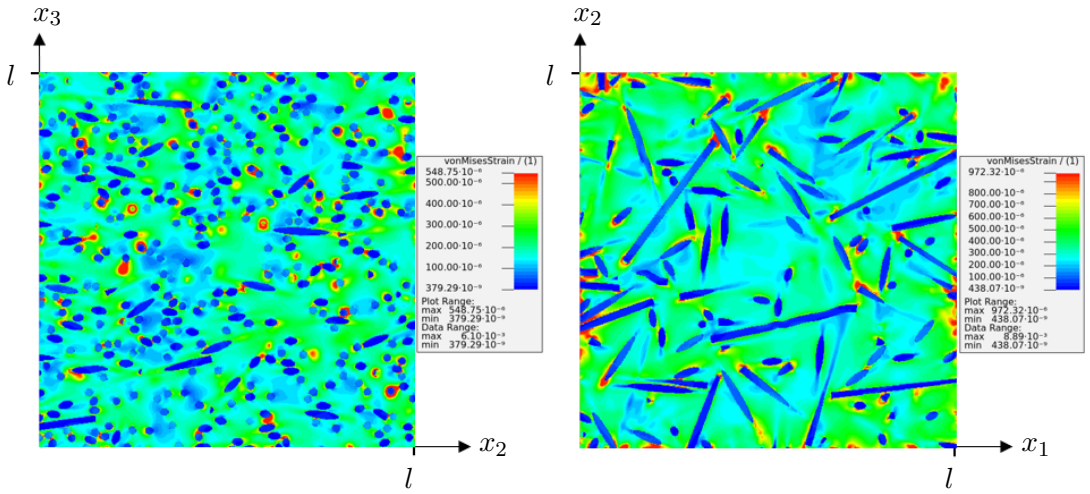

Figure 5.13: Von Mises strain fields for the considered load cases (tensile load: left, shear load: right) at $t = 10^4$ s within a cross-sectional area (half RVE length) of the associated RVE with $d_4 = 198.125$ GPa and $d_5 = 0.3$.

time-dependent effective viscoelastic material parameters will be created. This allows the representation of the full anisotropic overall viscoelastic material behavior in the form of (5.8) that is characterized by three Young's moduli, three shear moduli, and three Poisson's ratios as a function of the design variables. In the following optimization example, the time interval is chosen as $t \in [10^{0.125}, 10^4]$ s. The time dependence is modeled on the logarithmic time scale considering five time steps for each material parameter (one for each decade ($t = 10^1$, ..., 10^4 s) and one for the first time increment at $t = 10^{0.125}$ s). This results in a total number of $n_{\text{samp}} = 48 \cdot 5 = 240$ samples used to build each surrogate model. In order to test the prediction quality of the Kriging models, an error analysis by k-fold cross validation with $k = 6$ is conducted. The e_{MAPE} values (3.47) of the individual Kriging surrogates are listed in Table 5.12. It can be observed that the surrogate models can predict the viscoelastic behavior quite well with a maximum error of 3.07 % for $G_{13,\text{eff}}$.

Optimization and robustness evaluation

The description of the effective viscoelastic material parameters with surrogate models leads to a corresponding surrogate representation of the objective function according to (5.9). The target values usually result from the specific product requirements and can be derived by optimization at the component level. A possible technical application are seals, for example, where the time-dependent viscoelastic material parameters can be designed to satisfy a specific leak tightness. In the following, it is assumed that these

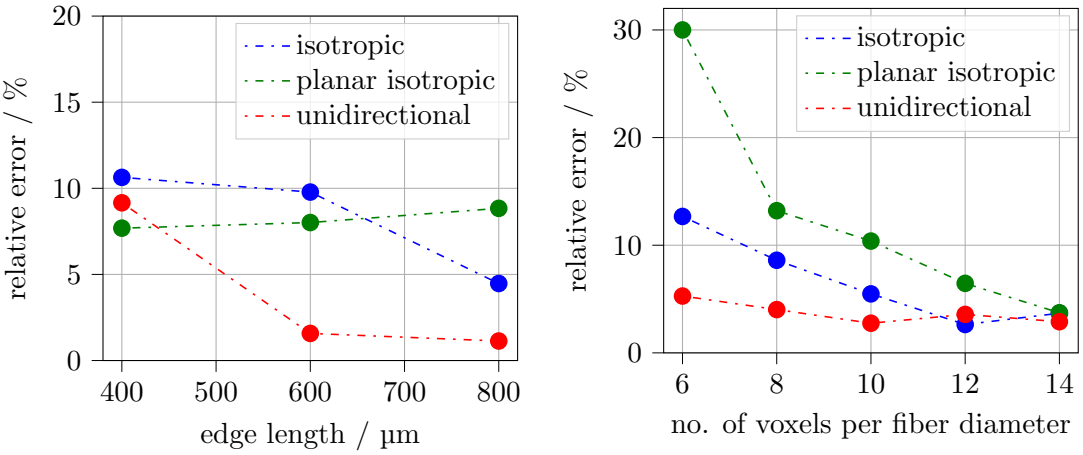

Figure 5.14: Relative error of the creep compliance tensor in the Frobenius norm in dependence of the edge length (left) and the resolution (right) for the three extreme fiber orientation cases

target values are given as a result of such a component specification. For demonstration purposes, the desired viscoelastic material parameters are obtained for the following microstructural configuration: d_1=12 %, d_2=0.57, d_3=0.33 (λ_3 = 0.1), d_4 = 72 GPa, and d_5 = 0.22 (according to glass fibers) at room temperature (T = 23°C) at $t = 10^4$ s. These are listed in Table 5.11. In the following example, the rotational degrees of freedom (d_6 to d_8) are not considered as additional design variables, thus the material behavior is described in terms of 5 design variables.

Table 5.11: Target values of the orthotropic components

Component	$E^*_{1,\text{eff}}$	$E^*_{2,\text{eff}}$	$E^*_{3,\text{eff}}$	$G^*_{12,\text{eff}}$	$G^*_{13,\text{eff}}$	$G^*_{23,\text{eff}}$	$\nu^*_{12,\text{eff}}$	$\nu^*_{13,\text{eff}}$	$\nu^*_{23,\text{eff}}$
Units	GPa	GPa	GPa	GPa	GPa	GPa	1	1	1
	5.17	4.29	3.83	1.71	1.42	1.37	0.3660	0.3756	0.4084

For the solution of the optimization problem, the constraint version of DE as mentioned in Section 3.8.4 is employed. An initial population of size N_p = 75 is generated. The candidates are uniformly distributed within the design space by LHS. The DE/best/1/bin strategy is used. A crossover probability P_{cross} of 0.7 is selected and the mutant factor F is chosen to be in the range between 0.5 and 1 employing dithering. In Fig. 5.15, the objective function value (fitness) is plotted against the number of iterations. For a termination tolerance of $1 \cdot 10^{-3}$ (convergence is reached if the standard deviation of the population energies normed by the mean is smaller than that value), the algorithm stops after 48 iterations and 3638 function evaluations. The optimization result is listed

Table 5.13: Optimization results obtained from the surrogate representation

Design no.	d_1^*	d_2^*	d_3^*	d_4^*	d_5^*	$J(\boldsymbol{d}^*)$
Units	%	1	1	GPa	1	1
1	12.02	0.56	0.34	70.92	0.28	$2.33{\cdot}10^{-4}$
2	11.12	0.55	0.34	84.10	0.29	$5.22{\cdot}10^{-4}$
3	12.92	0.58	0.34	61.33	0.26	$8.56{\cdot}10^{-4}$
4	10.28	0.55	0.34	99.80	0.29	$1.18{\cdot}10^{-3}$

in Table 5.13 (design no. 1). The discrepancies from the target values are quite small, i.e., a value of $J(\boldsymbol{d}^*) = 9 \cdot 10^{-4}$ implies a deviation of 3 % in one of the nine viscoelastic constants in the expression of the objective function.

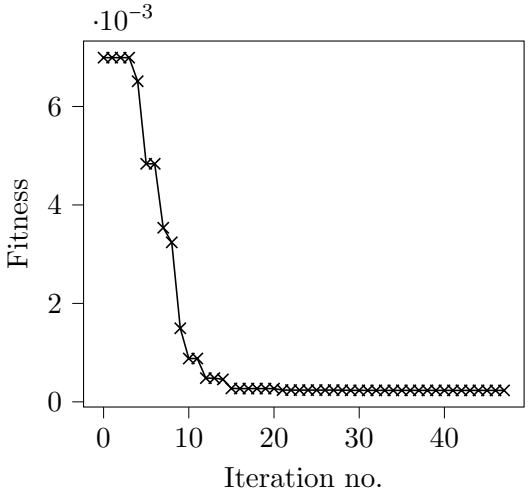

Figure 5.15: Fitness versus number of iterations for the first optimization run

Component	e_{MAPE} / %
$E_{1,\mathrm{eff}}$	2.48
$E_{2,\mathrm{eff}}$	1.70
$E_{3,\mathrm{eff}}$	2.45
$G_{12,\mathrm{eff}}$	1.95
$G_{13,\mathrm{eff}}$	3.07
$G_{23,\mathrm{eff}}$	3.00
$\nu_{12,\mathrm{eff}}$	2.35
$\nu_{13,\mathrm{eff}}$	2.48
$\nu_{23,\mathrm{eff}}$	1.79

Table 5.12: e_{MAPE} of the individual Kriging surrogate models

In a next step, alternative design variants should be found and examined for their robustness. For the evaluation of the robustness of the designs, the worst-case measure ρ_R according to Section 3.9.2 is investigated and the size of the hypercube is specified with $\delta = 0.075$. Since one is interested in finding different design variants, user-specific constraints, e.g., the hypercube area (3.78) with a size defined by specification of δ can be added in (5.9) to find variants that differ to a certain level from the previous ones during renewed optimization. Three additional optimizations are performed for illustration purposes. The additional user-specific constraints are chosen here such that the upper and lower bounds of the fiber volume fraction defined by the hypercube are established

as additional constraints in (5.9). This can be regarded as an iterative process, controlled by specifying the desired number of optimized designs and setting a maximum value of the objective function that prevents the designs deviating too much from the target behavior. The resulting design alternatives are listed in Table 5.13. It can be observed that even for the alternative design variants (design no. 2-4), the deviation from the desired viscoelastic behavior is quite small. The microstructural realizations in the form of RVEs are shown in Fig. 5.16. In Table 5.14, the worst-case measure ρ_R (3.79) of the four identified designs are listed. There are no major differences in the robustness of the different variants. However, the results of such robustness evaluations might be an additional criterion for the designer to select an appropriate variant.

Table 5.14: Worst-case measure and objective function value of the metamodel compared with the results from the micromechanical model for the four identified "optimal" designs

Design no.	$\rho_R(\boldsymbol{d}^*)$	$J(\boldsymbol{d}^*)$	$J_{\text{num}}(\boldsymbol{d}^*)$
1	$4.17{\cdot}10^{-2}$	$2.33{\cdot}10^{-4}$	$6.40{\cdot}10^{-4}$
2	$4.15{\cdot}10^{-2}$	$5.22{\cdot}10^{-4}$	$7.21{\cdot}10^{-4}$
3	$4.52{\cdot}10^{-2}$	$8.56{\cdot}10^{-4}$	$3.92{\cdot}10^{-4}$
4	$4.15{\cdot}10^{-2}$	$1.18{\cdot}10^{-3}$	$1.64{\cdot}10^{-3}$

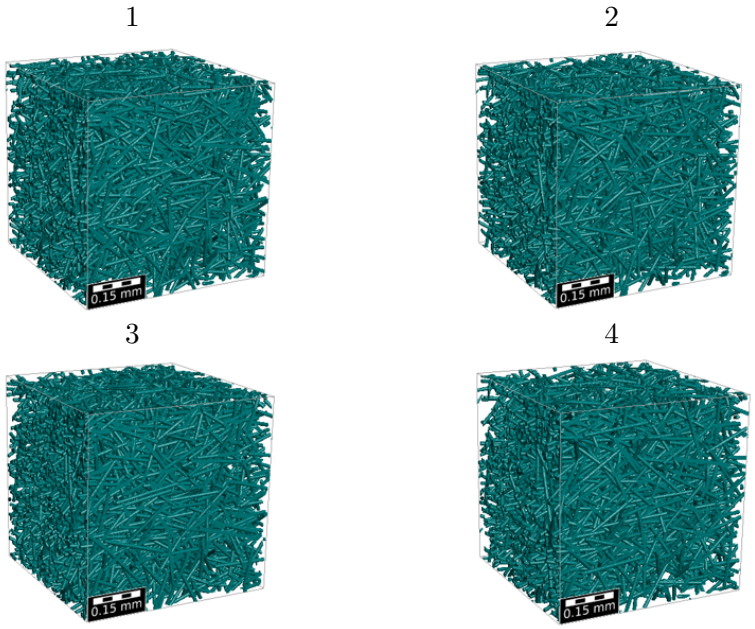

Figure 5.16: RVE representation of a set of four "optimal" microstructural designs

Since the optimizations were carried out on a faulty surrogate model, each identified optimum is validated by the evaluation of a micromechanical simulation. RVEs with an edge length of 600 µm and a resolution of 14 voxels per fiber diameter are considerd. Table 5.14 compares the objective function values of the optimas obtained by the surrogate model with the evaluation of the micromecahnical model. Only minor differences can be observed. For the specified target viscoelastic parameters, the surrogate model can predict the behavior quite well. When manufacturing composite parts, the designer can therefore choose from different variants the one that is easiest or most cost-effective to produce.

5.2.3 Experimental validation

In this subsection, the homogenization results were calibrated by comparison with corresponding measurements. For this purpose, the isochronous stress-strain curves for the considered material (PA66, Zytel 70G30HSLR NC010) available from the polymer material database CAMPUS (Altair Engineering GmbH 2022) [27] are investigated. A fiber weight fraction of 30 % (corresponding to a fiber volume fraction of 17 %) is analyzed. The viscoelastic material parameters identified in Section 5.2.1 are used for the specification of the simulation. A fiber orientation state of $\lambda_1 = 0.78$ and $\lambda_2 = 0.1$ is considered, because this is a common fiber orientation state realized in test specimens. In Fig. 5.17, the simulated creep curve for a macroscopic load of 32 MPa is compared with the experimental measurements. This value is chosen because the stresses in the polymer of the SFRP best corresponds to the stress for which the viscoelastic material parameter of the neat polymer were identified. There can be observed only small differences within the considered time history with a deviation of less than 10 %. By further varying the fiber orientation distribution, no better correspondence could be achieved. The deviations can result from other test conditions or nonlinear viscoelastic effects.

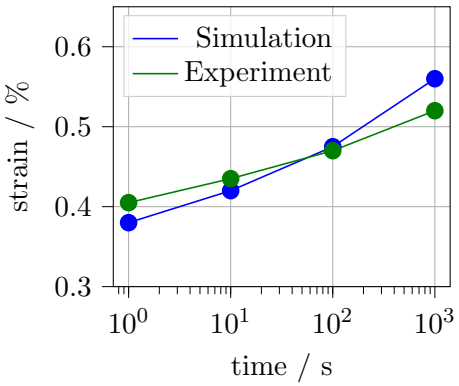

Figure 5.17: Comparison of creep simulation results with experimental results for an applied tensile load of 32 MPa

5.3 Multiphysical optimization of the three-phase PRP

Especially in the context of electromobility applications, it is usually not sufficient to consider purely thermal or mechanical requirements for the material properties, as in the previous examples. As stated in the motivation, different physical material properties must be taken into account in their entirety in order to fulfil specific multiphysical product requirements. In this section, the surrogate-based multiscale optimization method is adopted to address such multiphysical issues. For that purpose, a formulation of the material optimization problem as MOO problem is introduced. Surrogate models for each effective physical material property (respectively the individual design objectives and constraints) are constructed. These surrogate representations enables to find an approximation of the conflicting design objectives in terms of the Pareto front by population-based MOO methods in an efficient way.

5.3.1 Optimization approach

In the following, the surrogate-based MOO approach is demonstrated by the example of the previously considered three-phase PRP (see Section 5.1). In addition to the requirement of a target ETC k^*_{eff}, the multiphysical problem statement includes the demand for a desired overall coefficient of thermal expansion (CTE) α^*_{eff} and the specification of a maximum effective stiffness in terms of the Young's modulus $E_{\text{eff,max}}$ as constraint. The following MOO problem for the design variables $\boldsymbol{d}$ is formulated:

$$\begin{aligned} J_1(\boldsymbol{d}) &= \left(\frac{k_{\text{eff}}(\boldsymbol{d}) - k^*_{\text{eff}}}{k^*_{\text{eff}}} \right)^2 \rightarrow \min \\ J_2(\boldsymbol{d}) &= \left(\frac{\alpha_{\text{eff}}(\boldsymbol{d}) - \alpha^*_{\text{eff}}}{\alpha^*_{\text{eff}}} \right)^2 \rightarrow \min \\ \text{s. t.} \quad & g(\boldsymbol{d}) = E_{\text{eff}}(\boldsymbol{d}) - E_{\text{eff,max}} \leq 0, \\ & d_{i,low} \leq d_i \leq d_{i,up}. \end{aligned} \tag{5.21}$$

In this example, both design variables of the geometrical microstructure and the material properties of the filler particles are investigated. Besides the descriptor of the geometrical microstructure in terms of the filler volume fraction V_f and the phase proportion of the platelet-shaped particles δ_{fp}, the thermomechanical (isotropic) material parameter E, ν, α, k of the filler particles are specified as design variables. The problem statement comprises a total of $n = 10$ design variables chosen to cover a wide range of different technical relevant fillers. The design variables and their lower and upper bounds are listed in Table 5.15. The thermomechanical material parameter of the PBT matrix are considered to be constant at room temperature and are listed in Table 5.16. Please

Table 5.15: Design variables with lower- and upper bounds

Index i	Design variable d_i	Lower bound $d_{i,low}$	Upper bound $d_{i,up}$
1	V_f / %	0	34
2	δ_{fp} / %	0	75
3	E_{sp} / GPa	50	400
4	ν_{sp}	0.2	0.3
5	α_{sp} / (ppm/K)	4	6
6	k_{sp} / (W/mK)	2	40
7	E_{fp} / GPa	10	320
8	ν_{fp}	0.1	0.3
9	α_{fp} / (ppm/K)	0.1	5
10	k_{fp} / (W/mK)	150	400

note that these material parameters are in general a function of the temperature, i.e., E_m decreases with increasing temperature, while α_m increases. Such thermomechanical material optimization problems could be relevant for example for molding materials of encapsulated circuits. For such applications, in addition to a target ETC, a certain CTE (that coincides with the circuit board's) is sought. The demand for a maximum stiffness could be of importance in order to reduce stresses (and failure) due to a missmatch of the CTEs of both materials under temperature loading.

Table 5.16: Thermomechanical material parameter of the PBT matrix

E_m / GPa	ν_m	α_m / (ppm/K)	k_m / (W/mK)
2.3	0.4	60	0.23

Design of Experiments and microstructure generation

To create surrogate models of the individual objective functions, the thermomechanical SPR is evaluated based on well-chosen samples within the material design space. It is obvious that, except of the design variables of the geometrical microstructure d_1 and d_2, not each effective material property considered in MOO problem (5.21) depends on all 10 design variables. For example, the overall thermal material behavior is completely specified by the design variables of the geometrical microstructure and the thermal conductivities of the fillers (d_6 and d_{10}). Following that, the design space is splitted into two subsets - one set of design variables describing the ETC k_{eff} and another set of design variables for E_{eff} and α_{eff}. In the first set, the 4-dimensional design space for the modelling of the ETC is explored by the creation of 38 LH samples. For the modeling of the thermoelastic behavior, 80 LH samples are selected within the 8-dimensional design space. For illustration purposes, the projections of the sample distributions within

selected 2D and 3D material design spaces are illustrated for both subsets in Fig. 5.18. A fairly even distribution of the samples within the design spaces can be observed. For each individual sample, a microstructure according to the announcements in Section 5.1 is generated. The particle sizes are fixed to their upper bounds (see Table 5.2).

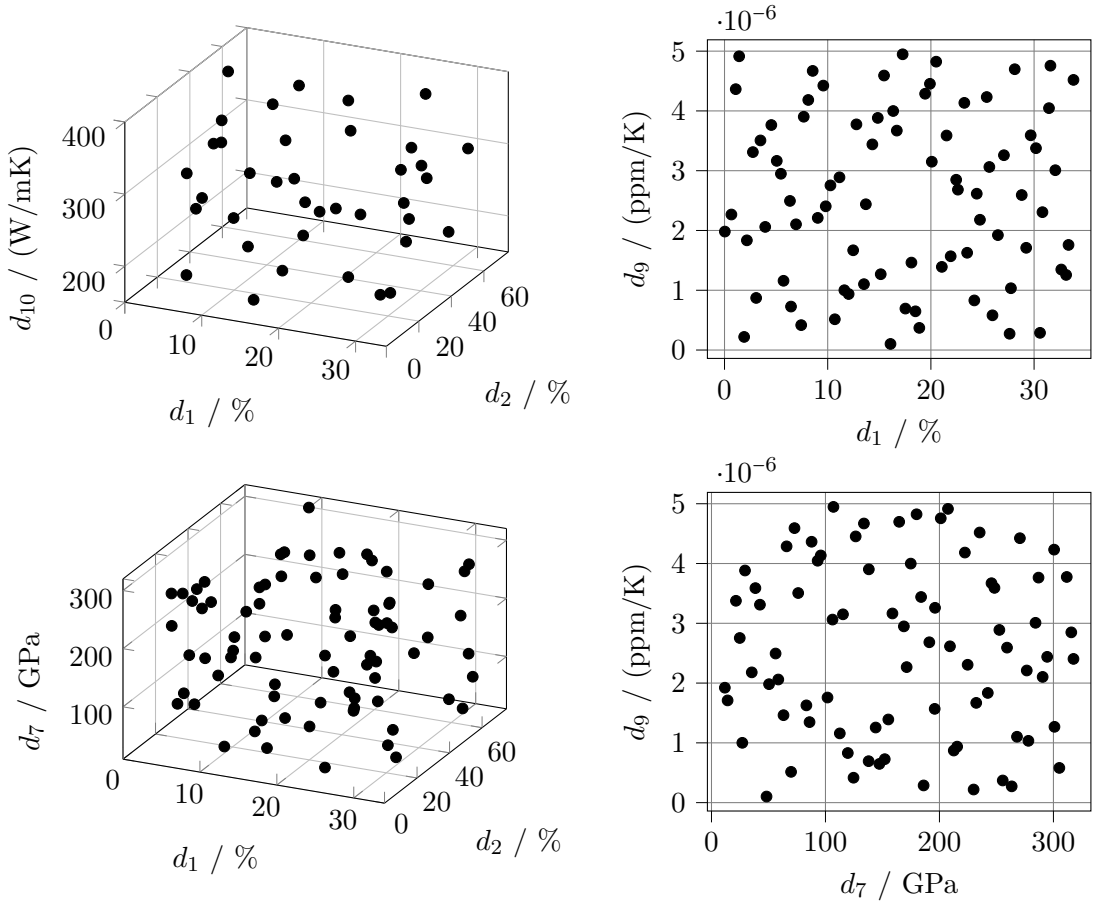

Figure 5.18: Projections of the LH sample distribution within selected 2D and 3D material design spaces

Computation of the effective thermal expansion tensor

In the following, the computation of the effective thermal expansion tensor $\boldsymbol{\alpha}_{\text{eff}}$ (considered in J_2) to describe the overall thermoelastic material behavior of the three-phase PRP is described. For that purpose, a corresponding BVP in the RVE domain ω is formulated. This BVP is not further elaborated here, because it is a simple extension of the pure linear elastic localization problem described in Section 3.5.6 by replacing Hooke's

law (2.14) by (2.19) and the specification of a temperature increment ΔT. Supplementary to the notations and explanations in Section 5.1, the RVE domain $\omega = (0,l)^3 \subset \mathbb{R}^3$ of the three-phase PRP is subdivided into three subdomains (phases) ω_p ($p = 1,2,3$), which are associated by the stiffness tensor $\boldsymbol{C}(\boldsymbol{x}) = \boldsymbol{C}_p$ for $\boldsymbol{x} \in \omega_p$ and the thermal expansion tensor $\boldsymbol{\alpha}(\boldsymbol{x}) = \boldsymbol{\alpha}_p$ if $\boldsymbol{x} \in \omega_p$. Please note that $p = 1$ corresponds to the thermomechanical material properties of the matrix (index m, see Table 5.16), $p = 2$ those of the spherical particles (index sp), and $p = 3$ those of the platelet-shaped particles (index fp), see Table 5.15. Since isotropic material behavior of the constituents is assumed in (2.19), $\boldsymbol{\alpha}_p$ can be expressed as a scalar value, i.e., $\boldsymbol{\alpha}_p = \alpha_p \boldsymbol{I}$. Correspondingly, the stiffness tensor of each phase $\boldsymbol{C}_p$ is defined by the specification of the Young's modulus E_p and the Poisson's ratio ν_p. In analogy to the local form of (2.19), the macroscopic thermoelastic behavior can be expressed as

$$\langle \boldsymbol{\sigma}_V \rangle = \boldsymbol{C}_{\text{eff,V}} \cdot \langle \boldsymbol{\epsilon}_{V,\text{el}} \rangle = \boldsymbol{C}_{\text{eff,V}} \cdot (\langle \boldsymbol{\epsilon}_V \rangle - \boldsymbol{\alpha}_{\text{eff,V}} \cdot \Delta T) \tag{5.22}$$

with the unknown effective thermal expansion tensor $\boldsymbol{\alpha}_{\text{eff,V}}$. For the computation of $\boldsymbol{\alpha}_{\text{eff}}$, a macroscopic strain $\langle \boldsymbol{\epsilon} \rangle = 0$ and a temperature increment of $\Delta T = 1$ K acting in the entire microscopic domain ω is prescribed. As result, the local strain field $\boldsymbol{\epsilon}_{\text{therm}}$ is obtained and the effective thermal expansion tensor can be computed as

$$\boldsymbol{\alpha}_{\text{eff,V}} = -\frac{1}{\Delta T} \boldsymbol{C}^{-1}_{\text{eff,V}} \cdot \langle \boldsymbol{\sigma}_{V,\text{therm}} \rangle \tag{5.23}$$

where $\langle \boldsymbol{\sigma}_{V,\text{therm}} \rangle$ denotes the macroscopic stress due to the pure thermal macroscopic strain $\langle \boldsymbol{\epsilon}_{V,\text{therm}} \rangle$. (5.23) indicates that the effective thermal expansion tensor is related to the elastic constants of the composite and requires the knowledge of the full stiffness tensor. The stiffness tensor is computed as described in Section 3.5.6 by specification of periodic BCs with a prescribed macroscopic strain of 0.005 % at reference temperature T_0. The solver FeelMathVox implemented in the ElastoDict module [148] of GeoDict [14] is employed for the computation of the thermoelastic properties. In summary, seven load cases are computed (six load cases for the computation of $\boldsymbol{C}_{\text{eff}}$ and a single load case for the computation of $\boldsymbol{\alpha}_{\text{eff}}$ according to 5.23) to determine the macroscopic thermoelastic material behavior. The CTE $\alpha_{\text{eff}}(\boldsymbol{d})$ in (5.21) will be determined from the mean value of the main diagonal components of the effective thermal expansion tensor, i.e., $\alpha_{\text{eff}}(\boldsymbol{d}) = \frac{1}{3}\text{tr}(\boldsymbol{\alpha}_{\text{eff}}(\boldsymbol{d}))$. The calculation of the ETC $k_{\text{eff}}(\boldsymbol{d})$ is completely analogous to the explanations in Section 5.1.

RVE convergence study

A representativeness study according to Section 3.5.7 is conducted to ensure a sufficiently accurate calculation of the effective thermomechanical material properties. The determination of the size and resolution of the RVE for the computation of the ETC

has already been performed in Section 5.1. Based on these results, RVEs specified by the LH samples for the computation of k_{eff} consist of $450 \times 450 \times 450$ voxels. These investigations are now carried out in an analogous manner for E_{eff} and α_{eff}. The extreme cases of setting the design variables to their upper bounds are investigated. Starting with an edge length of 200 µm, the size of the cubic RVEs is gradually increased by 100 µm. Fig. 5.19 depicts E_{eff} and α_{eff} for an ensemble size of $N = 4$ as a function of the edge length l for a voxel length of $h = 1$ µm. It can be observed that the influence of the edge length is less pronounced compared to the consideration of the overall thermal properties. Evaluating criterion (3.28) for the edge lengths of 300 and 450 µm reveals that $\epsilon_{vol} < 7 \cdot 10^{-3}$ for both E_{eff} and α_{eff}. Hence, an edge length of $l = 400$ µm is chosen, which seems to be a reasonable compromise between computational effort and accuracy. To investigate the influence of the resolution of the RVE on the homogenization results, the resolution of the structure with $l = 400$ µm and $h = 1$ µm is reduced by the factor 3 and criterion (3.29) is examined. It can be observed that the differences in the effective Young's modulus E_{eff} and in the CTE α_{eff} amount to about 1 % due to the refinement. From a practical point of view, this means that the effective thermomechanical properties are independent from the resolution of the RVE. Based on these investigations, each microstructural design specified by the LH scheme for the thermoelastic case will be generated with an edge length of $l = 400$ µm and a voxel length of $h = 1$ µm, so the resulting structures consist of $400 \times 400 \times 400$ voxels. In Fig. 5.20, the von Mises stress and strain fields within an corresponding RVE for an applied tensile load is shown. The largest strains (only displayed here within the matrix material) can be observed in the soft polymer matrix, especially in vicinity to the filler particles. The largest stresses occur in the stiff filler particles (especially the platelet-shaped particles), which carry most of the load of the composite.

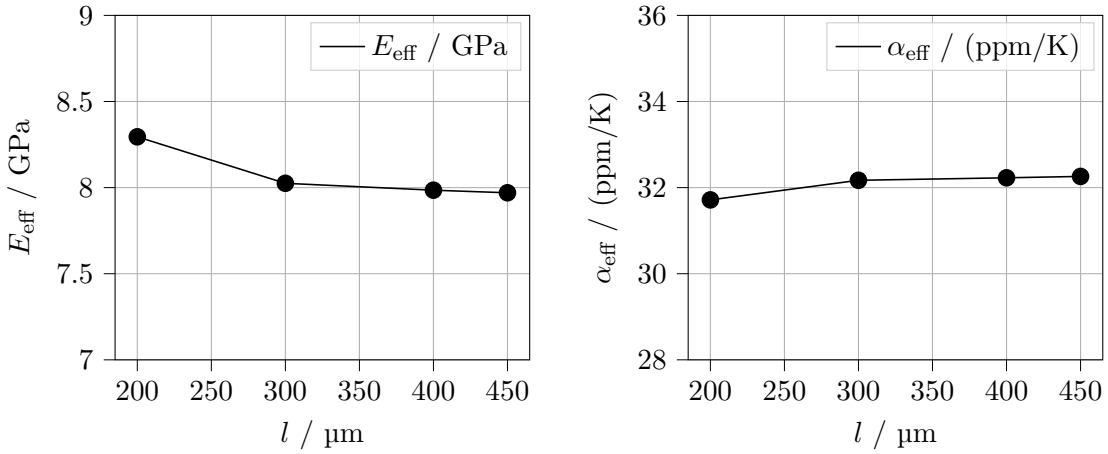

Figure 5.19: E_{eff} (left) and α_{eff} (right) in dependence of the edge length l

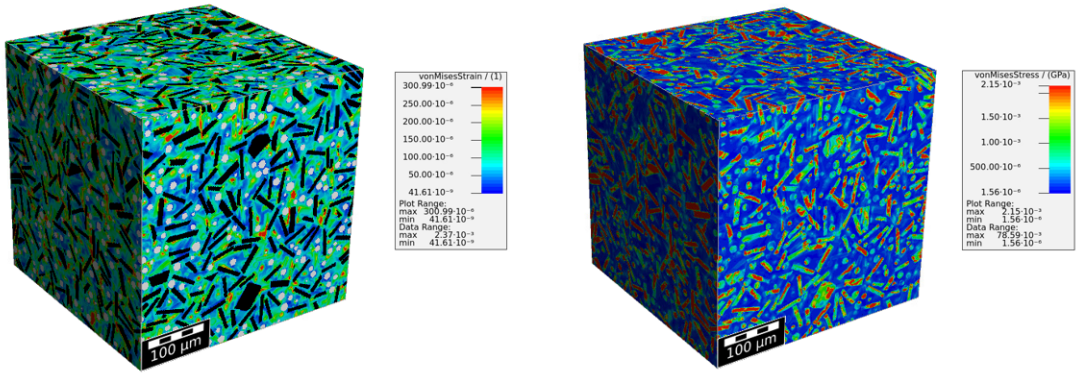

Figure 5.20: Von Mises strain (left) and stress (right) within an RVE of the three-phase PRP under tensile load for prescribed periodic BCs

Construction of thermomechanical surrogate models

Kriging surrogate models are utilized for the modeling of the individual effective thermomechanical properties E_{eff}, α_{eff}, and k_{eff}. The surrogates are trained by k-fold CV with $k = 5$. The e_{MAPE} (3.47) and e_{RMSE} (3.45) are investigated as error metrics. In Table 5.17, the average values of these measures are listed for all three surrogates. It can be observed that the Kriging models exhibit quite good prediction capabilities for each individual quantity. A maximum error of e_{MAPE} =2.48 % is obtained for the surrogate model of k_{eff}. In order to visualize the SPR, some response surfaces are shown in Fig. 5.21. In each case, the influence of two design variables on a specific thermomechanical quantity is illustrated. The remaining design variables are set to their upper bounds (see Table 5.15). The response surface of the ETC shows good agreement with Fig. 5.6. The macroscopic Young's modulus E_{eff} increases with increasing volume fraction V_f and increasing proportion of the plateled-shaped particles δ_{fp}. The influence of V_f and δ_{fp} on α_{eff} is shown in the lower left panel. The volume fraction is much more sensitive, however α_{eff} slightly decreases for increasing δ_{fp}. The influence of V_f and the stiffness of the platelet-shaped particles E_{fp} on E_{eff} is illustrated in the lower right panel. Especially for increasing volume fractions, a strong increase in E_{eff} can be observed for increasing E_{fp}.

Table 5.17: Error metrics of the individual thermomechanical surrogate models

Physical quantity	k_{eff}	E_{eff}	α_{eff}
e_{MAPE} / %	2.48	1.38	0.31
e_{RMSE}	0.015 / (W/mK)	0.083 / GPa	0.178 / (ppm/K)

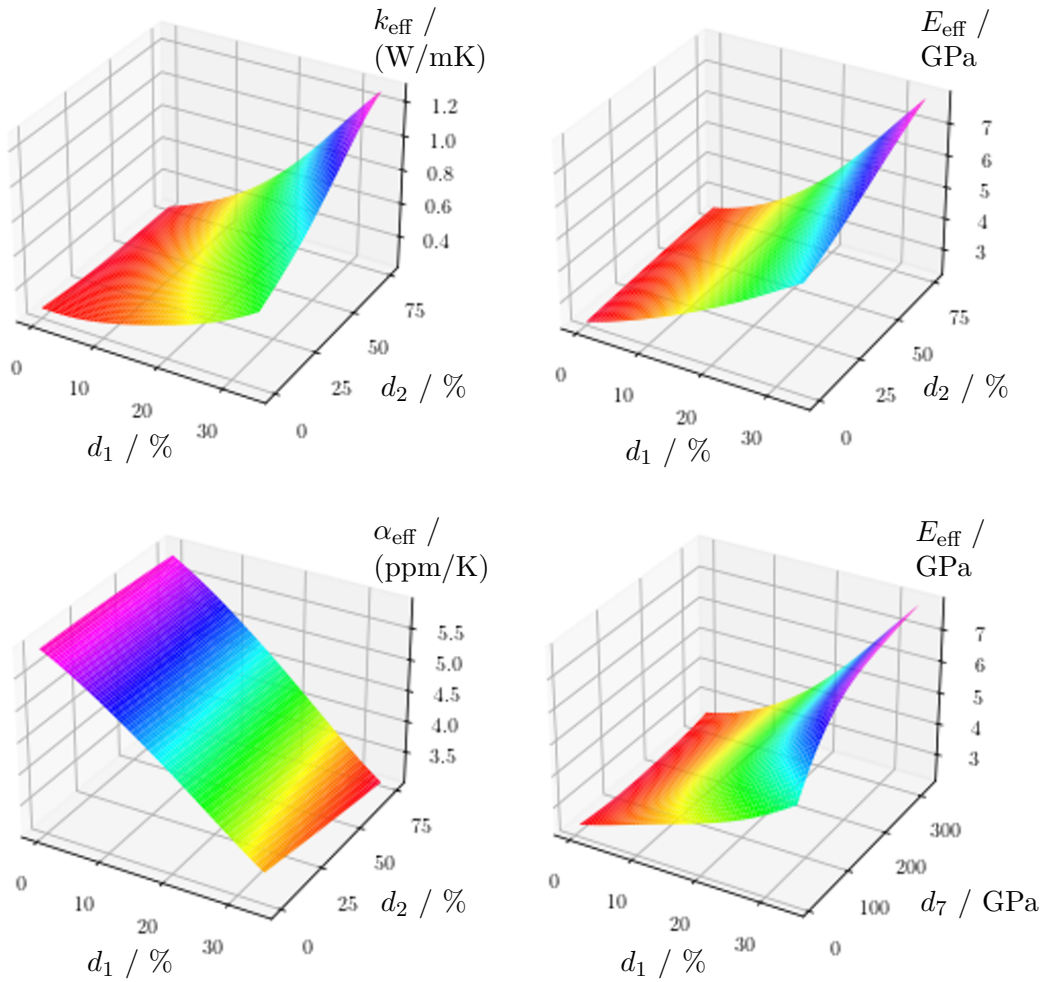

Figure 5.21: Response surfaces for individual thermomechanical properties of the three-phase PRP within selected design spaces

Global sensitivity analysis

To gather more quantitative information about the impact of the individual design variables on a quantity of interest, a sensitivity analysis is conducted. Total-order indices S_{T_i} are computed for each design variable based on $2 \cdot 10^{16}$ samples according to Section 3.7. The corresponding indices are listed in Table 5.18. It can be observed that the filler volume fraction is by far the most sensitive parameter and dominates the thermomechanical behavior. The phase proportion δ_{fp} also has a considerable effect on the thermomechanical properties, especially for k_{eff}. Since isolated filler particles are considered, the thermal conductivities of the particles has almost no effect on the overall

ETC. This is in agreement with results from literature, which indicate that for isolated particles the ETC is only influenced up to a ratio of the conductivities of the fillers to the matrix by a factor of about 10. The stiffness of the platelet-shaped particles E_{fl} has a significant impact on E_{eff}, while the stiffness of the spherical particles E_{sp} is negligible. This illustrates that the considered effective properties considered in this example are almost exclusively determined by the filler volume fraction and the phase proportions δ_{fp}.

Table 5.18: Total-order index S_{T_i} of the individual design variables

Index i	$S_{T_i} - k_{\text{eff}}$	$S_{T_i} - E_{\text{eff}}$	$S_{T_i} - \alpha_{\text{eff}}$
1	$8.83 \cdot 10^{-1}$	$9.57 \cdot 10^{-1}$	$9.87 \cdot 10^{-1}$
2	$1.89 \cdot 10^{-1}$	$4.02 \cdot 10^{-2}$	$1.23 \cdot 10^{-2}$
3	-	$1.14 \cdot 10^{-3}$	$8.13 \cdot 10^{-5}$
4	-	$4.56 \cdot 10^{-6}$	$3.11 \cdot 10^{-6}$
5	-	-	$1.54 \cdot 10^{-4}$
6	$3.05 \cdot 10^{-3}$	-	-
7	-	$3.37 \cdot 10^{-2}$	$5.31 \cdot 10^{-3}$
8	-	$1.62 \cdot 10^{-5}$	$6.61 \cdot 10^{-5}$
9	-	-	$5.99 \cdot 10^{-4}$
10	$2.42 \cdot 10^{-4}$	-	-

5.3.2 Case study 1

In the following, the NSGAII algorithm implemented in the Python library Platypus [56] is utilized to obtain the solutions on the surrogate representation of the MOO problem (5.21). In this implementation, the mutation and crossover operator are selected by analyzing the individual problem using best practice. However, several individual settings can be performed. For the problem at hand, a population size of $N_p = 100$ is chosen.

In a first case study, the constraint in (5.21) is disregarded and $k^*_{\text{eff}} = 0.75$ W/mK and $\alpha^*_{\text{eff}} = 25$ ppm/K are specified as target values. Figure 5.22 shows the Pareto frontiers in dependence of the specified number of function evaluations (NFE). It can be observed that the approximation of the Pareto front seems to stabilize after about 10000 NFE. A change in the population size, the mutation, and the crossover operators does not show a significant effect on the resulting front. Observing the large number of function evaluations, the advantage of the surrogate-based approach with view of computational efficiency becomes directly clear.

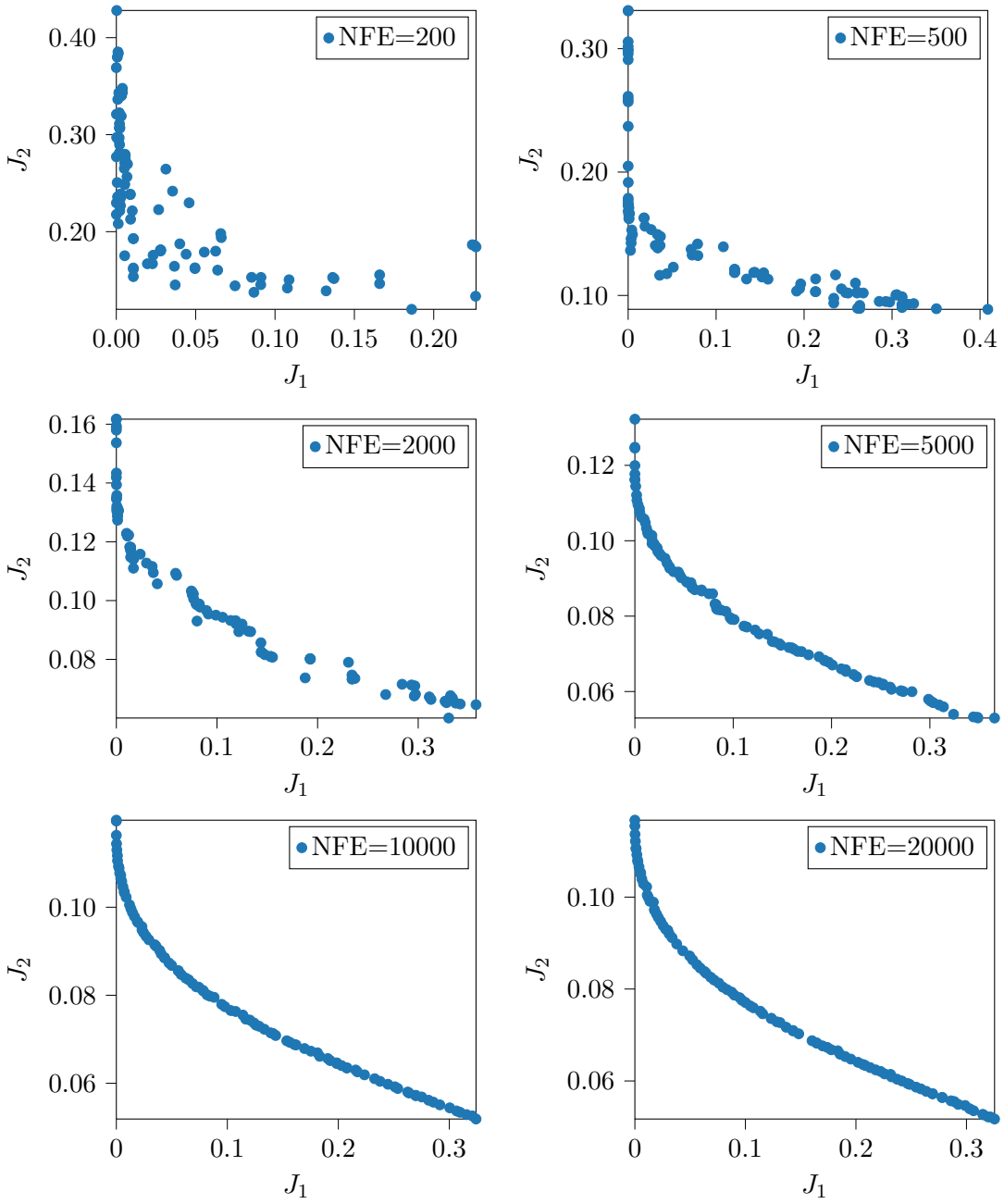

Figure 5.22: Pareto front in dependence of the number of function evalutions (NFE)

The Pareto front obtained with NFE=20000 is illustrated again in Fig. 5.23. It can be observed that the desired ETC can be attained (see also the results in Section 5.1).

The corresponding Pareto optimal point (PO1) shows a CTE of 33.54 ppm/K. If one interprets the optimization results starting from this point, one can observe that α_{eff} can be improved only slightly at the expense of a relatively strong deterioration of the ETC. Since the solution of the optimization problem is provided by a set of different solutions, a decision has to be made which design should be the final one. The Pareto optimal solution featuring the "optimal" ETC (PO1) is selected as final design. In addition, two further points of the front, (PO2) and (PO3), are considered. The corresponding design variables of all three Pareto optimal solutions are listed in Table 5.19. It can be observed that the filler volume fraction reaches the upper limit for all three points. Observing other points of the front, one can notices that it is mainly the phase fraction that differs. Please note that the remaining variables have almost no impact on the solution of this unconstrained optimization problem. For example, when evaluating the micromechanical model by setting E_{fl} to the upper bound, the CTE can only be improved by 0.8 %, so the error of the surrogate model is still quite small. One possibility would therefore be to neglect the non-sensitive parameters as in Section 5.1 and perform an optimization in the reduced design space. But even for such high-dimensional parameter spaces, a solution can be found in an efficient way with the surrogate representation. In summary, it can be stated that α_{eff} can only be slightly improved by increasing the phase fraction δ_{fp}, which is accompanied by a disproportionate deterioration of k_{eff}.

Since the optimization results were determined on the surrogate representation of the optimization problem (5.21), a validation is conducted by evaluating the micromechanical model. Table 5.20 shows a comparison of the optimas from the surrogate representation (Surr.) with the evaluation of the micromechanical model (Sim.). Although E_{eff} is not included in this first case study, the corresponding values are given here as additional information. A relatively large deviation in the ETC of 5.63 % can be observed. This may be due to the fact that the maximum filler volume fraction is analyzed, which cannot be captured accurately enough by the surrogate. For this purpose, a common and simple strategy is employed by adding the three Pareto-optimal points (PO1, PO2 and PO3) to the training data set for the ETC model and repeating the MOO optimization. The Pareto front obtained with that refined surrogate model is shown in Fig. 5.24. The corresponding design variables are listed in Table 5.21. A renewed validation (see Table 5.22) shows a quite low deviation with a maximum error of 1.70 % for the ETC.

Design variable	PO1	PO2	PO3
d_1 / %	34.00	34.00	34.00
d_2 / %	29.99	50.79	75.00
d_3 / GPa	367.93	373.93	363.76
d_4	0.29	0.30	0.30
d_5 / (ppm/K)	4.00	4.00	4.00
d_6 / (W/mK)	2.06	2.00	2.00
d_7 / GPa	184.49	185.84	203.42
d_8	0.30	0.30	0.30
d_9 / (ppm/K)	0.10	0.10	0.10
d_{10} / (W/mK)	204.05	164.75	157.55

Table 5.19: Pareto optimal solutions for the initial surrogate model

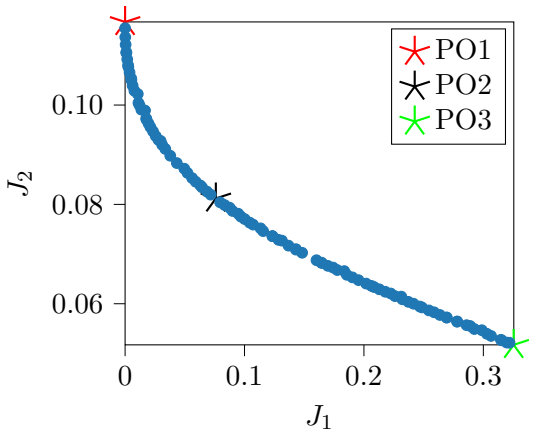

Figure 5.23: Pareto front for the initial surrogate model

Table 5.20: Validation of the selected Pareto optimal solutions - initial surrogate

Physical quantity	P01 Surr.	P01 Sim.	P01 Dev. / %	P02 Surr.	P02 Sim.	P02 Dev. / %	P03 Surr.	P03 Sim.	P03 Dev. / %
k_{eff} / (W/mK)	0.75	0.71	5.63	0.957	0.926	3.35	1.178	1.206	2.32
α_{eff} / (ppm/K)	33.54	33.72	0.53	32.13	32.21	0.25	30.69	30.43	0.85
E_{eff} / GPa	6.46	6.45	0.16	6.99	6.96	0.43	7.51	7.66	1.96

5.3.3 Case study 2

Observing the results of the first case study, it appears that the Pareto optimal designs exhibit a quite large stiffness (about E_{eff}=7 GPa compared to 2.3 GPa of the neat PBT material). As already explained with the example of the encapsulated circuit board, there is often a demand for a material with a reduced stiffness in order to reduce stresses, e.g., under temperature load. For that purpose, in the second case study, the optimization problem includes the specification of a maximum Young's modulus of $E_{\text{eff,max}}$= 5 GPa as constraint. The target values of k^*_{eff} = 0.75 W/mK and α^*_{eff} = 25 ppm/K are maintained. In Fig. 5.25, the resulting Pareto front is shown. The corresponding design variables are listed in Table 5.23. The main difference compared to the first case study is the reduced stiffness of the filler particles, especially the platelet-shaped particles E_{fl} due to the stiffness constraint. Because of this, α_{eff} deviates further

Design variable	PO1	PO2	PO3
d_1 / %	34.00	34.00	34.00
d_2 / %	35.73	53.42	75.00
d_3 / GPa	375.78	371.03	370.90
d_4	0.30	0.30	0.30
d_5 / (ppm/K)	4.00	4.00	4.00
d_6 / (W/mK)	2.00	2.00	2.00
d_7 / GPa	192.99	188.82	196.73
d_8	0.30	0.30	0.30
d_9 / (ppm/K)	0.10	0.10	0.10
d_{10} / (W/mK)	165.79	150.09	150.01

Table 5.21: Pareto optimal solutions for the refined surrogate model

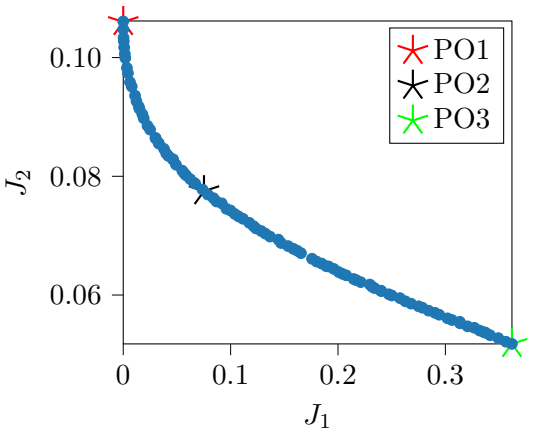

Figure 5.24: Pareto front for the refined surrogate model

Table 5.22: Validation of the selected Pareto optimal solutions - refined surrogate

Physical quantity	P01 Surr.	P01 Sim.	P01 Dev. / %	P02 Surr.	P02 Sim.	P02 Dev. / %	P03 Surr.	P03 Sim.	P03 Dev. / %
k_{eff} / (W/mK)	0.750	0.754	0.53	0.956	0.94	1.70	1.20	1.23	2.44
α_{eff} / (ppm/K)	33.15	33.29	0.42	31.96	32.04	0.25	30.69	30.48	0.69
E_{eff} / GPa	6.62	6.60	0.30	7.05	7.02	0.43	7.49	7.62	1.70

from the target value (respectively J_2). In Table 5.24, the effective values obtained from the surrogate representation are compared with an evaluation of the simulation model. Only slight deviations with a maximum error of 1.25 % for α_{eff} can be observed. The constraint is only slightly violated. If necessary, the refinemend strategy could be employed again to further improve the accuracy of the surrogate model in the vicinity of the Pareto optimal points. However, this is not done here, as the deviations are quite small.

Design variable	Value
d_1 / %	34.00
d_2 / %	35.89
d_3 / GPa	55.84
d_4	0.30
d_5 / (ppm/K)	4.00
d_6 / (W/mK)	2.02
d_7 / GPa	20.87
d_8	0.29
d_9 / (ppm/K)	0.17
d_{10} / (W/mK)	153.18

Table 5.23: Case study 2 - Pareto optimal solutions

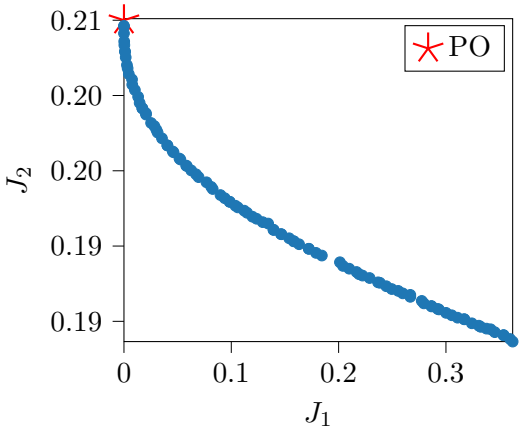

Figure 5.25: Case study 2 - Pareto front

Table 5.24: Case study 2 - Validation of the selected Pareto optimal solutions

Physical quantity	Surrogate	Simulation	Deviation %
k_{eff} / (W/mK)	0.750	0.758	1.05
α_{eff} / (ppm/K)	36.32	35.87	1.25
E_{eff} / GPa	5.00	5.05	0.99

Chapter 6

Conclusion and outlook

6.1 Summary and main results

In this work, an optimization methodology for the design of functional materials was proposed. The need for such a design framework arises from the challenging multiphysical requirements imposed on materials in the context of electromobility applications. Focus was placed on the thermomechanical properties of polymer matrix composites. The main results of this work consist in tackling two key issues in material design: On the one hand, the computation of the overall thermomechanical properties of particle reinforced and short fiber reinforced polymers. This includes the geometrical and physical modeling of the heterogeneous microstructure with the concept of representative volume elements, the numerical solution of boundary value problems at the microscale, and the extraction of effective quantities by averaging (homogenization) relations. On the other hand, the formulation and efficient solution of parametric material optimization problems under consideration of physical descriptors of the microstructure as design variables. As solution method, a surrogate-based optimization approach is proposed, which essentially integrates design of experiments (sampling), the results from computational homogenization, surrogate modeling, and global optimization.

Concerning the constitutive modeling of thermomechanical materials, Chapter 2 covers some basic aspects of continuum mechanics and the description of heat conduction problems. These notations and relations also apply at the microscale and are used in the following sections to determine the overall thermoelastic properties of the polymer matrix composites. The analogies between steady-state heat conduction and elastostatic boundary value problems are presented.

In Chapter 3, the surrogate-based multiscale approach for the design of composite materials is presented. To facilitate the use of optimization algorithms, a structural optimization problem is formulated for the material design. The established formulation allows the consideration of manifold demands for the effective physical material properties, taking into account the full anisotropic material behavior in terms of tensor quantities. Physical parameter of the microstructure are selected as design variables as this enables

a direct tailoring of the microstructure during the manufacturing process. These parameters are composed of design variables of the geometrical microstructure and the material properties of the individual constituents and specify the material design space. For the selection of a solution method, the properties of the generic optimization problem (3.1) were considered. Several aspects such as non-convexity and the influence of stochastic effects motivate the development of the surrogate-based optimization method. The basic idea consists in the approximation of the structure-property relationship through surrogate modeling techniques. Such surrogate models enables an efficient use of global optimization methods compared to the direct application on the micromechanical (simulation) model. Another important advantage is that these models allow an understanding of the complex SPR. For the creation of such surrogate model, the first step is to conduct virtual experiments on the basis of a DoE scheme. For each experimental sample, a RVE is generated and the corresponding effective properties are computed by numerical homogenization under prescribed periodic BCs. This results in a material database that describes the SPR for a discrete set of microstructural configurations. In a next step, this database is used to approximate the quantity of interest within the entire material design space. Kriging and response surface models are investigated as surrogate models. It should be noted that there exist also other models such as neural networks, splines, support vector machines, etc. that could also be used for this purpose. The use of (global) sensitivity analysis methods allows the quantification of the relative importance of the different design variables. A simple concept for the evaluation of the robustness of the designs is presented. The surrogate representation of the material optimization problem allows the use of global optimization algorithms which often require a large number of function evaluations in an tracktable way. Another advantage of the surrogate representation is that it allows the consideration of different targets on the material properties without the need of renewed simulations (except a validation simulation). Furthermore, existing models can be easily extended to include additional material properties in a multiphyics setting.

Chapter 4 provides a brief overview of particle reinforced and short fiber reinforced polymers. Technical relevant matrix and filler materials are mentioned. Selected aspects such as areas of application, manufacturing and important microscopic influencing factors are covered.

In Chapter 5, the surrogate-based multiscale optimization method is demonstrated by means of concrete material examples. In the first example (Section 5.1), a three-phase PRP with large contrast in the conductivities of the individual phases is investigated for which a certain effective thermal conductivity should be adjusted. Beside the filler volume fraction and the phase proportions, different geometrical parameters of the filler particles are specified as design variables. An analysis of the size and resolution of the structure is performed to ensure a sufficiently accurate calculation of the ETC. It

turns out that with a relatively small number of samples, an accurate model of the ETC can be created. The filler volume fraction and the phase proportions prove to be the most sensitive parameters, but also the aspect ratio of the platelet-shaped particles should not be neglected. For optimization, the DE algorithm is applied to the surrogate representation in order to identify different optimal microstructures. The validation of the optimization results with an evaluation of the micromechanical model (validation) shows only minor deviations. Subsequently, alternative optimization techniques such as a gradient-based method and a Bayesian optimization approach (EGO) are applied. Their advantages and disadvantages are discussed and compared with the proposed approach. For the considered example, the scaling of the design variable space and the adjustment of the step size to approximate the gradients by finite differences enables the direct application of gradient methods on the simulation model. The application of the EGO algorithm shows an identification of near optimal microstructures within only a few iterations. Corresponding measurements were conducted to validate the homogenization method. A comparison with the results of the micromechanic simulations shows a good agreement.
In Section 5.2, the methodology is applied for the optimization of the overall viscoelastic behavior of SFRPs. In addition to the fiber volume fraction and the fiber orientation distribution, the linear elastic material properties of the fibers are specified as design variables. Within the concept of the second-order Advani-Tucker fiber orientation tensor, the fiber orientation distribution can be depicted by only two parameters lying inside the so-called fiber orientation triangle. A generalized Maxwell model is employed to model viscoelastic effects of the polymer matrix. The corresponding material parameters are determined on the basis of experimental measurements. In a first step, virtual creep simulations are performed for each experimental sample. The corresponding BVPs are solved by FFT-based numerical homogenization for a prescribed macroscopic stress. This results in a viscoelastic material database describing the macroscopic creep compliance tensor for a discrete set of microstructural configurations. Based on this, Kriging models of the individual orthotropic components are constructed which describe the viscoelastic material behavior for arbitrary microstructures. A constraint version of DE is employed for the solution of the material optimization problem. Different design variants are identified for a target macroscopic creep compliance tensor and the robustness of these designs is investigated. A validation of the simulation method shows good agreement with experimentals as well.
An extension of the proposed method to address multiphysical problems is presented in Section 5.3. The problem formulation from Section 5.1 is extended and includes in addition to a target ETC a certain CTE while maintaining a maximum stiffness (if terms of the Young's modulus). To consider such requirements on the thermomechanical material properties, a formulation as MOO problem is introduced. A relatively large number of 10 design variables is specified, which covers the full thermomechanical behavior of the filler particles. Kriging models for each individual physical properties are created. A

validation of these models by appropriate error measures shows quite good prediction accuracy with a maximum error of 2.38% for the model of the ETC. This surrogate representations allows to find an approximation of the conflicting design objectives in terms of the Pareto frontier by population-based MOO methods in an efficient way. This is demonstrated by two examples. It can be observed that the Pareto optimal microstructures differ mainly in their phase fractions. This enables to select variants whether care have to taken to the ETC or the CTE.

Compared to the state of the art in material design, in this work the combination of different methods (DoE, numerical homogenization, metamodeling, sensitivity analysis, robustness evaluation, and global optimization) were applied to find particle reinforced and short fiber reinforced polymers with desired thermomechanical properties. The proposed approach was also employed for materials with more than a single phase. At this point, the importance of the microstructure simulation for the accuracy of the optimal solution should be reiterated. If the morphology of the microstructure and the physical material properties of the individual constituents are not accurate, an optimal solution cannot be found. The metamodel-based approach proved to be quite efficient to limit the high numerical effort of global optimization methods. A validation of the optimization results from the metamodel with the numerical model showed a quite good agreement in the considered examples.

6.2 Outlook and future work

By considering composites with high packing density and large contrasts in the conductivities of the constituents, a strong dependence of the ETC on the resolution of the structure (voxel length) was observed if the particles were allowed to touch each other. For this reason, isolated particles were considered in this work, which generally does not result in an ETC greater than 2 W/mK required for power electronics applications. In [72], the ETC of the considered three-phase material was experimentally determined and conductivities of the relevant magnitude were obtained. For applications in power electronics, so-called thermal interface materials (TIMs) are widely used. These materials are available in different forms, such as pastes or adhesives and exhibit very large filler contents up to 70 %. They are often applied as gap filler to improve the dissipation of heat between two or more surfaces. A realistic modeling of the particle contacts and the percolation network of such highly filled materials is a rather delicate task. An increasing refinement of the resolution of the structure (i.e., the voxel length in the applied software) is associated with a strong increase in the degrees of freedom. Even the generation of such structures may be connected with an enormous and partly unrealizable computational effort. In this context, it should be examined whether empirical models such as the Lewis-Nielsen model or percolation path models represent a simple

and sufficiently accurate alternative compared to numerical simulation methods.

The presented surrogate-based multiscale optimization method proves to be quite general and can be used for the modeling and optimization of various structural responses of composites. Hence, the approach can be applied for the optimization of other physical material properties as well as other types of composites than those considered in this work. In the context of electromobility applications, special interest is given to the electromagnetic properties of composite materials. In [136], a numerical method for the computation of the electromagnetic properties of dielectric and magnetic particulate composites is described. This method could be used in combination with the proposed optimization framework to optimize the electromagnetic properties of polymer matrix composites. Regarding mechanical properties, further material laws can be considered, e.g., to model effects such as damage due to plastic effects or cyclic loading. This is particularly important for technical applications of SFRPs and allows an accurate modeling of the complex material behavior within the polymer matrix at the microscopic level. The modelling of damage under static loading can be found in [173]. In [62], a material model for the polymer matrix to describe the cyclic stiffness degradation of GFRP is proposed. For such nonlinear material behavior, the dependence of the effective material response on the load case must be taken into account. This load dependency of the effective properties could be modelled similarly to the approach mentioned in [18] by increasing the degrees of freedom of the material design space. The application of the proposed optimization framework allows the optimization of the resulting material properties, e.g., with regard to failure.

Once the optimization results are available in the form of a digital microstructure, practical applications raise the question of realizing them during manufacturing. The parameters were chosen in such a way that they can be realized by designing the morphology of the microstructure and suitable filler materials. During the creation of the structures, a certain shape of the particles as well as orientation and distribution within the matrix were specified. In order to implement the optimization results, suitable manufacturing processes in combination with appropriate fillers must be developed. In [31], an overview of methods to tailor the microstructure and to realize anisotropic thermally conductive composites is given. Within this context, an interesting possibility is the optimization of components made of functional materials, e.g., in the setting of free material optimization [91]. Especially the use of different functional materials offers the potential to better realize the complex multiphysical requirements of componentes by locally designign the macroscopic properties. Another interesting task could be additive manufacturing processes with which more complex structures can be realized. An overview of the use of such methods for polymer composites can be found in [42] and [134].

Bibliography

[1] Aboudi, J., Arnold, S. M., and Bednarcyk, B. A. *Micromechanics of composite materials: A generalized multiscale analysis approach*. Elsevier Science, 2013.

[2] Abueidda, D. W., Almasri, M., Ammourah, R., Ravaioli, U., Jasiuk, I. M., and Sobh, N. A. „Prediction and optimization of mechanical properties of composites using convolutional neural networks“. *Composite Structures* 227 (2019), p. 111264.

[3] Adams, B. L., Henrie, A., Henrie, B., Lyon, M., Kalidindi, S. R., and Garmestani, H. „Microstructure-sensitive design of a compliant beam“. *Journal of the Mechanics and Physics of Solids* 49.8 (2001), pp. 1639–1663.

[4] Advani, S. G. and Tucker, C. L. „The Use of Tensors to Describe and Predict Fiber Orientation in Short Fiber Composites“. *Journal of Rheology* 31.8 (1987), pp. 751–784.

[5] Agrawal, A. and Choudhary, A. „Perspective: Materials informatics and big data: Realization of the “fourth paradigm” of science in materials science“. *APL Materials* 4 (2016), p. 053208.

[6] Ahmad, M. F., Mat Isa, N. A., Lim, W. H., and Ang, K. M. „Differential evolution: A recent review based on state-of-the-art works“. *Alexandria Engineering Journal* 61.5 (2022), pp. 3831–3872.

[7] Altenbach, H. and Eremeyev, V. „Basic Equations of Continuum Mechanics“. *Plasticity of Pressure-Sensitive Materials*. Ed. by Altenbach, H. and Öchsner, A. Springer, Berlin, Heidelberg, 2014, pp. 1–47.

[8] Arora, S. J. *Introduction to Optimum design*. Academic Press, 2017.

[9] Ashank, Chakravarty, S., Garg, P., Kumar, A., Agrawal, M., and Agnihotri, P. „Deep neural networks based predictive-generative framework for designing composite materials“. *Modelling and Simulation in Materials Science and Engineering* 30.7 (2022), p. 075003.

[10] *ASTM D5470-12, Standard Test Method for Thermal Transmission Properties of Thermally Conductive Electrical Insulation Material*. ASTM International. 2012.

[11] Bakhvalov, N. S. and Panasenko, G. *Homogenisation: Averaging Processes in Periodic Media: Mathematical Problems in the Mechanics of Composite Materials*. Springer Netherlands, 1989.

[12] Bandemer, H. and Bellmann, A. *Statistische Versuchsplanung*. Vieweg+Teubner Verlag, 1994.

[13] Bargmann, S., Klusemann, B., Markmann, J., Schnabel, J., Schneider, K., Soyarslan, C., and Wilmers, J. „Generation of 3D representative volume elements for heterogeneous materials: A review“. *Progress in Materials Science* 96 (2018), pp. 322–384.

[14] Becker, J., Biebl, F., Glatt, E., Cheng, L., Grießer, A., Groß, M., Linden, S., Mosbach, D., Wagner, C., Weber, A., and Westerteiger, R. *GeoDict simulation software Release 2023*.

[15] Becker, J., Cheng, L., and Planas, B. *ConductoDict User Guide 2022*. Tech. rep. Math2Market GmbH.

[16] Ben-Tal, A., Ghaoui, L. E., and Nemirovski, A. *Robust Optimization*. Princeton University Press, 2009.

[17] Benveniste, Y. „A new approach to the application of Mori-Tanaka's theory in composite materials“. *Mechanics of Materials* 6.2 (1987), pp. 147–157.

[18] Bessa, M. A., Bostanabad, R., Liu, Z., Hu, A., Apley, D. W., Brinson, L. C., Chen, W., and Liu, W. K. „A framework for data-driven analysis of materials under uncertainty: Countering the curse of dimensionality“. *Computer Methods in Applied Mechanics and Engineering* 320 (2017), pp. 633–667.

[19] Beyer, H.-G. and Schwefel, H.-P. „Evolution strategies - A comprehensive introduction“. *Natural Computing* 1.1 (2002), pp. 3–52.

[20] Beyer, H.-G. and Sendhoff, B. „Robust Optimization - A Comprehensive Survey“. *Computer Methods in Applied Mechanics and Engineering* 196.33-34 (2007), pp. 3190–3218.

[21] Bostanabad, R., Zhang, Y., Li, X., Kearney, T., Brinson, L. C., Apley, D. W., Liu, W. K., and Chen, W. „Computational microstructure characterization and reconstruction: Review of the state-of-the-art techniques“. *Progress in Materials Science* 95 (2018), pp. 1–41.

[22] Bouhlel, M. A., Hwang, J. T., Bartoli, N., Lafage, R., Morlier, J., and Martins, J. R. R. A. „A Python surrogate modeling framework with derivatives“. *Advances in Engineering Software* (2019), p. 102662.

[23] Box, G. E. P. and Draper, N. R. *Empirical Model-Building and Response Surfaces*. Wiley, 1987.

[24] Branke, J., Deb, K., Miettinen, K., and Roman, S. *Multiobjective Optimization: Interactive and Evolutionary Approaches*. Springer, Berlin, Heidelberg, 2008.

[25] Brinson, L. C., Deagen, M., Chen, W., McCusker, J., Mcguinness, D., Schadler, L. S., Palmeri, M., Ghumman, U. F., Lin, A., and Hu, B. „Polymer Nanocomposite Data: Curation, Frameworks, Access, and Potential for Discovery and Design“. *ACS Macro Letters* 9.8 (2020), pp. 1086–1094.

[26] Budiansky, B. „On the elastic moduli of some heterogeneous materials“. *Journal of The Mechanics and Physics of Solids* 13.4 (1965), pp. 223–227.

[27] *CAMPUS*. Altair Engineering GmbH. Chemie Wirtschaftsförderungs-GmbH.

[28] Cang, R., Xu, Y., Chen, S., Liu, Y., Jiao, Y., and Ren, Y. „Microstructure Representation and Reconstruction of Heterogeneous Materials Via Deep Belief Network for Computational Material Design“. *Journal of Mechanical Design* 139.7 (2017).

[29] Chand, S. „Review Carbon Fibers for Composites“. *Journal of Materials Science* 35.6 (2000), pp. 1303–1313.

[30] Chen, C.-T. and Gu, G. „Machine learning for composite materials“. *MRS Communications* 9 (2019), pp. 1–11.

[31] Chen, H., Ginzburg, V. V., Yang, J., Yang, Y., Liu, W., Huang, Y., Du, L., and Chen, B. „Thermal Conductivity of Polymer-Based Composites: Fundamentals and Applications“. *Progress in Polymer Science* 59 (2016), pp. 41–85.

[32] Chen, W., Iyer, A., and Bostanabad, R. „Data Centric Design: A New Approach to Design of Microstructural Material Systems“. *Engineering* 10 (2022), pp. 89–98.

[33] Christensen, P. W. and Klarbring, A. *An Introduction to Structural Optimization*. Springer Netherlands, 2008.

[34] Cox, S. E., Haftka, R. T., Baker, C. A., Grossman, B., Mason, W. H., and Watson, L. T. „A Comparison of Global Optimization Methods for the Design of a High-speed Civil Transport“. *Journal of Global Optimization* 21 (2001), pp. 415–432.

[35] Curtarolo, S., Hart, G. L. W., Nardelli, M. B., Mingo, N., Sanvito, S., and Levy, O. „The high-throughput highway to computational materials design“. *Nature Materials* 12.3 (2013), pp. 191–201.

[36] Das, I. and Dennis, J. E. „A Closer Look at Drawbacks of Minimizing Weighted Sums of Objectives for Pareto Set Generation in Multicriteria Optimization Problems“. *Structural Optimization* 14 (1997), pp. 63–69.

[37] Das, S. and Suganthan, P. N. „Differential Evolution: A Survey of the State-of-the-Art.“ *IEEE Transactions on Evolutionary Computation* 15.1 (2011), pp. 4–31.

[38] Deb, K., Agrawal, S., Pratap, A., and Meyarivan, T. „A fast and elitist multiobjective genetic algorithm: NSGA-II“. *IEEE Transactions on Evolutionary Computation* 6.2 (2002), pp. 182–197.

[39] Dem'yanov, V. F. and Malozemov, V. N. „On the theory of non-linear minimax problems“. *Russian Mathematical Surveys* 26.3 (1971), pp. 57–115.

[40] Diebels, S. and Rjasanow, S. *Multi-scale Simulation of Composite Materials: Results from the Project MuSiKo*. Springer, Berlin, Heidelberg, 2019.

[41] Ehrgott, M. *Multicriteria Optimization*. Springer, Berlin, Heidelberg, 2005.

[42] El Moumen, A., Tarfaoui, M., and Lafdi, K. „Additive manufacturing of polymer composites: Processing and modeling approaches“. *Composites Part B: Engineering* 171 (2019), pp. 166–182.

[43] Eshelby, J. D. „The determination of the elastic field of an ellipsoidal inclusion, and related problems“. *Proceedings of the Royal Society of London. Series A, Mathematical and Physical Sciences* 241.1226 (1957), pp. 376–396.

[44] Ferreira, F. V., Pinheiro, I. F., Souza, S. F. de, Mei, L. H. I., and Lona, L. M. F. „Polymer Composites Reinforced with Natural Fibers and Nanocellulose in the Automotive Industry: A Short Review“. *Journal of Composites Science* 3.2 (2019).

[45] Feyel, F. and Chaboche, J.-L. „FE2 multiscale approach for modelling the elastoviscoplastic behaviour of long fibre SiC/Ti composite materials“. *Computer Methods in Applied Mechanics and Engineering* 183.3 (2000), pp. 309–330.

[46] Fisher, R. A. *The Design of Experiments*. Oliver and Boyd, 1935.

[47] Flemming, M., Ziegmann, G., and Roth, S. *Faserverbundbauweisen: Fasern und Matrices*. Springer, Berlin, Heidelberg, 1995.

[48] Forrester, A. I. J. and Keane, A. J. „Recent advances in surrogate-based optimization“. *Progress in Aerospace Sciences* 45.1-3 (2009), pp. 50–79.

[49] Fullwood, D. T., Niezgoda, S. R., Adams, B. L., and Kalidindi, S. R. „Microstructure Sensitive Design for Performance Optimization“. *Progress in Materials Science* 55.6 (2010), pp. 477–562.

[50] Gao, C., Shen, Y., and Wang, T. „Enhanced thermal conductivity for traditional epoxy packaging composites by constructing hybrid conductive network“. *Materials Research Express* 7.6 (2020).

[51] Geers, M. G. D., Kouznetsova, V. G., and Brekelmans, W. A. M. „Multi-scale computational homogenization: Trends and challenges“. *Journal of Computational and Applied Mathematics* 234.7 (2010), pp. 2175–2182.

[52] Goldberg, D. E. *Genetic Algorithms in Search, Optimization and Machine Learning*. Addison-Wesley, 1989.

[53] Grimm-Strele, H. and Kabel, M. „Runtime optimization of a memory efficient CG solver for FFT-based homogenization: implementation details and scaling results for linear elasticity“. *Computational Mechanics* 64.6 (2019), pp. 1339–1345.

[54] Gross, D. and Seelig, T. *Bruchmechanik: Mit einer Einführung in die Mikromechanik*. Springer, Berlin, Heidelberg, 2016.

[55] Gunantara, N. „A review of multi-objective optimization: Methods and its applications“. *Cogent Engineering* 5.1 (2018).

[56] Hadka, D. „Platypus-multiobjective optimization in python“. *Revision 0552483b* (2015).

[57] Haftka, R. T., Gürdal, Z., and Kamat, M. P. *Elements of Structural Optimization*. Springer Netherlands, 2014.

[58] Han, Z. and Fina, A. „Thermal Conductivity of Carbon Nanotubes and Their Polymer Nanocomposites: A Review“. *Progress in Polymer Science* 36 (2011), pp. 914–944.

[59] Hashemi, M. S., Safdari, M., and Sheidaei, A. „A supervised machine learning approach for accelerating the design of particulate composites: Application to thermal conductivity“. *Computational Materials Science* 197 (2021), p. 110664.

[60] Hashin, Z. and Shtrikman, S. „A variational approach to the theory of the elastic behaviour of polycrystals“. *Journal of The Mechanics and Physics of Solids* 10.4 (1962), pp. 343–352.

[61] Haupt, P. *Continuum Mechanics and Theory of Materials*. Springer, Berlin, Heidelberg, 2013.

[62] Henkelmann, N., Köbler, J., Andrä, H., Welschinger, F., Müller, R., and Schneider, M. „A multiscale high-cycle fatigue-damage model for the stiffness degradation of fiber-reinforced materials based on a mixed variational framework“. *Computer Methods in Applied Mechanics and Engineering* 388 (2022), p. 114198.

[63] Herman, J. and Usher, W. „SALib: An open-source Python library for Sensitivity Analysis“. *The Journal of Open Source Software* 2.9 (2017).

[64] Hilden, J., Rief, S., and Planas, B.
GrainGeo User Guide 2022. Tech. rep. Math2Market GmbH.

[65] Hilden, J., Rief, S., and Planas, B.
FiberGeo User Guide 2022. Tech. rep. Math2Market GmbH.

[66] Hill, R. „A self-consistent mechanics of composite materials“. *Journal of The Mechanics and Physics of Solids* 13.4 (1965), pp. 213–222.

[67] Hill, R. „Elastic properties of reinforced solids: some theoretical principles“. *Journal of The Mechanics and Physics of Solids* 11.5 (1963), pp. 357–372.

[68] Holland, J. H. *Adaptation in Natural and Artificial Systems: An Introductory Analysis with Applications to Biology, Control, and Artificial Intelligence*. MIT Press, 1992.

[69] Holzapfel, G. A. *Nonlinear Solid Mechanics: A Continuum Approach for Engineering*. Wiley, 2000.

[70] Homma, T. and Saltelli, A. „Importance measures in global sensitivity analysis of nonlinear models“. *Reliability Engineering & System Safety* 52.1 (1996), pp. 1–17.

[71] Hong, J.-P., Yoon, S.-W., Hwang, T., Oh, J.-S., Hong, S.-C., Lee, Y., and Nam, J.-D. „High thermal conductivity epoxy composites with bimodal distribution of aluminum nitride and boron nitride fillers“. *Thermochimica Acta* 537 (2012), pp. 70–75.

[72] Hoppmann, C. and Adamy, M. „Compoundierung wärmeleitender Kunststoffe“. *Kunststoffxtra* (11/2016), pp. 20–24.

[73] Huang, X., Iizuka, T., Jiang, P., Ohki, Y., and Tanaka, T. „Role of Interface on the Thermal Conductivity of Highly Filled Dielectric Epoxy/AlN Composites“. *The Journal of Physical Chemistry C* 116 (2012), pp. 13629–13639.

[74] Huang, X., Jiang, P., and Tanaka, T. „A review of dielectric polymer composites with high thermal conductivity“. *IEEE Electrical Insulation Magazine* 27.4 (2011), pp. 8–16.

[75] Hwang, C. L., Masud, A. S. M., Paidy, S. R., and Yoon, K. *Multiple Objective Decision Making - Methods and Applications: A State-of-the-Art Survey*. Springer, Berlin, Heidelberg, 2012.

[76] Hyun, S. and Torquato, S. „Designing composite microstructures with targeted properties“. *Journal of Materials Research* 16 (2001), pp. 280–285.

[77] Iooss, B. and Saltelli, A. „Introduction to Sensitivity Analysis“. *Handbook of Uncertainty Quantification*. Ed. by Ghanem, R, Higdon, D., and Owhadi, H. Springer, Cham, 2017, pp. 1103–1122.

[78] Iwanaga, T., Usher, W., and Herman, J. „Toward SALib 2.0: Advancing the accessibility and interpretability of global sensitivity analyses“. *Socio-Environmental Systems Modelling* 4 (2022), p. 18155.

[79] Iyer, A., Zhang, Y., Prasad, A., Tao, S., Wang, Y., Schadler, L. S., Brinson, L. C., and Chen, W. „Data-Centric Mixed-Variable Bayesian Optimization for Materials Design“. *Proceedings of the ASME 2019 International Design Engineering Technical Conferences and Computers and Information in Engineering Conference. Volume 2A: 45th Design Automation Conference*. Anaheim, California, USA. 2019.

[80] Jin, R., Chen, W., and Sudjianto, A. „An Efficient Algorithm for Constructing Optimal Design of Computer Experiments“. *Journal of Statistical Planning and Inference* 134.1 (2005), pp. 268–287.

[81] Jones, D. R., Schonlau, M., and Welch, W. J. „Efficient Global Optimization of Expensive Black-Box Functions“. *Journal of Global Optimization* 13.4 (1998), pp. 455–492.

[82] Kachanov, M. and Sevostianov, I. *Micromechanics of Materials, with Applications*. Springer International Publishing, 2018.

[83] Kaliske, M. and Rothert, H. „Formulation and implementation of three-dimensional viscoelasticity at small and finite strains“. *Computational Mechanics* 19 (1997), pp. 228–239.

[84] Kanit, T., Forest, S., Galliet, I., Mounoury, V., and Jeulin, D. „Determination of the Size of the Representative Volume Element for Random Composites: Statistical and Numerical Approach“. *International Journal of Solids and Structures* 40.13-14 (2003), pp. 3647–3679.

[85] Kennedy, J. and Eberhart, R. „Particle swarm optimization“. *Proceedings of ICNN'95 - International Conference on Neural Networks*. Vol. 4. 1995, pp. 1942–1948.

[86] Kirkpatrick, S., Gelatt, C. D., and Vecchi, M. P. „Optimization by Simulated Annealing“. *Science* 220 (1983), pp. 671–680.

[87] Kirsch, U. *Structural Optimization: Fundamentals and Applications*. Springer, Berlin, Heidelberg, 2012.

[88] Kleijnen, J. and Sargent, R. „A Methodology for Fitting and Validating Metamodels in Simulation“. *European Journal of Operational Research* 120 (2000), pp. 14–29.

[89] Köbler, J., Schneider, M., Ospald, F., Andrä, H., and Müller, R. „Fiber orientation interpolation for the multiscale analysis of short fiber reinforced composite parts“. *Computational Mechanics* 61.4-5 (2018), pp. 729–750.

[90] Koch, P., Wujek, B., Golovidov, O., and Simpson, T. „Facilitating probabilistic multidisciplinary design optimization using Kriging approximation models“. 9th AIAA/ISSMO Symposium on Multidisciplinary Analysis and Optimization 2002, Atlanta, Georgia, United States. 2002.

[91] Kocvara, M. and Stingl, M. „Free material optimization: recent progress“. *Optimization* 57.1 (2008), pp. 79–100.

[92] Koehler, J. and Owen, A. B. „Computer experiments“. *Handbook of Statistics*. Ed. by Ghosh, S., Rao, C. R., and Owhadi, H. Elsevier Science, 1996, pp. 261–308.

[93] Komal, U. K., Lila, M. K., Chaitanya, S., and Singh, I. „Fabrication of Short Fiber Reinforced Polymer Composites“. *Reinforced Polymer Composites: Processing, Characterization and Post Life Cycle Assessment*. Ed. by Bajpai, P. K. and Singh, I. Wiley-VCH, 2019, pp. 21–38.

[94] Kouznetsova, V. G., Geers, M. G. D., and Brekelmans, W. A. M. „Multi-scale second-order computational homogenization of multi-phase materials: a nested finite element solution strategy“. *Computer Methods in Applied Mechanics and Engineering* 193.48-51 (2004), pp. 5525–5550.

[95] Kraus, M. A., Schuster, M., Kuntsche, J., Siebert, G., and Schneider, J. „Parameter identification methods for visco- and hyperelastic material models“. *Glass Structures & Engineering* 2 (2017).

[96] Kraus, T. and Kühnel, M. „Composites-Marktbericht 2015“. *Carbon Composites e.V. & AVK - Industrievereinigung Verstärkte Kunststoffe e.V.* (2015).

[97] Kröner, E. „Berechnung der elastischen Konstanten des Vielkristalls aus den Konstanten des Einkristalls“. *Zeitschrift für Physik* 151 (1958), pp. 504–518.

[98] Kwon, S. Y., Kwon, I. M., Kim, Y.-G., Lee, S., and Seo, Y.-S. „A large increase in the thermal conductivity of carbon nanotube/polymer composites produced by percolation phenomena“. *Carbon* 55 (2013), pp. 285–290.

[99] Lai, J. and Bakker, A. „3-D schapery representation for non-linear viscoelasticity and finite element implementation“. *Computational Mechanics* 18.3 (1996), pp. 182–191.

[100] Lampinen, J. „A constraint handling approach for the differential evolution algorithm“. *Proceedings of the 2002 Congress on Evolutionary Computation* 2 (2002), pp. 1468–1473.

[101] Lee, K.-H. and Park, G.-J. „Robust optimization considering tolerances of design variables“. *Computers & Structures* 79.1 (2001), pp. 77–86.

[102] Lewis, A. S. „Robust Regularization“. *Optimization Online* (2002).

[103] Liu, Y., Zhao, T., Ju, W., and Shi, S. „Materials discovery and design using machine learning“. *Journal of Materiomics* 3.3 (2017), pp. 159–177.

[104] Mallick, P. K. *Fiber-Reinforced Composites: Materials, Manufacturing, and Design*. Taylor & Francis, 2007.

[105] Mármol, G., Ferreira, D. P., and Fangueiro, R. „Automotive and construction applications of fiber reinforced composites“. *Fiber Reinforced Composites: Constituents, Compatibility, Perspectives, and Applications*. Ed. by Joseph, K., Oksman, K., George, G., Wilson, R., and Appukuttan, S. Woodhead Publishing, 2021, pp. 785–819.

[106] Marr, J., Zartmann, L., Reinel-Bitzer, D., Andrä, H., and Müller, R. „Multiscale optimization of the viscoelastic behavior of short fiber reinforced composites“. *International Journal of Mechanics and Materials in Design* 19.3 (2023), pp. 1–19.

[107] Marr, J., Zartmann, L., Reinel-Bitzer, D., Andrä, H., and Müller, R. „Parametric optimization of the effective thermal conductivity for a three-phase particle-filled composite“. *Computational Materials Science* 205.5 (2022), p. 111214.

[108] Matheron, G. „Principles of geostatistics“. *Economic Geology* 58.8 (1963), pp. 1246–1266.

[109] McDowell, D. L. and Kalidindi, S. R. „The materials innovation ecosystem: A key enabler for the Materials Genome Initiative“. *MRS Bulletin* 4 (2016), pp. 326–337.

[110] McKay, M. D., Beckman, R. J., and Conover, W. J. „A Comparison of Three Methods for Selecting Values of Input Variables in the Analysis of Output from a Computer Code“. *Technometrics* 21.2 (1979), pp. 239–245.

[111] Meckesheimer, M., Booker, A. J., Barton, R. R., and Simpson, T. W. „Computationally Inexpensive Metamodel Assessment Strategies“. *AIAA Journal* 40.10 (2002), pp. 2053–2060.

[112] Mirkhalaf, S. M., Pires, F. M. A., and Simoes, R. „Determination of the size of the Representative Volume Element (RVE) for the simulation of heterogeneous polymers at finite strains“. *Finite Elements in Analysis and Design* 119 (2016), pp. 30–44.

[113] Mitchell, T. J. and Morris, M. D. „Bayesian design and analysis of computer experiments: two examples“. *Statistica Sinica* 2.2 (1992), pp. 359–379.

[114] Mockus, J. „On Bayesian Methods for Seeking the Extremum“. *Lecture Notes in Computer Science* (1974), pp. 400–404.

[115] Montgomery-Smith, S., He, W., Jack, D. A., and Smith, D. E. „Exact tensor closures for the three-dimensional Jeffery's equation“. *Journal of Fluid Mechanics* 680 (2011), pp. 321–335.

[116] Montgomery, D. C. *Design and Analysis of Experiments*. Wiley, 2012.

[117] Montgomery, D. C., Peck, E. A., and Vining, G. G. *Introduction to Linear Regression Analysis*. Wiley, 2015.

[118] Moore, A. L. and Shi, L. „Emerging challenges and materials for thermal management of electronics“. *Materials Today* 17.4 (2014), pp. 163–174.

[119] Mori, T. A. and Tanaka, K. . „Average stress in matrix and average elastic energy of materials with misfitting inclusions“. *Acta Metallurgica* 21.5 (1973), pp. 571–574.

[120] Morris, M. D. and Mitchell, T. J. „Exploratory designs for computational experiments“. *Journal of Statistical Planning and Inference* 43.3 (1995), pp. 381–402.

[121] Moulinec, H. and Suquet, P. „A numerical method for computing the overall response of nonlinear composites with complex microstructure“. *Computer Methods in Applied Mechanics and Engineering* 157.1-2 (1998), pp. 69–94.

[122] Moulinec, H. and Suquet, P. „A fast numerical method for computing the linear and nonlinear mechanical properties of composites“. *Comptes Rendus de l'Académie des sciences. Série II. Mécanique, physique, chimie, astronomie* 318.11 (1994), pp. 1417–1423.

[123] Moussaddy, H., Therriault, D., and Lévesque, M. „Assessment of existing and introduction of a new and robust efficient definition of the representative volume element“. *International Journal of Solids and Structures* 50.24 (2013), pp. 3817–3828.

[124] Myers, R. H., Montgomery, D. C., and Anderson-Cook, C. M. *Response Surface Methodology: Process and Product Optimization Using Designed Experiments*. Wiley, 2016.

[125] Myers, R. H., Montgomery, D. C., Vining, G. G., Borror, C. M., and Kowalski, S. M. „Response Surface Methodology: A Retrospective and Literature Survey“. *Journal of Quality Technology* 36.1 (2004), pp. 53–77.

[126] Nair, A. B. and Joseph, R. „Eco-friendly bio-composites using natural rubber (NR) matrices and natural fiber reinforcements“. *Chemistry, Manufacture and Applications of Natural Rubber*. Ed. by Kohjiya, S. and Ikeda, Y. Woodhead Publishing, 2014, pp. 249–283.

[127] Nelder, J. A. and Mead, R. „A Simplex Method for Function Minimization“. *The Computer Journal* 7.4 (1965), pp. 308–313.

[128] Neumaier, A. „Complete search in continuous global optimization and constraint satisfaction“. *Acta Numerica* 13.1 (2004), pp. 271–369.

[129] Nocedal, J. and Wright, S. J. *Numerical Optimization*. Springer Nature, 2006.

[130] Olson, G. B. „Computational Design of Hierarchically Structured Materials“. *Science* 277.1237 (1997), pp. 1237–1242.

[131] Olson, G. B. „Designing a New Material World“. *Science* 288.5468 (2000), pp. 993–998.

[132] Ostoja-Starzewski, M. „Material spatial randomness: from statistical to representative volume element“. *Probabilistic Engineering Mechanics* 21.2 (2006), pp. 112–132.

[133] Panchal, J. H., Kalidindi, S. R., and McDowell, D. L. „Key Computational Modeling Issues in Integrated Computational Materials Engineering“. *Computer-Aided Design* 45.1 (2013), pp. 4–25.

[134] Parandoush, P. and Lin, D. „A Review on Additive Manufacturing of Polymer-Fiber Composites“. *Composite Structures* 182 (2017), pp. 36–53.

[135] Park, G.-J., Hwang, K.-H., Lee, T. H., and Lee, K. W. „Robust Design: An Overview“. *AIAA Journal* 44.1 (2006), pp. 181–191.

[136] Patel, B. and Zohdi, T. I. „Numerical estimation of effective electromagnetic properties for design of particulate composites“. *Materials & Design* 94 (2016), pp. 546–553.

[137] Pecht, M., Agarwal, R., McCluskey, F. P., Dishongh, T. J., Javadpour, S., and Mahajan, R. *Electronic Packaging Materials and Their Properties*. CRC Press, 1998.

[138] Pedregosa, F., Varoquaux, G., Gramfort, A., Michel, V., Thirion, B., Grisel, O., Blondel, M., Prettenhofer, P., Weiss, R., Dubourg, V., Vanderplas, J., Passos, A., Cournapeau, D., Brucher, M., Perrot, M., and Duchesnay, E. „Scikit-learn: Machine Learning in Python“. *Journal of Machine Learning Research* 12 (2011), pp. 2825–2830.

[139] Powell, M. J. D. „An efficient method for finding the minimum of a function of several variables without calculating derivatives“. *The Computer Journal* 7.2 (1964), pp. 155–162.

[140] Prashanth, S., Subbaya, K. M., Nithin, K. S., and Sachhidananda, S. „Fiber Reinforced Composites - A Review“. *Journal of Material Science & Engineering* 6.3 (2017), pp. 1–6.

[141] Queipo, N. V., Haftka, R. T., Shyy, W., Goel, T., Vaidyanathan, R., and Tucker, P. K. „Surrogate-based analysis and optimization“. *Progress in Aerospace Sciences* 41.1 (2005), pp. 1–28.

[142] Rajak, D. K., Pagar, D. D., Menezes, P. L., and Linul, E. „Fiber-Reinforced Polymer Composites: Manufacturing, Properties, and Applications“. *Polymers* 11.10 (2019).

[143] Ramprasad, R., Batra, R., Pilania, G., Mannodi-Kanakkithodi, A., and Kim, C. „Machine Learning and Materials Informatics: Recent Applications and Prospects“. *npj Computational Materials* 3.54 (2017).

[144] Rao, C. R. *Linear Statistical Inference And Its Applications*. Wiley India Pvt. Limited, 2009.

[145] Renard, J. and Marmonier, M. F. „Etude de l'initiation del'endommagement dans la matrice d'un matériau composite parune méthode d'homogénisation". *Aerospace Science and Technology* 6 (1987), pp. 37–51.

[146] Reuss, A. „Berechnung der Fließgrenze von Mischkristallen auf Grund der Plastizitätsbedingung für Einkristalle". *ZAMM - Zeitschrift für Angewandte Mathematik und Mechanik* 9.1 (1929), pp. 49–58.

[147] Rhein, B. „Robuste Optimierung mit Quantilmaßen auf globalen Metamodellen". PhD thesis. Universität zu Köln, 2014.

[148] Rief, S., Widera, A., and Planas, B. *ElastoDict User Guide 2022*. Tech. rep. Math2Market GmbH.

[149] Rösler, J., Harders, H., and Bäker, M. *Mechanisches Verhalten der Werkstoffe*. Springer Fachmedien Wiesbaden, 2012.

[150] Roy, A. K., Farmer, B. L., Varshney, V., Sihn, S., Lee, J., and Ganguli, S. „Importance of Interfaces in Governing Thermal Transport in Composite Materials: Modeling and Experimental Perspectives". *ACS Applied materials & interfaces* 4.2 (2012), pp. 545–563.

[151] Saal, J. E., Kirklin, S., Aykol, M., Meredig, B., and Wolverton, C. „Materials Design and Discovery with High-Throughput Density Functional Theory: The Open Quantum Materials Database (OQMD)". *JOM: The journal of the Minerals, Metals & Materials Society* 65.11 (2013), pp. 1501–1509.

[152] Sacks, J., Schiller, S. B., and Welch, W. J. „Designs for Computer Experiments". *Technometrics* 31.1 (1989), pp. 41–47.

[153] Sacks, J., Welch, W. J., Mitchell, T. J., and Wynn, H. P. „Design and Analysis of Computer Experiments". *Statistical Science* 4.4 (1989), pp. 409–423.

[154] Saltelli, A., Ratto, M., Andres, T., Campolongo, F., Cariboni, J., Gatelli, D., Saisana, M., and Tarantola, S. *Global sensitivity analysis: The primer*. Wiley, 2008.

[155] Saltelli, A., Annoni, P., Azzini, I., Campolongo, F., Ratto, M., and Tarantola, S. „Variance based sensitivity analysis of model output. Design and estimator for the total sensitivity index". *Computer Physics Communications* 181.2 (2010), pp. 259–270.

[156] Saltelli, A., Tarantola, S., Campolongo, F., and Ratto, M. *Sensitivity Analysis in Practice: A Guide to Assessing Scientific Models*. Wiley, 2004.

[157] Samsudin, S. S., Majid, M. S. A., Ridzuan, M. J. M., and Osman, A. F. „Thermal polymer composites of hybrid fillers". *IOP Conference Series: Materials Science and Engineering* 670.1 (2019).

[158] Santner, T. J., Williams, B. J., and Notz, W. I. *The Design and Analysis of Computer Experiments*. Springer New York, 2019.

[159] Schneider, M. „The sequential addition and migration method to generate representative volume elements for the homogenization of short fiber reinforced plastics“. *Computational Mechanics* 59.2 (2017), pp. 247–263.

[160] Schonlau, M. „Computer Experiments and Global Optimization“. PhD thesis. University of Waterloo, 1997.

[161] Schonlau, M., Welch, W. J., and Jones, D. R. „Global versus local search in constrained optimization of computer models“. *Lecture Notes-Monograph Series* 34 (1998), pp. 11–25.

[162] Schürmann, H. *Konstruieren mit Faser-Kunststoff-Verbunden*. Springer, Berlin, Heidelberg, 2006.

[163] Shanghai Bestry Performance Materials Co., L. *Product brochures: Surface modified BN-ABN series and Spherical Alumina-BAK series*.

[164] Sharma, A., Mukhopadhyay, T., Rangappa, S. M., Siengchin, S., and Kushvaha, V. „Advances in Computational Intelligence of Polymer Composite Materials: Machine Learning Assisted Modeling, Analysis and Design“. *Archives of Computational Methods in Engineering* 29 (2022), pp. 3341–3385.

[165] Sigmund, O. and Torquato, S. „Design of materials with extreme thermal expansion using a three-phase topology optimization method“. *Journal of the Mechanics and Physics of Solids* 45.6 (1997), pp. 1037–1067.

[166] Simpson, T. W., Allen, J. K., and Mistree, F. „Spatial Correlation Metamodels for Global Approximation in Structural Design Optimization“. *Proceedings of the ASME 1998 Design Engineering Technical Conferences: 24th Design Automation Conference*. Atlanta, Georgia, USA. 1998.

[167] Simpson, T. W., Mauery, T. M., Korte, J. J., and Mistree, F. „Kriging Models for Global Approximation in Simulation-Based Multidisciplinary Design Optimization“. *AIAA Journal* 39.12 (2001), pp. 2233–2241.

[168] Simpson, T. W., Peplinski, J. D., Koch, P. N., and Allen, J. K. „Metamodels for Computer-based Engineering Design: Survey and recommendations“. *Engineering with Computers* 17 (2001), pp. 129–150.

[169] Snyman, J. A. and Wilke, D. N. *Practical Mathematical Optimization: Basic Optimization Theory and Gradient-Based Algorithms*. Springer International Publishing, 2018.

[170] Sobol, I. M. „Global sensitivity indices for nonlinear mathematical models and their Monte Carlo estimates“. *Mathematics and Computers in Simulation* 55.1-3 (2001), pp. 271–280.

[171] Sobol, I. M. „Sensitivity Estimates for Nonlinear Mathematical Models“. 1993.

[172] Spahn, J. „An Efficient Multiscale Method for Modeling Progressive Damage in Composite Materials“. PhD thesis. Technische Universität Kaiserslautern, 2015.

[173] Spahn, J., Andrä, H., Kabel, M., and Müller, R. „A multiscale approach for modeling progressive damage of composite materials using fast Fourier transforms“. *Computer Methods in Applied Mechanics and Engineering* 268 (2014), pp. 871–883.

[174] Spall, J. C. „Implementation of the simultaneous perturbation algorithm for stochastic optimization“. *IEEE Transactions on Aerospace and Electronic Systems* 34.3 (1998), pp. 817–823.

[175] Storn, R. and Price, K. „Differential Evolution - A Simple and Efficient Heuristic for Global Optimization over Continuous Spaces“. *Journal of Global Optimization* 11.4 (1997), pp. 341–359.

[176] Swolfs, Y., Gorbatikh, L., and Verpoest, I. „Fibre hybridisation in polymer composites: A review“. *Composites Part A: Applied Science and Manufacturing* 67 (2014), pp. 181–200.

[177] Temizer, I. and Zohdi, T. I. „A numerical method for homogenization in nonlinear elasticity“. *Computational Mechanics* 40.2 (2007), pp. 281–298.

[178] Torquato, S. „Optimal Design of Heterogeneous Materials“. *Annual Review of Materials Research* 40 (2010), pp. 101–129.

[179] Torquato, S. *Random Heterogeneous Materials: Microstructure and Macroscopic Properties*. Springer New York, 2005.

[180] Torquato, S., Hyun, S., and Donev, A. „Multifunctional Composites: Optimizing Microstructures for Simultaneous Transport of Heat and Electricity“. *Physical Review Letters* 89.26 (2003), p. 266601.

[181] Vachhani, V. L., Dabhi, V. K., and Prajapati, H. B. „Survey of multi objective evolutionary algorithms“. *International Conference on Circuits, Power and Computing Technologies*. 2015, pp. 1–9.

[182] Vanderplaats, G. N. „Structural optimization for statics, dynamics and beyond“. *Journal of the Brazilian Society of Mechanical Sciences and Engineering* 28.3 (2006), pp. 316–322.

[183] Vanderplaats, G. N. „Thirty years of modern structural optimization“. *Advances in Engineering Software* 16.2 (1993), pp. 81–88.

[184] Vasudevan, R., Pilania, G., and Balachandran, P. V. „Machine learning for materials design and discovery“. *Journal of Applied Physics* 129.7 (2021), p. 070401.

[185] Virtanen, P., Gommers, R., Oliphant, T. E., Haberland, M., Reddy, T., Cournapeau, D., Burovski, E., Peterson, P., Weckesser, W., Bright, J., van der Walt, S. J., Brett, M., Wilson, J., Millman, K. J., Mayorov, N., Nelson, A. R. J., Jones, E., Kern, R., Larson, E., Carey, C. J., Polat, İ., Feng, Y., Moore, E. W., VanderPlas, J., Laxalde, D., Perktold, J., Cimrman, R., Henriksen, I., Quintero, E. A., Harris, C. R., Archibald, A. M., Ribeiro, A. H., Pedregosa, F., van Mulbregt, P., and SciPy 1.0 Contributors. „SciPy 1.0: Fundamental Algorithms for Scientific Computing in Python“. *Nature Methods* 17.3 (2020), pp. 261–272.

[186] Voigt, W. „Ueber die Beziehung zwischen den beiden Elasticitätsconstanten isotroper Körper“. *Annalen der Physik* 274.12 (1889), pp. 573–587.

[187] Wang, G. and Shan, S. „Review of Metamodeling Techniques in Support of Engineering Design Optimization“. *Journal of Mechanical Design* 129.4 (2007), pp. 370–380.

[188] Wattanakul, K., Manuspiya, H., and Yanumet, N. „Effective Surface Treatments for Enhancing the Thermal Conductivity of BN-Filled Epoxy Composite“. *Journal of Applied Polymer Science* 119.6 (2011), pp. 3234–3243.

[189] Wiegmann, A. and Zemitis, A. „EJ-HEAT: A fast explicit jump harmonic averaging solver for the effective heat conductivity of composite materials“. *Berichte des Fraunhofer ITWM* 94 (2006).

[190] Wiener, O. *Die Theorie des Mischkörpers für das Feld der stationären Strömung. Erste Abhandlung. Die Mittelwertsätze für Kraft, Polarisation und Energie.* Teubner, 1912.

[191] Wu, H. P., Wu, X. J., Ge, M., Zhang, G. Q., Wang, Y. W., and Jiang, J. Z. „Effect analysis of filler sizes on percolation threshold of isotropical conductive adhesives“. *Composites Science and Technology* 67.6 (2007), pp. 1116–1120.

[192] Wypych, G. *Handbook of Fillers.* Elsevier Science, 2016.

[193] Xu, H., Li, Y., Brinson, L. C., and Chen, W. „A descriptor-based design methodology for developing heterogeneous microstructural materials system“. *Journal of Mechanical Design* 136.5 (2014), p. 051007.

[194] Xu, H., Liu, R., Choudhary, A., and Chen, W. „A Machine Learning-Based Design Representation Method for Designing Heterogeneous Microstructures“. *Journal of Mechanical Design* 137.5 (2015), p. 051403.

[195] Xu, Y. and Chung, D. D. L. „Increasing the Thermal Conductivity of Boron Nitride and Aluminum Nitride Particle Epoxy-Matrix Composites by Particle Surface Treatments“. *Composite Interfaces* 7.4 (2000), pp. 243–256.

[196] Yang, J.-L., Zhang, Z., Schlarb, A. K., and Friedrich, K. „On the characterization of tensile creep resistance of polyamide 66 nanocomposites. Part I. Experimental results and general discussions“. *Polymer* 47.8 (2006), pp. 2791–2801.

[197] Yang, J.-L., Zhang, Z., Schlarb, A. K., and Friedrich, K. „On the characterization of tensile creep resistance of polyamide 66 nanocomposites. Part II: Modeling and prediction of long-term performance“. *Polymer* 47.19 (2006), pp. 6745–6758.

[198] Yang, Z., Li, X., Brinson, L. C., Choudhary, A. N., Chen, W., and Agrawal, A. „Microstructural Materials Design Via Deep Adversarial Learning Methodology“. *Journal of Mechanical Design* 140.11 (2018), p. 111416.

[199] Younis, A. and Dong, Z. „Trends, features, and tests of common and recently introduced global optimization methods“. *Engineering Optimization* 42.8 (2010), pp. 691–718.

[200] Yv, Y. H., Lasdon, L. S., and Da, D. W. „On a bicriterion formation of the problems of integrated system identification and system optimization“. *IEEE Transactions on Systems, Man, and Cybernetics* (1971), pp. 296–297.

[201] Zhang, S., Cao, X. Y., Ma, Y., Ke, Y., Zhang, J., and Wang, F. S. „The effects of particle size and content on the thermal conductivity and mechanical properties of Al2O3/high density polyethylene (HDPE) composites“. *Express Polymer Letters* 5.7 (2011), pp. 581–590.

[202] Zhang, Y., Tao, S., Chen, W., and Apley, D. W. „A Latent Variable Approach to Gaussian Process Modeling with Qualitative and Quantitative Factors“. *Technometrics* 62.3 (2020), pp. 291–302.

[203] Zhou, W., Qi, S., Tu, C., Zhao, H., Wang, C., and Kou, J. „Effect of the Particle Size of Al2O3 on the Properties of Filled Heat-Conductive Silicone Rubber“. *Journal of Applied Polymer Science* 104.2 (2007), pp. 1312–1318.

List of Figures

List of Tables

List of Abbreviations

BC ..... Boundary condition

BVP ..... Boundary value problem

CCD ..... Central composite design

CG ..... Conjugate gradient

CTE ..... Coefficient of thermal expansion

CV ..... Cross validation

DE ..... Differential evolution

DoE ..... Design of experiments

EI ..... Expected improvement

EGO ..... Efficient global optimization

ETC ..... Effective thermal conductivity

FD ..... Finite Differences

FE ..... Finite element

FEM ..... Finite element method

FFT ..... Fast Fourier transform

FRP ..... Fiber reinforced polymer

GFRP ..... Glass fiber reinforced polymer

ICME ..... Integrated computational materials engineering

IMSE ..... Integrated mean squared error

LCB ..... Lower confidence bound

LH ..... Latin Hypercube

LHS ..... Latin Hypercube sampling

MCR ..... Microstructure characterization and reconstruction

ML ..... Machine learning

MOEA ..... Multi-objective evolutionary algorithm

MOO ..... Multi-objective optimization

MSD ..... Microstructure-sensitive design

NFE ..... Number of function evaluations

NSGA ..... Non-dominated sorting genetic algorithm

PA ..... Polyamide

PBT ..... Polybutylenterephthalate

PRP ..... Particle reinforced polymer

RVE ..... Representative volume element

RSM ..... Response surface model

SFRP ..... Short fiber reinforced polymer

SMT ..... Surrogate modeling toolbox

SPR ..... Structure-property relationship

SQP ..... Sequential quadratic programming

TIM ..... Thermal interface material

TO ..... Topology optimization

WLB/WUB .. Wiener lower/upper bound

List of Symbols

Scalars

ν ..... Poisson's ratio

E ..... Young's modulus

G ..... Shear modulus

Ω ..... Macroscopic domain

ω ..... Microscopic (RVE) domain

ρ ..... Density

m ..... Mass

λ ..... First Lamé constant

μ ..... Second Lamé constant

u ..... Specific internal energy

c_v ..... Specific isochoric heat capacity

r ..... Heat sources/sinks

T ..... Temperature

T_g ..... Glass transition temperature

W_{el} ..... Elastic energy

Q ..... Thermal energy

V_f ..... Filler volume fraction

t ..... Time

v, V ..... Volume in current/reference configuration

a, A ..... Surface area in current/reference configuration

d_h ..... Characteristic length of the heterogeneities

l ..... Characteristic length of the RVE

L ..... Characteristic length of a macroscopic sample

h ..... Voxel length

ϵ_{ens} ..... Ensemble size measure

ϵ_{vol} ..... Volume size measure

ϵ_{res} ..... Measure for the resolution of the RVE

y ..... Surrogate model output

ϵ ..... Random error

σ^2 ..... Global variance of the Kriging model

s^2 ..... Local variance of the Kriging model

θ ..... Correlation parameter

R^2 ..... Coefficient of determination

e ..... Error metric of the surrogate model

N_p ..... Population size

F ..... Mutant factor

$P_{\mathbf{cross}}$ ..... Crossover probability

V ..... Variance

E ..... Conditional expectation

S_i ..... First-order Sobol' index

S_{T_i} ..... Total-order Sobol' index

$\lambda_1, \lambda_2, \lambda_3$ ..... Eigenvalues of the fiber orientation tensor

η_k ..... Viscosity

τ_k ..... Relaxation constants

γ_k ..... Normalized relaxation coefficients

θ, γ, β ..... Euler angles

δ ..... Size parameter of the hypercube

ρ_R ..... Worst-case criterion

δ_{bn} ..... Proportion boron nitride

p_r ..... Particle size ratio

a_r ..... Aspect ratio

t_h ..... Thickness of the platelet-shaped particles

δ_{fp} ..... Proportion of the platelet-shaped particles

Vectors

$\boldsymbol{u}$ ..... Displacement vector

$\boldsymbol{d}$ ..... Design variables vector

$\boldsymbol{n}$ ..... Outward normal

$\boldsymbol{t}$ ..... Traction vector

$\boldsymbol{f}$ ..... Volume forces

$\boldsymbol{q}$ ..... Heat flux vector

∇T ..... Temperature gradient

$\boldsymbol{\beta}$ ..... Regression coefficient vector

$\boldsymbol{x}, \boldsymbol{X}$ ..... Position vector in current/reference configuration

$\boldsymbol{s}$ ..... Search direction

$\boldsymbol{v}$ ..... Mutant vector

$\boldsymbol{p}$ ..... Normalized fiber direction

$\boldsymbol{z}$ ..... Vector in design objective space

Tensors and matrices

$\boldsymbol{k}$ ..... Thermal conductivity tensor

$\boldsymbol{\alpha}$ ..... Thermal expansion tensor

$\boldsymbol{D}$ ..... Design matrix

$\boldsymbol{F}$ ..... Deformation gradient

$\boldsymbol{H}$ ..... Displacement gradient

$\boldsymbol{I}$ ..... Second-order identity tensor

$\boldsymbol{E}$ ..... Green-Lagrange strain tensor

$\boldsymbol{\epsilon}$ ..... Linearized strain tensor

$\boldsymbol{\sigma}$ ..... Cauchy stress tensor

$\boldsymbol{C}$ ..... Stiffness tensor

$\boldsymbol{S}$ ..... Compliance tensor

$\boldsymbol{\Psi_{\mathrm{eff}}}$ ..... Effective property of interest

$\boldsymbol{\Psi^{*}_{\mathrm{eff}}}$ ..... Target effective property of interest

$\|\boldsymbol{\Psi_{\mathrm{eff}}}\|_2$ ..... Frobenius norm of $\boldsymbol{\Psi}_{\mathrm{eff}}$

$\boldsymbol{R}$ ..... Correlation matrix

$\boldsymbol{R_{\mathrm{rot}}}$ ..... Rotation matrix

$\boldsymbol{a}$ ..... Microscopic quantity of interest

$\boldsymbol{\Gamma}$ ..... Creep relaxation tensor

$\boldsymbol{\Upsilon}$ ..... Creep compliance tensor

$\boldsymbol{A}$ ..... Advani-Tucker fiber orientation tensor

Lebenslauf

Name	Julian Marr
07/2009	Fachhochschulreife Ausbildungsrichtung Technik Fachoberschule Kulmbach
10/2009 - 01/2015	Diplom-Ingenieur (FH) Maschinenbau Hochschule Coburg
10/2016 - 09/2019	Master of Science Computational Engineering Anwendungsfach Maschinenbau Technische Universität Darmstadt
10/2019 - 12/2022	Doktorand ZF Friedrichshafen AG